Search for Pentaquark Partners Θ^{++}, Σ^0 and N^0 in H(e,e'K(π))X Reactions at Jefferson Lab Hall A

by

Yi Qiang

Submitted to the Department of Physics
in partial fulfillment of the requirements for the degree of

Doctor of Philosophy in Physics

at the

MASSACHUSETTS INSTITUTE OF TECHNOLOGY

May 2007

Author .....
Department of Physics
May 25, 2007

Certified by .....
William Bertozzi
Professor of Physics
Thesis Supervisor

Certified by .....
Shalev Gilad
Principle Research Scientist
Thesis Supervisor

Accepted by .....
Thomas J. Greytak
Professor of Physics, Associate Department Head for Education

Search for Pentaquark Partners Θ^{++}, Σ^0 and N^0 in H(e,e'K(π))X Reactions at Jefferson Lab Hall A

by

Yi Qiang

Submitted to the Department of Physics
on May 25, 2007, in partial fulfillment of the
requirements for the degree of
Doctor of Philosophy in Physics

Abstract

In 1997, D. Diakonov *et al.* using a soliton model predicted a $SU(3)_F$ flavor antidecuplet of pentaquarks. The most striking prediction using this symmetry group is a narrow exotic state, $\Theta^+(1540)$, which has quark component $uudd\bar{s}$. If such a state is confirmed, other members of the antidecuplet could be expected to have sufficiently narrow widths to be observed as well.

The Jefferson Laboratory experiment E04-012 focused on the search for Σ^0 and N^0 partner states in the missing mass spectra of the H(e,e'K^+)X and H(e,e'π^+)X channels. In addition, if the Θ^+ has non-zero isospin then a hypothetical isospin partner, Θ^{++}, might be expected in the H(e,e'K^-)X channel; this was also investigated.

The experiment was performed in Hall A at Jefferson Lab using a 5 GeV electron beam incident on a liquid hydrogen target. The two high resolution magnetic spectrometers were coupled to septum magnets to allow measurement of scattered electrons and outgoing hadrons at angles as small as 6 degrees. The missing mass resolution was determined to be 3.5 MeV/c^2 FWHM using neutron, $\Lambda(1116)$ and $\Sigma(1193)$ production and provided a high sensitivity to narrow resonances. A precise measurement of the $\Lambda(1520)$ resonance has also been conducted for a cross-section comparison.

As a result, no significant narrow resonances were observed in any of the three reaction channels being investigated. Based on this fact, a likelihood scan using the G. Feldman and R. Cousins method was performed. The analysis provided total cross section upper limits at 90% confidence level with no lower limits or always below background fluctuation.

Thesis Supervisor: William Bertozzi
Title: Professor of Physics

Thesis Supervisor: Shalev Gilad
Title: Principle Research Scientist

In memory of my Grandma

Hui-Wen Pu

1916-2006

Acknowledgments

I would like to deeply thank the various people, during all these years in which my graduate study lasted, providing me with so much help. Without their care and consideration I would likely not have achieved my doctoral degree.

First, I would like to thank my advisor Prof. William Bertozzi for his continuing guidance, attention, encourangement and support throughtout my graduate study at MIT. Many enlightening discussions with him not only enhanced my physics insight, but also helped me understand how to become a successful physicist.

I would like to thank my another advisor Dr. Shalev Gilad for his helpful discussions and friendly suggestions throughout my study and research as a graduate student.

I would like to thank my academic advisor Prof. Ulrich Becker for his careful guidance in my graduate courses. He also gave me very helpful advices on how to quickly master English as my second language.

I would like to thank my thesis committee members: Prof. John. W. Negele and Prof. Gabriella Sciolla for their valuable comments and corrections to this thesis.

I would like to thank my Jefferson Lab on-site supervisor Dr. Douglas Higinbotham. He quickly brought me involved in the Jefferson Lab colloboration and helped me get acquainted with the Hall A instrumentations and find interesting projects.

I would like to thank Dr. Bogdan Wojtsekhowski and Dr. Paul E. Reimer. for their role as the spokepersons in this experiment. Their delibrate experimental setup and run plan guaranteed a promising experiment. I learned a lof from their high standard experimental requirement and the unbiased scientific attitude. Bogdan also helped me so much during the preparation for my PhD candidate oral examination. His broad knowledge in not only experimental techinques but also nuclear physics theories was very impressive.

I would like to thank Dr. Jens-Ole Hansen, Dr. Robert Feuerbach, Dr. Olivier Gayou and Vahe Manyan for their help in my thesis data analysis.

I would like to thank Dr. John J. Lerose, Prof. Nilanga Liyange and Dr. Vicent Sulkosky for their invaluable help on the optimization of the Hall A spectrometer optics.

I would like to thank Prof. Franco Garibaldi and Francesco Cusanno from INFN for their contributions and discussions of the HRS optics and RICH detector.

I would like to thank the Hall A staff members: Dr. Kees de Jager, Dr. Jian-Ping Chen, Dr. Eugene Chudakov, Dr. Arun Saha, Dr. Bodo Reitz and the members of the Hall A collaboration for their commitment and shift efforts for this experiment. I would also like to thank the Jefferson Lab accelerator crew for delivering high quality beam for this experiment.

I would like to thank my friends, either graduate students or post-docs, whose friendship made my graduate study and research an enjoyable experience. They are: Peter Monaghan, Zhengwei Chai, Bin Zhang, Xiaochao Zheng, Lingyan Zhu, Yuan Xiao, Chi Zhang, Bin Ma, Andrew Puckett, Liang Lin, Lu Wan, Pan Mao, Lulin Yuan, Xiaofeng Zhu, Jianxun Yan, Bo Zhao, Ya Li, Huan Yao, Xin Qian, Zhihong Ye, Bryan Moffit, Ramesh Subedi, Ameya Kolarkar, Andrew Puckett.

I would like to thank my parents for all their love, their persistent support and everything they have done for me. They encouraged and pushed me to pursuit my physicist dream even though they already understood that it would require me, their only child, on another side of the earth.

Finally my thanks are to my girl friend Xiaohui Zhan for all her love and support to me through both easy and diffcult times during all these years together.

Contents

List of Figures

List of Tables

Chapter 1

Introduction

This thesis presents the results of the experiment E04-012 [8] searching for pentaquark states Σ_5^0, N_5^0 and Θ^{++} in electro-production. The experiment which was performed in Hall A at Jefferson Lab in 2004. The first chapter discusses the predictions and current experimental searches for the pentaquarks. The experimental setup is described in chapter 2. The detail of the cross section analysis is given in chapter 3. The last chapter presents and discusses the experimental results. A brief description of spectrometer's optics optimization can be found in the appendix.

1.1 Pentaquark Models

1.1.1 Exotic Baryons: Pentaquarks

Under the frame work of the constituent quark model and QCD most of hadrons are classified into two categories: meson and baryon. Mesons have baryon number $B = 0$ and are $q\bar{q}$ bound states of quarks q and anti-quarks $\bar{q}$. Baryons are fermions with baryon number $B = 1$ and so far all established baryons are 3-quark (qqq) configurations. However, QCD does not prohibit the existence of hadrons that lie outside of the naive quark model. While predictions of the decay rates and cross-sections based on isospin symmetry are close to experimental results in general, the quark model does not address quark confinement within the hadrons. This should not be surpris-

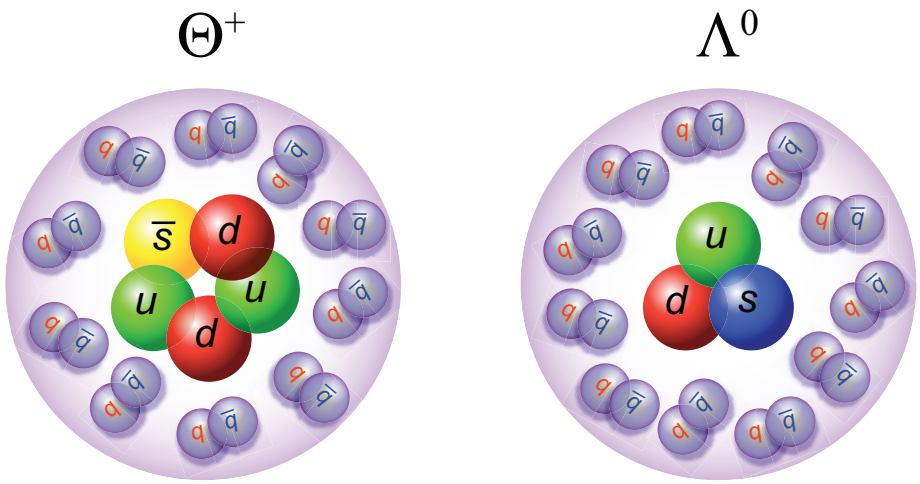

Figure 1-1: The quark configurations of an exotic pentaquark Θ^+ ($uudd\bar{s}$) and a normal baryon Λ^0 (uds). As can be seen, the minimum component of pentaquark Θ^+ is five quarks.

ing, since confinement should arise from the existence of gluons within the hadron states. the gluons themselves are in fact expected to contribute to the properties of the hadronic particles, and provide extra degrees of freedom. Various proposed models predict possible exotic mesons and baryons that involve more complex internal structures. Those states that have quantum numbers which cannot exist within the naive quark model are called exotic states. Possible exotic mesons may be classified as glueballs (gg), hybrids ($q\bar{q}g$), four-quarks states ($q\bar{q}q\bar{q}$), and exotic baryon ($qqqq\bar{q}$) states. It is also important to note that recent measurement of nucleon structure functions from high energy lepton-nucleon experiments has demonstrated that the quark cloud ($q\bar{q}$ pairs) does make contributions to the total momentum and spin of the nucleon. In other words, the usual baryons can be seen as a mixture of the standard (qqq) configuration, as well as ($qqqq\bar{q}$), ($qqqg$) configurations. Therefore, the search for exotic particles beyond the normal quark model is of fundamental importance to the understanding of quark confinement and the nature of the strong force. The exotic baryon ($qqqq\bar{q}$) states are generally called "pentaquark"s and Figure 1-1 shows such state Θ^+ along with a convetional baryon state Λ^0.

1.1.2 Early Predictions and Searches of Exotic Baryons

The exotic baryon state with positive strangeness and a minimal configuration of four quarks and an anti-quark was first discussed by R. L. Jaffe within MIT quark-bag model [9] in the 70's. These studies were continued by other authors (e.g.[10][11]) and the predictions of the lightest exotic pentaquark baryon ranged from 1.7 to 1.9 GeV/c^2. The searches for such states have been conducted for almost 40 years with both partial wave analysis of hadro-production (e.g.[12]) and electro-production (e.g.[13]). During those experiments, widths of the order of 100 MeV/c^2 were expected and the mass ranged from 1.55 to 2.65 GeV/c^2. These early results have generally been interpreted as unconvincing [14]. In fact, the whole section on pentaquarks was removed from the Particle Data Group after 1986.

1.1.3 Chiral Soliton Model

The chiral soliton model, proposed by Skyrme [15][16] in the 1960's, was a different approach to understand the nucleon. He suggested that the low-energy behavior of nucleons can be viewed as a spherically symmetric soliton solution of the pion field. The minimal generalization of spherical symmetry to incorporate three isospin components of the pion field is the so-called hedgehog form

$$\pi^a(\vec{x}) = \frac{x^a}{r} P(r), \tag{1.1}$$

where the superscript $a = 1, 2, 3$ is the spatial dimension index and $P(r)$ is the spherically-symmetric profile of the soliton. This implies that a spatial rotation of the field is equivalent to that in isospin and the rotational states have isospin T equal to spin J, with the excitation energies being

$$E_{rot} = \frac{J(J+1)}{2I}, \tag{1.2}$$

where I is the soliton moment of inertia. The rotational states are therefore $(2J+1)^2$-fold degenerate. The four nucleon states have $J = 1/2$ and the sixteen Δ-isobar states

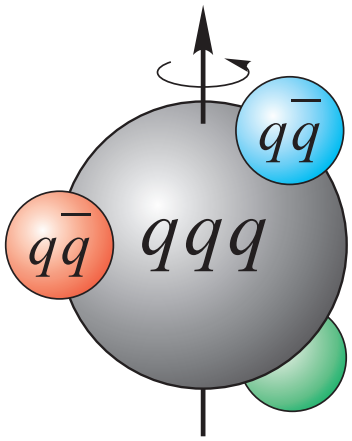

Figure 1-2: A simplistic picture of the chiral soliton model within which the baryon anti-decuplet is predicted. The baryons are represented by a qqq rigid core surrounded by $q\bar{q}$ meson field.

have $J = 3/2$. In this view, the baryonic nature of the nucleon is not due to quarks carrying baryon quantum number $B = 1/3$. Instead, the baryon number is interpreted as topological quantum number of the pion field [17][18]. QCD has shed some light into why this picture may be correct: the spontaneous chiral symmetry breaking in QCD determines to a great extent the strong interaction dynamics, while Witten attributes the reason the pion field inside the nucleon can be considered as a classic one, *i.e.* as a "soliton", to the large N_c (number of colors) argumentation [17].

By introducing the rotation in the flavor $SU(3)$ space, the quantizations show that the lowest baryon state is the octet with spin 1/2 and the next is the decuplet with spin 3/2 which are exactly what we meet in reality. Again, there are numerous relations between characteristics of members of the octet and the decuplet which follow purely from symmetry considerations. The most spectacular is the Guadagnini formula [19] which relates splittings inside the decuplet with those in the octet to an accuracy better than 1%. In the case of three-flavor, the third rotational excitation is an anti-decuplet $\overline{\mathbf{10}}$ with spin 1/2 which was mentioned as early as 1984 [20][21][22]. As it is demonstrated in Figure 1-2, pentaquark states come out naturally as the rotational excitations of the soliton rigid core (qqq) surrounded by meson fields ($q\bar{q}$) in the framework of the chiral soliton model.

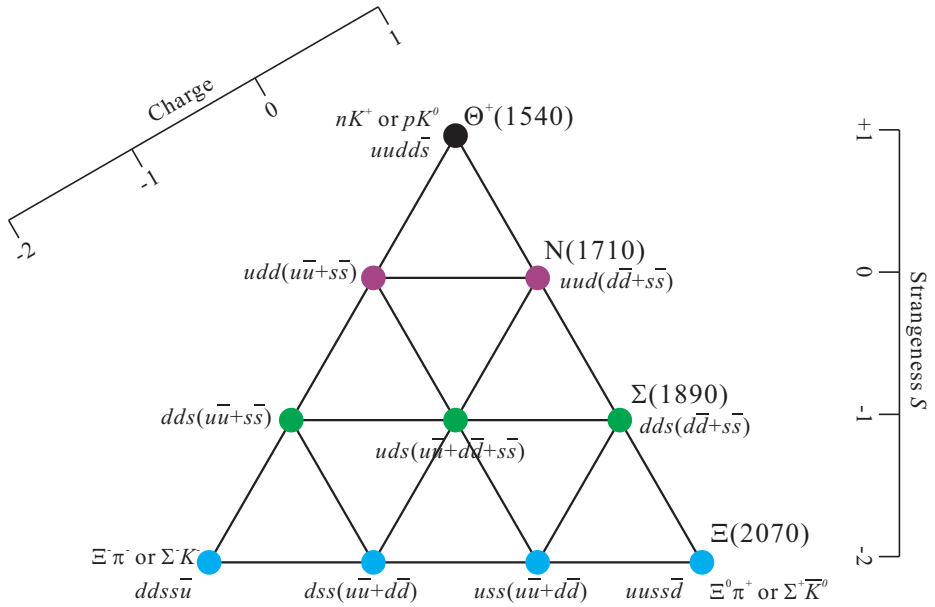

Figure 1-3: The baryon anti-decuplet predicted by Diakonov *et al.* [1] using the chiral soliton model with $N_c = 3$. The three corners are states that are manifestly exotic which are not accessible by conventional three quark baryons. The middle octet states overlap with the conventional baryons and are not exotic.

The numerical estimation $M_\Theta \approx 1530$ MeV/c^2 was obtained first by M. Praszalowicz [23] in 1987. The mass splittings within the octet and the decuplet of baryons were not described satisfactorily with parameters of the model at that time. In 1997, D. Diakonov, V. Petrov and M. Polyakov [1] made a definite prediction for the masses and widths of such anti-decuplet of pentaquarks states, see Figure 1-3. By identifying the rather well established nucleon resonance $N(1710, 1/2^+)$ as one of the members of the anti-decuplet, namely the one with the nucleon quantum members N_5[1], the second $SU(3)_f$ moment of inertia I_2 can be fixed and used to determine the mass and width of the anti-decuplet members. These calculations do not rely upon a specific dynamical realization, but follow from symmetry considerations.

In the anti-decuplet, three exotic baryon states locate at the corners: Θ^+ with $S = +1$, Ξ^{--} and Ξ^+ with $S = -2$. Such quantum numbers can only be obtained with a minimal pentaquark configuration of the type of $uudd\bar{s}$ for Θ^+, $ddss\bar{u}$ for Ξ^{--} and $uussd\bar{}$ for Ξ^+. Furthermore, the widths of these exotic pentaquarks were

[1]The subscript 5 stands for 5 quark component.

predicted by this model to be very narrow (10-20 MeV/c^2). These predictions suggest the possible observation of these exotic baryon states directly in an invariant mass spectrum, and would not need a more sophisticated but sometimes ambiguous partial wave analysis. The narrow width would also explain the lack of evidence of such exotic states from previous data, when widths of the order of 100 MeV/c^2 were expected. Of course, the choice of the anchoring member of the anti-decuplet ($N(1710, 1/2^+)$) is open to debate, therefore the experimental evidence for the existence of manifestly exotic pentaquark states is crucial for the validity of such models.

1.1.4 Di-Quark Model

Aside from the chiral soliton model of pentaquarks other models such as the di-quark model proposed by Jaffe and Wilczeck, have similar predictions in terms of the mass and width of the pentaquark baryon states [2]. Jaffe and Wilczeck argued that the chiral soliton model in the three-flavor case relies heavily on chiral $SU(3) \times SU(3)$ symmetry which is badly broken in nature. Instead, they propose a picture of the $q^4\bar{q}$ system in the frame work of a di-quark model, where the four quarks are bound into two spin zero, color and flavor $\bar{\mathbf{3}}$ di-quarks which form an $SU(3)_f$ $\bar{\mathbf{6}}$: $[ud]^2, [ud][us]_+, [us]^2, [us][ds]_+, [ds]^2 and [ds][ud]_+$. When combined with the anti-quark the result is a degenerate $SU(3)_f$ $\mathbf{8}_f \oplus \overline{\mathbf{10}}_f$, whose quark content is shown in Figure 1-4. The state $\Theta^+([ud]^2\bar{s})$ is identified as $\Theta^+(1540)$. The narrowness of the state is explained possibly by the relative weak coupling of the K^+n continuum to the $[ud]^2\bar{s}$ state from which it differs in color, spin and spatial wave functions.

The mass hierarchy of the di-quark model is compared with chiral soliton model in Figure 1-5. Though the prediction of the $\mathbf{8}_f \oplus \overline{\mathbf{10}}_f$ coincides with chiral soliton model in some extent, it differs in several dramatic ways. The chiral soliton model predicts only a $\overline{\mathbf{10}}_f$. First order perturbation theory in m_s predicts equal spacing between isomultiplets of decreasing hypercharge. None of the phenomena related to ideal missing of the $\mathbf{8}_f \oplus \overline{\mathbf{10}}_f$ occur. In particular in the chiral soliton model: a) There is no N lighter than the Θ^+, therefore no candidate for the Roper resonance; b) the N that is heavier than the Θ couples both to strange and non-strange channels. The N_s

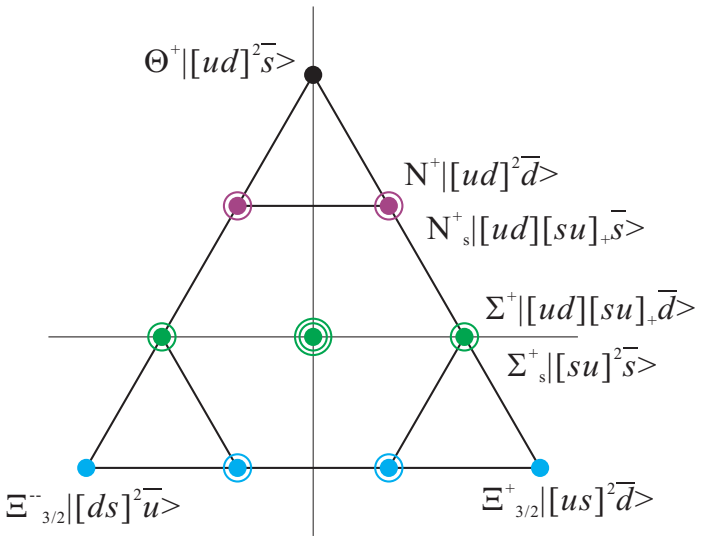

Figure 1-4: The quark content of representative members of the $(q^4\bar{q})$ $\overline{\mathbf{10}}_f$+$\mathbf{8}_f$ baryons in the di-quark model [2].

in the correlated quark picture should couple predominantly with hidden strangeness (like the $\phi(1020)$ or $f_0(980)$); c) the Ξ states are heaviest, above 2 GeV/c^2. In the correlated quark picture they are close to the N_s because they both contain two s-quarks. The prediction of light charge-exotic Ξ's is the modest distinctive signature of the di-quark model; d) There is no second multiplet of Σ's with hidden strangeness and no Λ. The striking departure of predicted mass splittings in the chiral soliton model from an approximate additive quark mass formula arises from the model's powerful embodiment of chiral flavor $SU(3) \times SU(3)$.

1.2 Experiment Results of Θ^+

Since the publication of the Diakonov paper in 1997, a series of new experimental searches have been conducted. A possible $S = 1$ baryon was reported in October 2002 by the LEPS Collaboration [24] in the reaction $\gamma n \to K^+K^-n$ from a ^{12}C target. A narrow exotic baryon state of $S = 1$ was seen in the missing mass spectrum of the K^-, $n(\gamma, K^-)X$, after removing events associated with the $\phi(1020)$ ($\phi \to K^+K^-$) and $\Lambda(1520)$ ($\Lambda \to K^-p$). The signal was found at 1.54 ± 0.01 GeV/c^2 with a width

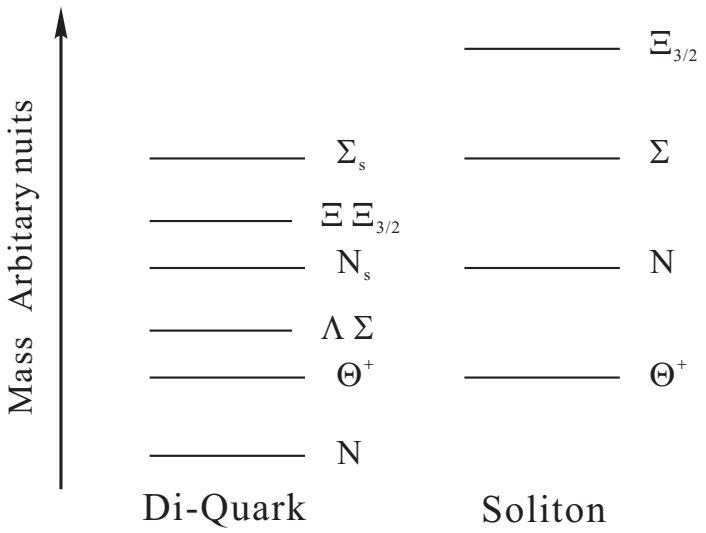

Figure 1-5: Relative masses of states in the ideally mixed $(q^4\bar{q})$ $\mathbf{8}_f \oplus \overline{\mathbf{10}}_f$, compared with the mass hierarchy in the chiral soliton model.

less than 25 MeV/c^2 and a Gaussian significance of 4.6 σ as in Figure 1-6. The real photon beam has range from 1.5 to 2.35 GeV. A Fermi momentum correction was applied due to the nature of the target[2].

Such a result has generated renewed experimental and theoretical interest in pentaquarks and was received with both enthusiasm and skepticism within the hadronic physics community. The following searches around the world were carried out and set out to either confirm or deny the existence of the Θ^+. Detailed reviews of experimental evidence can be found in the references [25][26][27]. Only a brief discussion about the results will be given here.

1.2.1 Positive Reports

The first five publications showing positive evidence for the Θ^+ are given in the left side of Table 1.1. Except LEPS, the other collaborations are: DIANA [28], CLAS [3], SAPHIR [29] and HERMES [7]. The quoted statistical significance in these papers is about 4-5 σ, although the uncertainties in the background under the peaks suggests that the statistical significance should have been smaller. Each of these experiments

[2]The Fermi momentum distribution of neutron was measured through the missing mass of $K^+\pi^-$ of the following channel $\gamma n \to K^+\Sigma^- \to K^+\pi^- n$.

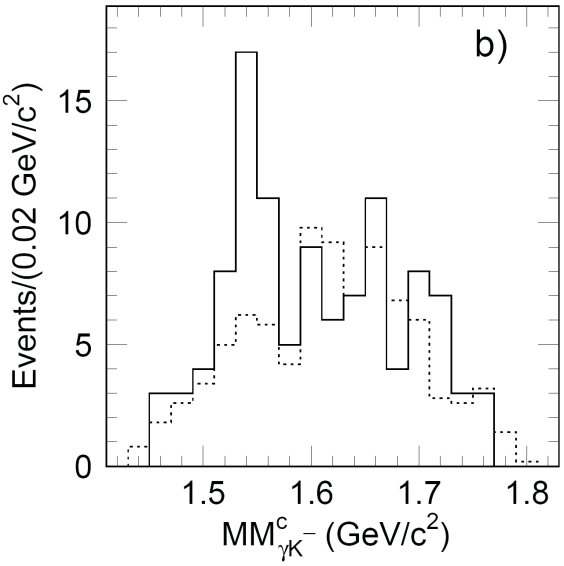

Figure 1-6: The $MM^C_{\gamma K^-}$ missing mass spectra (solid line) in the reaction $\gamma C \to K^- X$ on ^{12}C target from the LEPS collaboration. Dotted histogram is for events from the liquid hydrogen (LH_2) target normalized by a fit in the region above 1.59 GeV/c^2. The difference of the two plots shows the spectrum of reaction channel $\gamma n \to K^- X$. This is the first reported evidence for a $S = +1$ exotic baryon consistent with the prediction of the chiral soliton model.

Original Experiments			Repeat Measurements			
Group	Reaction	σ's	Group	Reaction	Inc.	Result
LEPS	$\gamma C \to K^+K^-X$	4	LEPS	$\gamma d \to K^+K^-X$	5	3-5 σ
DIANA	$K^+Xe \to K^0pX$	4	Belle	$K^+Si \to K^0pX$	10	$\Gamma < 1$ MeV/c^2
CLAS	$\gamma d \to K^+K^-pn$	5	CLAS	$\gamma d \to K^+K^-pn$	6	$\sigma_{tot} < 3$ nb
SAPHIR	$\gamma p \to K^+K^-n$	5	CLAS	$\gamma p \to K^+K^-n$	10	$\sigma_{tot} < 1$ nb
HERMES	$e^+d \to K^0pX$	4	BaBar	$e^+Be \to K^0pX$	100	No Θ^+ seen

Table 1.1: The first five positive Θ^+ publications (left side) and the results of repeat measurements with higher statistics (right side). The column labeled σ show the statistical significance quoted in the publications. The column labeled "Inc." shows the factor by which the number of counts in the mass spectrum increased.

has been repeated, sometimes by other groups, although the experimental conditions were not reproduced exactly. The "repeat" experiments are listed in the right side of Table 1.1.

The LEPS collaboration repeated their earlier experiment, except using a deuterium target rather than Carbon. And the statistics in the K^- missing mass spectrum was more than 5 times higher. The resulting spectrum has been published only in a conference proceeding [30] and shows a peak at the same mass as before. The statistical significance of this signal is likely in the range of 3-5 σ.

The DIANA results [28] are still viable, but just barely. These data are from old bubble chamber experiments using a K^+ beam on Xenon. Cuts are applied to reduce the background from kaon charge exchange. Their results were not reproduced directly, but are limited by analysis from the Belle Collaboration. For the Belle results, a kaon was tagged from D-meson decay, which interacts with Silicon in their vertex detector, followed by detection of pK^0 and pK^+ pairs. They estimate and subtract events from kaon charge exchange. The resulting mass spectrum does not show any Θ^+ peak. Belle's upper limit for Θ^+ production is below that calculated from the DIANA experiment, but still within one standard deviation of the DIANA result. While the Belle result does not entirely rule out the DIANA result, it puts a severe limit on the possible width of the Θ^+ at less than 1 MeV/c^2.

The original CLAS result used older data (called g2a) from deuterium that was analyzed quickly after the LEPS result was announced. The repeat of the CLAS result [4] is shown in Figure 1-7 by the solid histogram (which has been rescaled down by a factor of 5.92) overlayed on top of the original "g2a" data. In this comparison, the photon energy range was constrained to be the same in both analysis. Using the new data, the g2a "peak" is about a 3 σ fluctuation, and an upper limit of 3 nb on the total cross section was found.

The SAPHIR Collaboration were the first to publish a Θ^+ search using the $\gamma p \to K^+K^0n$ reaction [29]. One year later, the CLAS Collaboration measured the same reaction as SAPHIR, but with more than 10 times higher statistics [31]. The resulting Θ^+ mass spectrum was completely void of peaks, even when SAPHIRs data cuts and

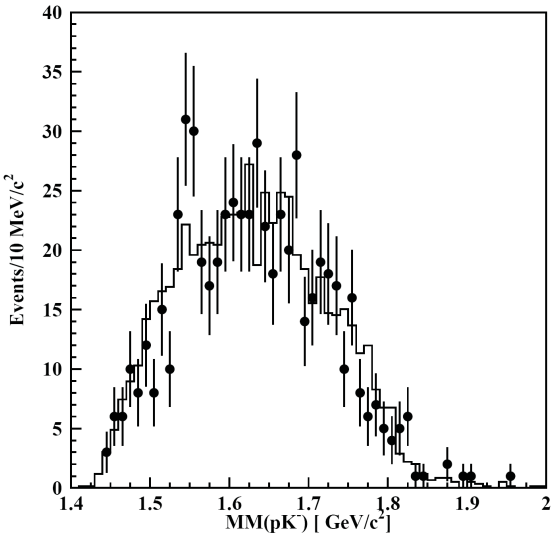

Figure 1-7: Comparison of the original CLAS data [3] (points with error bars) and the repeat measurement [4] (solid histogram, scaled down by a factor of 5.92).

photon energy range were applied. An upper limit of 1 nb was found for the total cross section.

The HERMES Collaboration [7] used high-energy e^+ on a fixed deuteron target to produce events with a K^0 and a proton. The invariant mass spectrum for K^0p pairs showed a peak near 1528 MeV/c^2, about 10 MeV/c^2 lower than the Θ^+ peak from other experiments. The BaBar experiment, using colliding e^+e^- beams, had some beam halo hit the Beryllium beam pipe in their detector. The resulting luminosity was large, and hence they had data for high-energy e^+ on a fixed Be target with high statistics. Their preliminary results [32] showed a smooth spectrum without any Θ^+ peak. Although there are questions in comparing the BaBar results from to those of HERMES since the mechanism of the Θ^+ production is still unknown, it seems that again the Θ^+ could not be reproduced.

There are still several early pentaquark searches that have positive results with high statistical significance, but have not yet been repeated. these experiments from the collaborations ITEP [33], ZEUS [34], CLAS [4] and COSY/TOF [35] are listed in Table 1.2.

One possible theoretical explanation for the contradictory results from LEPS,

Group	Reaction	σ's	Comment
ITEP	$\mu A \to pK^0X$	6-7	NOMAD μ experiment also sees a small peak
ZEUS	$e^+p \to pK^0X$	$\sim$4.5	new data with improved vertex detector is being analyzed
CLAS	$\gamma p \to \pi^+K^-K^+n$	7-8	needs 5.5 GeV beam; might be rerun in 2008?
COSY	$pp \to \Sigma^-K^0p$	$\sim$5	new data with 5 times higher statistics is being analyzed

Table 1.2: Publications with positive evidence for the Θ^+ that have not yet been repeated with higher statistics. As before, the statistical significance (σ's) is that given in the published paper.

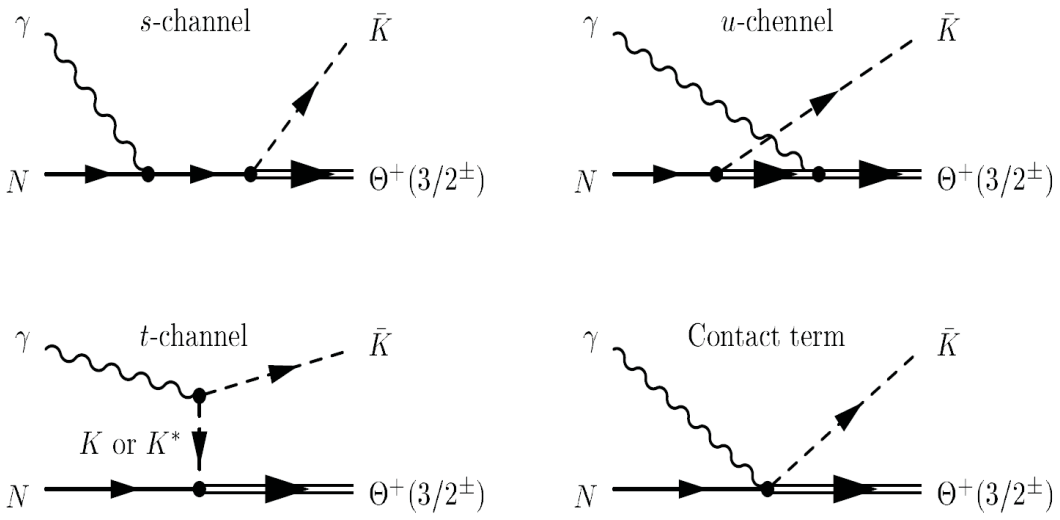

Figure 1-8: Born diagrams calculated in the effective Lagrangian method.

CLAS and SAPHIR was proposed by Nam, Hosaka and Kim [36], provided that the Θ^+ has spin-parity $J^P = 3/2^+$. In the paper, they argue that for Θ^+ production, the s- and u-channel diagrams, defined as in Figure 1-8, are suppressed compared with the t-channel and the contact term. They also note that the contact term is present only for production on the neutron. For $J = 3/2$ in their model, they find that the contact term dominates by a factor of 25-50 over K^* exchange in the t-channel. Hence it is possible to see the Θ^+ at LEPS (for production from the neutron) and not see it for the SAPHIR reaction (using a proton target), provided the width of the Θ^+ is 1 MeV/c^2 or less. Furthermore, their calculation for $J^P = 3/2+$ gives almost all

of the cross section at forward kaon angles, where the CLAS data has a hole in the acceptance.

1.2.2 Null Results

The negative Θ^+ results mainly come from either electro-position colliders (BES [37], BaBar [32], Belle [38], LEP [39]) or from high-energy reactions using a hadron beam (such as HERA-B [40], SPHINX [41], HyperCP [42] and CDF [43]). Because of the difficulty in detecting neutrons in these detectors, these experiments look at the pK_s^0 invariant mass. These high energy experiments typically have higher statistics yet see no Θ^+ peak. The major argument for not seeing Θ^+ in high energy experiments rather than medium energy experiments is of different mechanisms [25][44].

1.2.3 Width of Θ^+ from Partial Wave Analysis

Shortly after the first Θ^+ papers [24][28][3][29] were published, some comparisons with the the K^+N data using partial wave analysis (PWA) were done. Nussinov [45] was one of the first, and based on the general expression for the K^+n total cross section from deuteron target evaluated on-resonance (with the phase shift at 90°) and the momentum needed to reach the Θ^+ mass, he finds a 37 mb value. If the Θ^+ is narrow, it could escape detection if there is a gap in the database at the resonant energy, but the deuteron's Fermi motion will spread it out so that it should be noticeable. Using these estimates and a cursory examination of the database, Nussinov concludes that the width of the Θ^+ must be less than 6 MeV/c^2. Other estimates of the width followed, using similar but perhaps more careful approaches (e.g. [46] [47]) and all of these agree that the Θ^+ width must be less than a few MeV/c^2 to be consistent with the K^+N total cross section.

One comparison to the KN database by Gibbs [48] is particularly interesting. This paper is based on a weak scattering approximation and the resulting calculation is compared with the total cross section data of reference [49]. The paper concludes that in all cases, the width of Θ^+ must be unusually small, on the order of 1 MeV/c^2.

1.3 Other Partner States in the Anti-Decuplet

The chiral soliton model predicted three manifestly exotic baryon states with the Θ^+ being the lightest one, and two $S = -2$ exotic Ξ states, Ξ^{--} and Ξ^0, within the baryon anti-decuplet. The first evidence of a possible $\Xi^{--}_{3/2}$ state was also reported by the NA49 collaboration [5]; a doubly negatively charge baryon with $S = -2$ was seen at 1860 MeV/c^2 decaying to $\Xi^-\pi^-$. Figure 1-9 shows the combined $\Xi^-\pi^-$, $\Xi^-\pi^+$, $\overline{\Xi}^+\pi^-$ and $\overline{\Xi}^+\pi^+$ invariant mass spectra, with the $\Xi{--}_{3/2} \to \Xi^-\pi^-$ being the exotic baryon candidate, and a possible isospin partner $\Xi^0_{3/2}$ decaying into $\Xi^-\pi^+$ observed at the same mass.

The evidence of the $\Xi^{--}_{3/2}$ as another marker of the anti-decuplet of pentaquarks is intriguing and injected more excitement into the hadron spectroscopy community.

Reference [44] reconsidered the identity of $N(1710)$ state as a member of pentaquark anti-decuplet, N_5. And they concluded that the $N(1710)$ is not the appropriate candidate for N_5 together with the Θ^+. Instead, they suggest if the states $\Xi^{--}_{3/2}$ and Θ^+ are indeed members of the same anti-decuplet, then according to the Gell-Mann-Okubo rule, the mass difference of two neighboring isospin multiplets in the anti-decuplet should be constant and equal

$$(M_{\Xi_{3/2}} - M_\Theta)/3 \approx 107 \text{ MeV}/c^2. \tag{1.3}$$

This gives M_{N_5} ≈1650 MeV/c^2 and M_{Σ_5} ≈1755 MeV/c^2. Their following work in the framework of the soliton picture suggests that a Θ^+ width of about 1 MeV/c^2 implies that its non-strange partner in the $SU(3)_f$ anti-decuplet may have a total decay widths around 10 MeV/c^2 or less. So that the N_5 state would be wider than the Θ^+, though still narrow. All early proposed candidates from particle data group (PDG) have much wider width than this (>50 MeV/c^2) and it's implied that the N_5 has not been observed up to now.

Further works from partial wave analysis (e.g. [50]) suggest that if Θ^+ pentaquark exists then other members of its symmetry group and/or other multiplets (**27**-plet and $\overline{\mathbf{35}}$-plet) containing exotic states should be observable as well but can only be detected

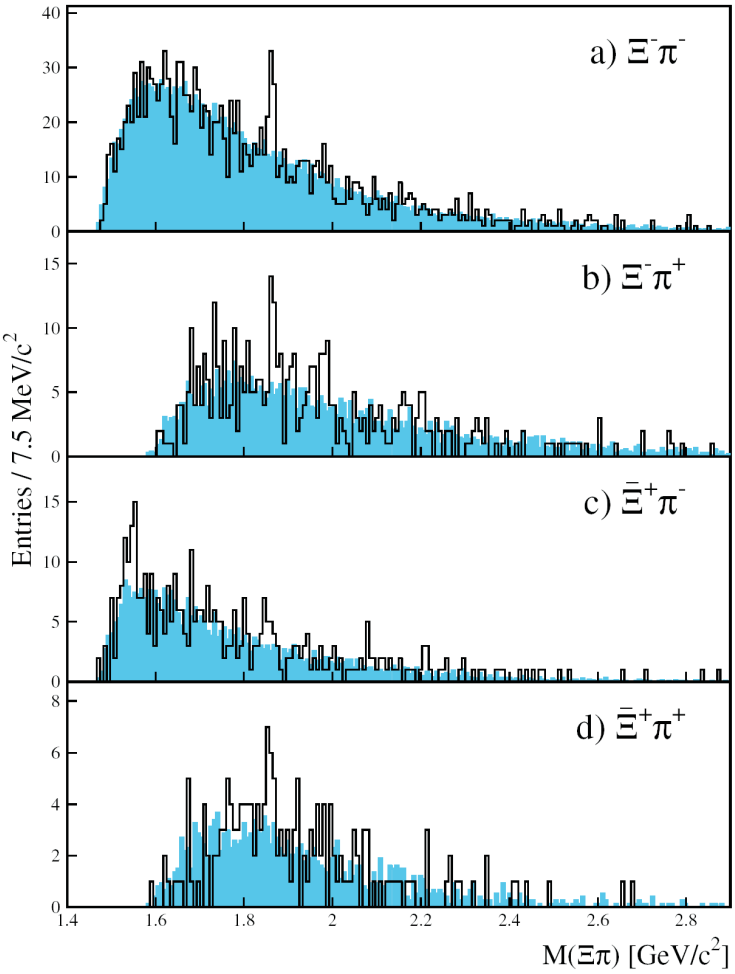

Figure 1-9: Invariant mass spectra after selection cuts for : a) $\Xi^-\pi^-$; b) $\Xi^-\pi^+$; c) $\overline{\Xi}^+\pi^-$ (note that the $\Xi^0(1530)$ state is also visible) and d) $\overline{\Xi}^+\pi^+$ from reference [5]. The shaded histograms are the normalized mixed-event backgrounds.

by high resolution experiments, provided they are much narrower (<1 MeV/c^2) than current experimental resolution ∼10 MeV/c^2.

1.4 Θ^+ as an Isotensor Pentaquark

To explain the narrow width and low mass of pentaquark Θ^++ an isotensor multiplet of Θ^+ was proposed by Simon Capstick *et al.* in reference [51].

Any state with the structure $qqqq\bar{q}$, for any flavors, has as a possible color configuration a set of three quarks in a colorless (baryon) state, plus a quark and anti-quark in a colorless (meson) state. This means that by a simple rearrangement of the color configuration, the state can "fall apart" into a baryon and meson, with only weak forces between the two colorless hadrons. Therefore the Θ^+ state which is 110 MeV/c^2 above the threshold should have a decay width of the order of 500 MeV/c^2 unless its decays are suppressed by phase space, symmetry or special dynamics.

The largest phase space for the fall-apart decay of an isoscalar or isovector $\Theta^+ \to nK^+$ will be when the Θ^+ has $J^P = 1/2^-$ and so it decays in an S-wave. If the width of such a S-wave decay is 500 MeV/c^2, the 10 MeV/c^2 width of Θ^+ can only be achieved with the decay proceeds in F-wave or higher, i.e., the total angular momentum J of Θ^+ is $\leq 5/2$ for a parity $P = +1$ Θ^+ or $J \leq 7/2$ for $P = -1$. However, this scheme is very unlikely for such a light ground state resonance, as the addition of orbital angular momentum will significantly increase its energy.

From the view of symmetry, if Θ^+ has isospin $I = 2$, the decay $\Theta^+ \to nK^+$ becomes isospin-symmetry violating. This is not the case if the Θ^+ is isoscalar or isovector. It is shown that isospin symmetry violating decay widths are typically 0.1% of isospin conserving widths. For the $I = 2$ Θ^+ state, the the isospin projection $I_z = 0$ member of the multiplet are depicted in Table 1.3. The mass splitting in the Θ multiplet is expected to be less than 10 MeV/c^2. Since Θ^+ is below $NK\pi$ threshold by about 30 MeV/c^2, its isospin partners are also below the threshold. This precludes the strong decays $\Theta \to NK\pi$; specifically $\Theta^- \to n\pi^- K^0$ and $\Theta^{++} \to n\pi^+ K^+$. Thus, these states must decay weakly.

State	Quarks	I_z	Decay modes
Θ^-	$dddd\bar{s}$	-2	
Θ^0	$uddd\bar{s}$	-1	nK^0
Θ^+	$uudd\bar{s}$	0	nK^+, pK^0
Θ^{++}	$uuud\bar{s}$	1	pK^+
Θ^{+++}	$uuuu\bar{s}$	2	

Table 1.3: Quark content, I_z and strong decay modes of Θ states.

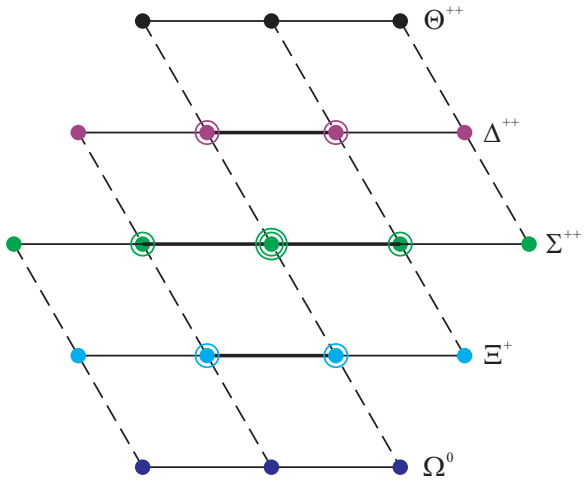

Figure 1-10: Structure of a possible baryon **27**-plet, for non-violated $SU(3)_f$.

In the deuteron target experiment at CLAS, it should be possible to produce the isospin partner Θ^{++} of the Θ^+ by the reaction $\gamma d \to \Theta^{++} K^- n \to p K^+ K^-$, and detect it by examining the invariant mass of the K^+p system [52]. It may be the case that production of the Θ^{++} is suppressed relative to that of the Θ^+. If, as is common in kaon photo-production experiments,the reactions $\gamma n \to K^- \Theta^+$ and $\gamma p \to K^- \Theta^{++}$ result in forward peaked K^- distributions, these negatively charged particles will be bent into the beam direction by the CLAS magnetic field and will go largely undetected, unless they scatter off the spectating neutron. Scattering cross sections for K^-n are considerably smaller than those of K^-p where they are measured, at kaon beam energies of 600 MeV/c^2 or higher [53]. Thus, if the K particles are forward peaked and the K^-n cross section remains small down to low energies, it is likely that the Θ^{++} will remain undetected without a larger data sample.

Another prediction for the double charge pentaquark Θ^{++} comes from the **27**-plet

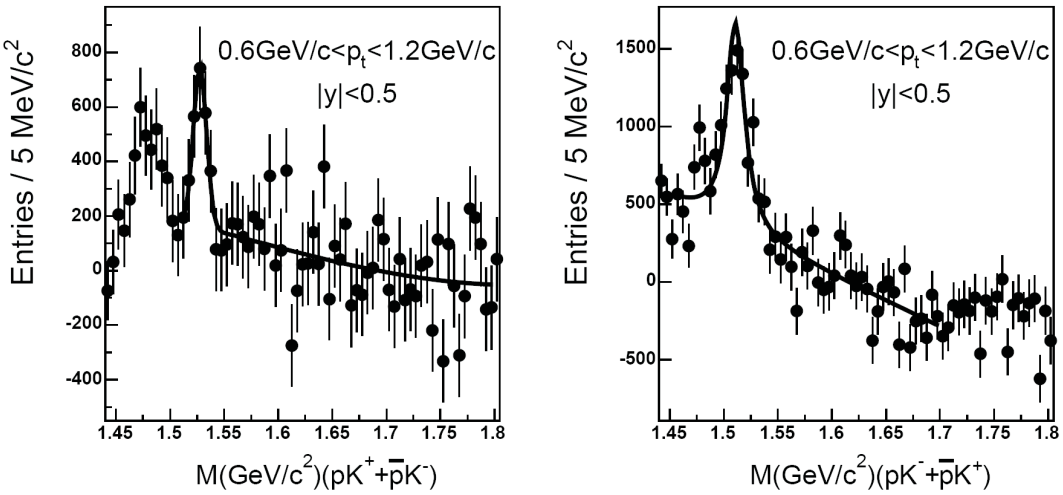

Figure 1-11: Invariant mass distributions of $pK^+ + \bar{p}K^-$ (left) and $pK^- + \bar{p}K^+$ (right) from d+Au collisions at 200 GeV/c^2 after the subtraction of combinatorial background from reference [6]. The curves are a fit of Gaussian and polynomial function.

of chiral soliton model [19][21][22], as show in Figure 1-10. The predicted mass for such state is heavier than the Θ^+ and ranges from 1640 to 1740 MeV/c^2 and the predicted width according to PWA is either too wide (few hundreds of MeV/c^2) to be separated from background or too narrow (<1 MeV/c^2) which would be suppressed by the much wider resolution of current experiments (>10 MeV/c^2) [50].

Several searches for the Θ^{++} in K^+p invariant mass distributions have been published [54][7][6][34]. The only positive report comes from STAR at RHIC [6]. An intriguing peak was observed in the invariant mass distribution of $pK^+ + \bar{p}K^-$ from 18.6 Million d+Au collision events at $\sqrt{S_{NN}} = 200$ GeV/c^2. The peak centers at a mass $1528 \pm 2 \pm 5$ MeV/c^2 and the FWHM$\sim$15 MeV/c^2 is limited by detector responses (see Figure 1-11). The statistical significance of the peak is 4.2 σ. However, the similar search they performed in the Au+Au events yield no significant signal at same place. But the Au+Au did not offer enough statistics to rule out the possibility of such signal due to overwhelming combinatorial backgrounds.

The remaining experiments all show negative results. This result may not be surprising because of their wide mass resolution [50]. Figure 1-12 shows the result

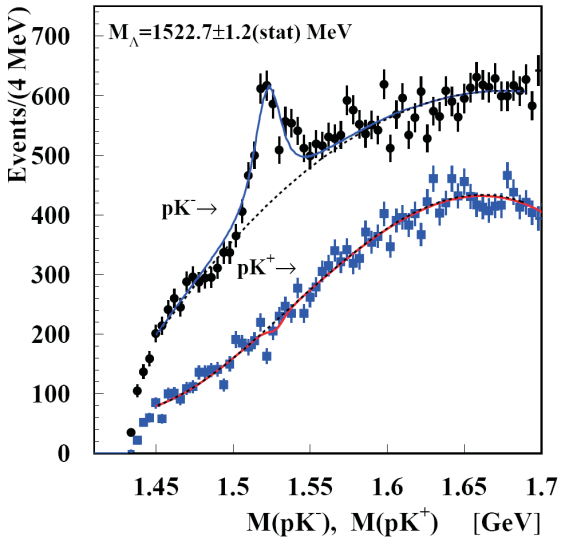

Figure 1-12: Spectra of M_{pK^-} (top) and M_{pK^+} (bottom) from reaction $e^+d \rightarrow K^+K^-pX$ [7]. A clear peak is seen for the $\Lambda^0(1520)$ in the M_{pK^-} invariant mass distribution.

from HERMES.

1.5 Opportunity for Jefferson Lab Hall A

According to previous discussions, most of current experiments suffer from their wide experiment resolutions so that it's hard to clearly identify or rule out the pentaquark states. Jefferson Lab Hall A is an ideal place for the pentaquark search because of its pair of high resolution spectrometers (HRS) and the normal missing mass resolution is about 1 MeV/c^2. Such good resolution brings an extremely high sensitivity to narrow structures than any other previous experiments with mass resolution larger than 10 MeV/c^2. The high luminosity electron beam will also provides sufficient statistic. Actually, back to 1999, H. Gao and B.-Q. Ma already suggested a similar search for Θ^{++} in the missing mass of electro-production $ep \rightarrow e'K^-X$ in Jefferson Lab. However the pentaquark didn't grasp so many interests from nuclear physics community at that momentum.

The Jefferson Lab Experiment E04-012 [8] was proposed and approved by the end

of 2003 to search for Θ^{++} and other two non-exotic anti-decuplet members N_5^0 and Σ_5^0 in electro-production. These three states were searched in the missing mass spectra of the following channels: $H(e,e'K^+)\Sigma_5^0$, $H(e,e'\pi^+)N_5^0$ and $H(e,e'K^-)\Theta^{++}$. The result of this experiment which is described in this thesis will bring an important input to the debate about the existence of pentaquarks.

Chapter 2

The Experiment

2.1 Overview

During the early summer of 2004, the high resolution search of pentaquark partners experiment, E04-012, was performed in Hall A of Thomas Jefferson National Accelerator Facility (Jefferson Lab, or JLab; formerly known as Continuous Electron Beam Accelerator Facility, or CEBAF). A 5 GeV CW electron beam was incident on a 15 cm extended liquid hydrogen target. Scattered electrons were detected in the right side High Resolution Spectrometer (HRS) in coincidence with electro-produced hadrons in the left side HRS. The pentaquark states Σ_5^0, N_5^0 and Θ^{++} were searched in the missing mass spectra of the following three reaction channels:

$$H(e, e'K^+)\Sigma_5^0$$
$$H(e, e'\pi^+)N_5^0$$
$$H(e, e'K^-)\Theta^{++}.$$

Each spectrometer was coupled with a SEPTUM magnet to catch paticles at 6° forward angle to have the produced mesons, π or K, in the same direction of virtual photon emitted by the electron scattering. The reason to use such forward angle is the expection of a similar t-channel dominated process of pentaquarks as of the production of $\Lambda^0(1520)$ [8], see Figure 1-8. In the right arm, electrons were selected by a Gas Cherenkov detector. In the left arm, two Aerogel Cherenkov detectors,

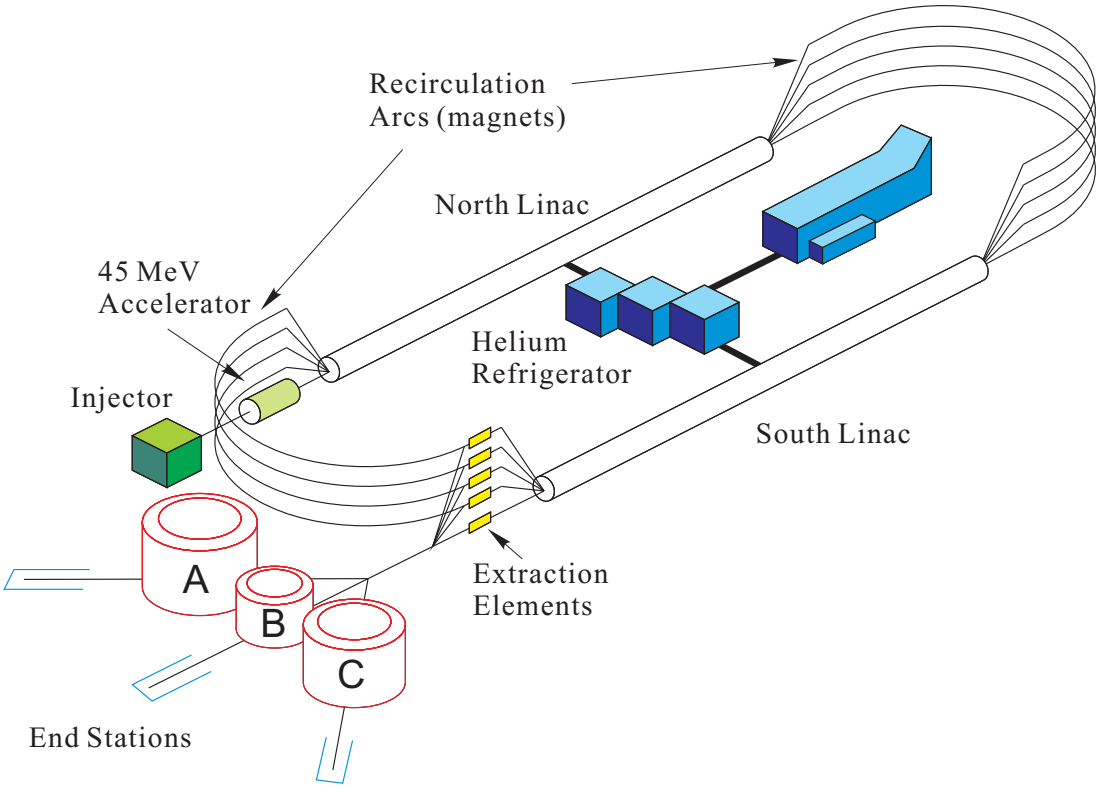

Figure 2-1: The Jefferson Lab Accelerator.

one Ring Imaging Cherenkov detector (RICH) and a pair of lead glass detector, Pion rejector, were combined to identify K^+, K^- and π^+.

2.2 Accelerator

Jefferson Lab, the world's premier medium energy electron scattering laboratory, is located in Newport News, Virginia. The facility consists of a state-of-the art continuous wave (CW) electron accelerator, three complementary experiment halls that utilize the beam to explore different aspects of nuclear physics, a free electron laser facility and an applied research center.

The 7-furlong (7/8 of a mile) accelerator was designed to deliver polarized electron beam up to 6 GeV to three halls simultaneously using radio frequency (RF) technique. Its two straight super-conducting linear accelerators (linac) are connected by 180° arcs to form a unique "racetrack" recirculating beamline, see Figure 2-1. Both

of the linacs are lined up with twenty RF cryomodules, each containing eight superconducting niobium 5-cell cavities, as show in Figure 2-2. Liquid helium, produced at the Central Helium Liquefier (CHL), keeps the accelerating cavities superconducting at a temperature of 2 Kelvin. Quadrupole and dipole magnets in each arc provide the field which focus and steers the beam as it passes through each arc. More than 2,200 magnets are necessary to keep the beam on a precise path and tightly focused.

In the injector, the electron source with current up to 200 μA current is polarized up to 85% by illumating a strained superlattice GaAs cathode with polarized laser light. An RF chopping system operating at 499 MHz is used to develop a 3-beam 1497 MHz bunch train at 100 keV. The beam is then longitudinally compressed in the bunching section to provide 2 picoseconds bunches, which are then accelerated to 45 MeV and injected into north linac. The linac energies are each set identically and the RF cavities are phased to provide maximum acceleration. The nominal gain of each linac can be set from 400 to 600 MeV, therefore after maximum 5 rounds, the energy of electron beam can range from 0.8 GeV to maximum 6.07 GeV.

After passing through the south linac, the beam can be either circle around the west recirculation arc for another round or be directed into a hall's transport channel using magnetic or RF extraction. The RF scheme uses 499 MHz cavities, which kick every third bunch out of the machine to a designated hall.

During this experiment period, an averaged 5 GeV CW beam was delivered into Hall A for production data taking with energy spread less than 5×10^{-5} and the current was typically 15 μA.

2.3 Hall A

All three experiment halls have their bulk volumes underground with shield of concrete and a thick layer of earth. Hall A is the largest one with a diameter of 53 m. Figure 2-3 shows the configuration of Hall A during the experiment E04-012. The central elements include the beamline, cryogenic target in the scattering chamber and two High Resolution Spectrometers (HRS).

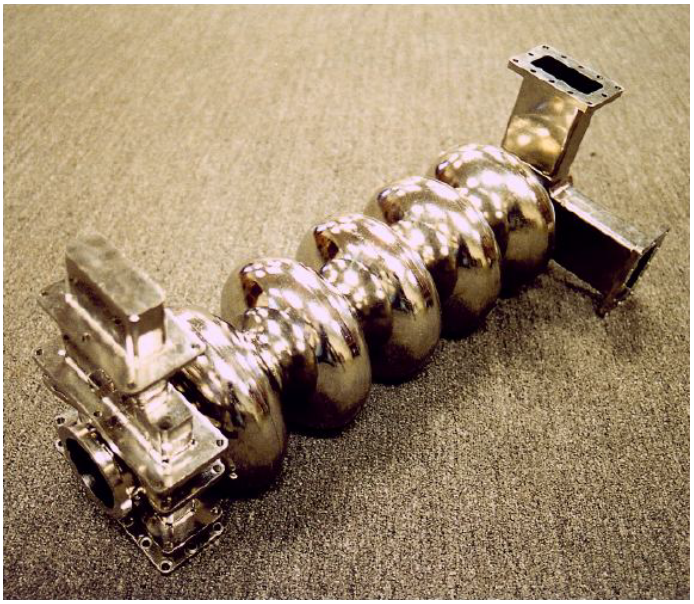

Figure 2-2: The RF accelerating unit.

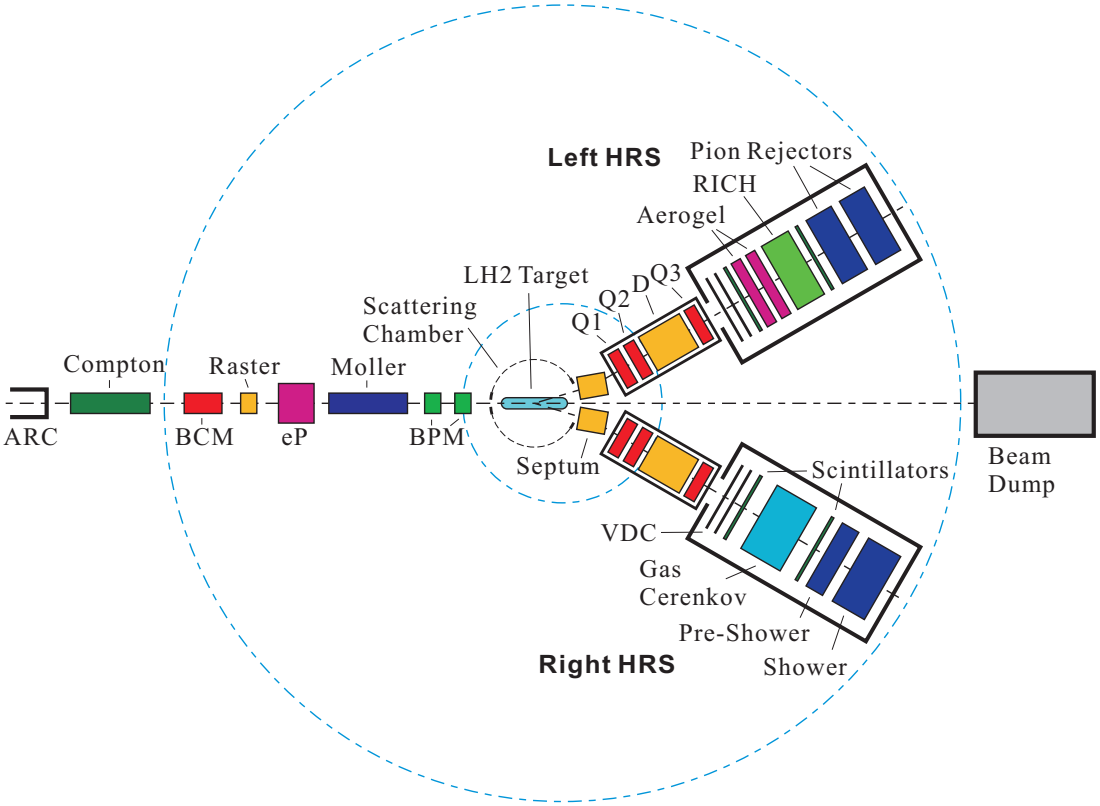

Figure 2-3: Hall A Configuration during E04-012.

As the electron beam is incident on the target, the right HRS serves as a electron arm and the left HRS detects recoiled hadrons. Both HRSs feature 3 quadrupoles and 1 dipole magnets and the combination provides a momentum resolution of better than 2×10^{-4} and a horizontal angular resolution of better than 2 mrad at a designed maximum central momentum of 4 GeV/c. However due to large volume of HRS, they can only be positioned at a angle larger than 12.5 degrees. To achieve the requested 6 degrees, two SEPTUM [55] magnets were installed to bend the scattered charged particles by additional 6.5 degrees.

2.4 Beam Line

The instrumentation along the beam line consists of various elements necessary to transport the electron beam onto the target and into the dump, and to measure simultaneously the relevant properties of the beam.

2.4.1 Beam Energy Measurement

The beam energy during the experiment was monitored by "Tiefenbach" value. This value uses the current values of Hall A arc Bdl value and Hall A arc beam position monitors (BPM) to calculate the beam energy. This number is continuously recorded in the data stream and is calibrated against the Arc energy of the 9th dipole regularly. Due to it's high accuracy, less than 1 MeV, there was no invasive measurement performed during the experiment.

The energy spread $\delta p/p$ of beam is potentially a big factor of the missing mass resolution. To monitor it, the online synchrotron light interferometry (SLI) [56] was used. The Hall A SLI was developed for new experiments' growing requirements of small transverse beam size ($\sigma_{x,y} < 20\ \mu m$) and low energy spread ($\delta p/p < 3 \times 10^{-5}$) but also allows for continuous monitoring at a critical point of the accelerator. This technique was firstly introduced at KEK, Japan [57] and is essentially a wave front division interferometer that uses polarized quasi-monochromatic synchrotron light.

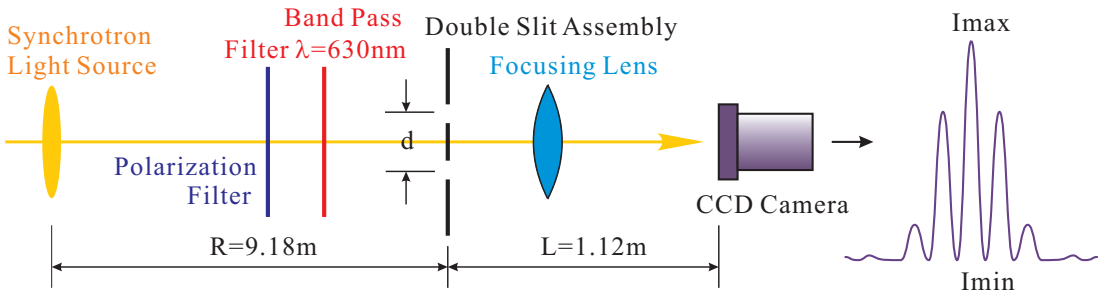

Figure 2-4: The Hall A SLI Energy Spread Measurement.

The transverse beam size σ_{beam} measured in a dispersive location has two sources:

$$\sigma_{beam} = \sqrt{\sigma_\beta^2 + \sigma_\delta^2}, \tag{2.1}$$

where $\sigma_\beta = \sqrt{\epsilon\beta}$ is the betatron size and σ_δ is the size due to dispersion [58]. The energy spread is $\frac{\sigma_E}{E_0} = \frac{\sigma_\delta}{D}$, where D is the local dispersion. Ignoring the betatron contribution (which is reasonable when $\sigma_\beta/\sigma_\delta << 1$), the upper limit on the energy spread is

$$\frac{\sigma_E}{E_0} < \frac{\sigma_{beam}}{D}. \tag{2.2}$$

When the beam has small energy spread, as is the case with the JLab Beam, σ_β can be comparable to σ_δ and the betatron contribution to the transverse beam size must be taken into account to determine the central value of the energy spread. In order to minimize the betatron contribution to the beam size, as well as the effect of incoming dispersion, a special optics was devised for the end station transport line to increase the dispersion from 4 m (nominal) to 8 m (high dispersion).

Figure 2-4 shows the sketch of SLI. The synchrotron light generated by the electron beam in the dipole magnet is extracted through a quartz window by the mirror installed in a vacuum chamber. A polarization filter selects out the σ-polarized component and a band optical filter with $\lambda_0 = 630 \pm 10$ nm is used to obtain a quasi-monochromatic light. After passing through a double slit assembly, the interference pattern is captured by a CCD camera. The double slit has different sets of slits with separation d between 5 to 20 mm and it is moved by a remotely controlled

stepper-motor.

The beam size is a function of the visibility V which is estimated from the intensities of the first (central) maximum (I_{max}) and minimum (I_{min}) of the interferogram:

$$V = \frac{I_{max} - I_{min}}{I_{max} + I_{min}}. \tag{2.3}$$

For a Gaussian beam distribution the RMS beam size is found to be:

$$\sigma_{beam} = \frac{\lambda_0 R}{\pi d}\sqrt{\frac{1}{2} ln(1/V)}, \tag{2.4}$$

where R is the distance between the light source and slit.

As a result, the beam energy used in whole experiment was determined to be $E_0 = 5009.28$ MeV while the energy spread was about $\delta p/p = 5 \times 10^{-5}$.

2.4.2 Beam Current Monitor

The beam current was measured by the Beam Current Monitor (BCM) in Hall A, which provides a stable, low-noise, no-invasive measurement [59]. It has an Unser monitor, two RF cavities, associated electronics and a data-acquisition system. The cavities and the Unser monitor are enclosed in a temperature-stabilized magnetic shielding box which is located 25 m upstream of the target.

Figure 2-5 shows the setup of BCM. The Unser monitor is a Parametric Current Transformer which provides an absolute reference [60]. The monitor is calibrated by passing a known current through a wire inside the beam pipe and has a nominal output of 4 mV/μA. As the Unser monitor's output signal drifts significantly on a time scale of several minutes, it is not suitable for continuous monitoring. However, the drift can be measured during the calibration runs and the net measured value is used to calibrate the two RF BCMs. The two resonant RF cavity monitors on either side of the Unser monitor are stainless steel cylindrical high-Q ($\sim$3000) waveguides which are tuned to the frequency of the beam (1497 MHz) resulting in voltage levels at their outputs which are proportional to the beam current. Each of the RF output

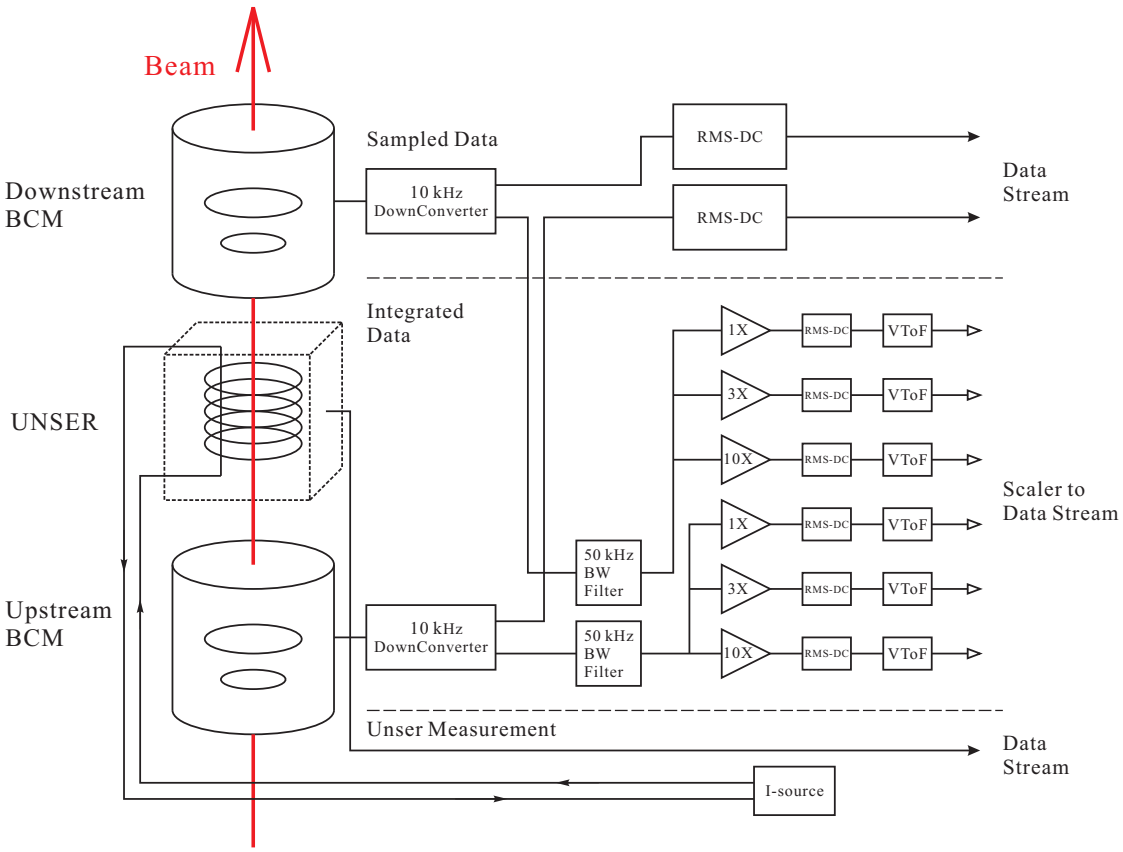

Figure 2-5: The Hall A BCM Configuration.

signals from the two cavities is split into two parts: to be sampled or integrated.

The signals to be sampled are processed by a high-precision digital multi-meter (DMM), HP3458A, and each second this device gives a digital output proportional to the RMS of beam current during that second. Signals from both cavities' and Unser's multimeter's are transported through GPIB ports and are recorded by the data logging process every 1-2 s. The signals to be integrated are sent to an RMS-to-DC converter to produce an analog DC voltage level and this level drives a Voltage-To-Frequency (VTOF) converter. These frequency signals are then fed to 200 MHz VME scalers and the outputs are injected into the data stream along with other scaler information. These logged scalers accumulate during the run and provide a number proportional to the time-integrated voltage level which accurately represents the total delivered charge. The regular RMS to DC output is linear for currents from about 5 μA to 200 μA. So a set of amplifiers has been introduced with gain factors of 1, 3 and 10 to lower currents at the expense of saturation at high currents. Hence, there is a set of three signals coming from each RF BCM. These six signals are fed to scaler inputs of each spectrometer, providing redundant beam charge information.

The beam charge can be derived from BCM scaler reading as

$$Q_{\mathrm{BCM}\times A,H} = \frac{\frac{N_{\mathrm{BCM}\times A,H}}{\mathrm{clock}_H} - \mathrm{offset}_{\times A,H}}{\mathrm{constant}_{\times A}} \mathrm{clock}_H, \tag{2.5}$$

where A=1, 3 or 10 is the gain factor, H=plus, minus or ungate is the beam helicity state and clock_H is the total clock time of corresponding helicity gate. The BCM calibration is typically performed every 2-3 months and the results are stable within $\pm 0.5\%$ down to a current of 1 μA.

2.4.3 Raster and Beam Position Monitor

To determine the position and direction of the beam at the target location, two Beam Position Monitors (BPMa and BPMb) were placed 7.345m and 2.214 m upstream of the Hall A center[1] respectively.

[1]See section A.1.1 for Hall A coordinate definitions.

The standard difference-over-sum technique is used to determine the relative position of the beam to with 100 μm for currents above 1 μA [61, 62]. The absolute position of the beam can be determined from the BPMs by calibrating them with respect to wire scanners (superharps) which are located adjacent to each BPM. The wire scanners are regularly surveyed with respect to the Hall A coordinates and the results are reproducible at the level of 200 μm. The position information from the BPMs are recorded in the raw data stream by two ways: average value and event-by-event. The real beam position and direction at the target can be reconstructed using the BPM positions calculated from 8 BPM antennas' readout (2×4):

$$\begin{aligned} x, y_{\text{target}} &= \frac{x, y_{\text{BPMa}} \cdot \Delta z_{\text{BPMb}} - x, y_{\text{BPMb}} \cdot \Delta z_{\text{BPMa}}}{z_{\text{BPMb}} - z_{\text{BPMa}}} \\ \vec{x}_{\text{beam}} &= \frac{\vec{x}_{\text{BPMb}} - \vec{x}_{\text{BPMa}}}{|\vec{x}_{\text{BPMb}} - \vec{x}_{\text{BPMa}}|}, \end{aligned} \tag{2.6}$$

where $\Delta z = z_{\text{BPM}} - z_{\text{target}}$.

For liquid or gas targets, high current beam (> 5 μA) may damage the target cell by overheating it. To prevent this, the beam is rastered by two pairs of horizontal (X) and vertical (Y) air-core dipoles located 23 m upstream of the target, and the size of rastered beam is typically several millimeters. The raster can be used in two modes, sinusoidal or amplitude modulated. In the sinusoidal mode both the X and Y magnet pairs are driven by pure sine waves with relative 90° phase, and frequencies, $\sim$ 18.3 kHz, which do not produce a closed Lissajous pattern. In the amplitude modulated mode both X and Y magnets are driven at 18 kHz with a 90° phase between X and Y, producing a circular pattern. The radius of this pattern is changed by amplitude modulation at 1 kHz.

During the experiment, a 2mm × 2mm sinusoidal mode raster was used with average 15 μA beam on the cryogenic liquid hydrogen target. Figure 2-6 shows the beam profiles measured by BPMs and the projection on target position.

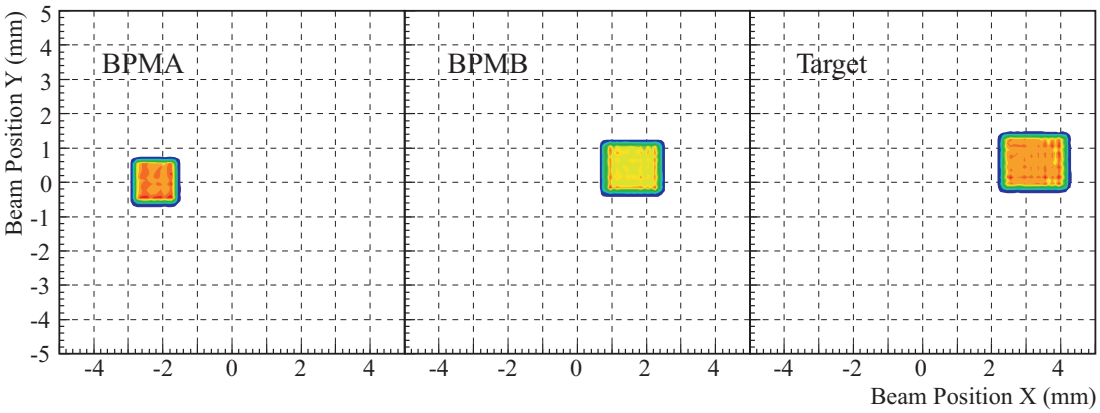

Figure 2-6: The Raster Size Measured during the experiment.

2.5 Target

2.5.1 Scattering Chamber

The scattering vacuum chamber [63] consists of several rings, supported on a 607 mm diameter central pivot post. The stainless steel base ring has one vacuum pump-out port and other ports for viewing and electrical feed-throughs. The middle ring is made of aluminum with average diameter = 1.092 m and located at beam height with 3 windows to cover full angular range and and beam entrance port. One of the windows is centered on the beamline covering $\pm 13.0^{\circ}$ to allow septum magnets to reach scattering angles from 6 - 12 degrees on either side of the beamline. The other windows ranged from 30 - 173.7 degrees and are specially designed for later experiments using BigBite large acceptance spectrometer [64]. In E04-012 configuration, the side windows were covered with a pair of flanges with thin aluminum foils. The upper ring is used to house the cryotarget. The scattering chamber has two flat covers, one for the middle ring and one for the top hat. The chamber vacuum is maintained at 10^{-6} Torr to insulate the target and to reduce the effect of multiple scattering.

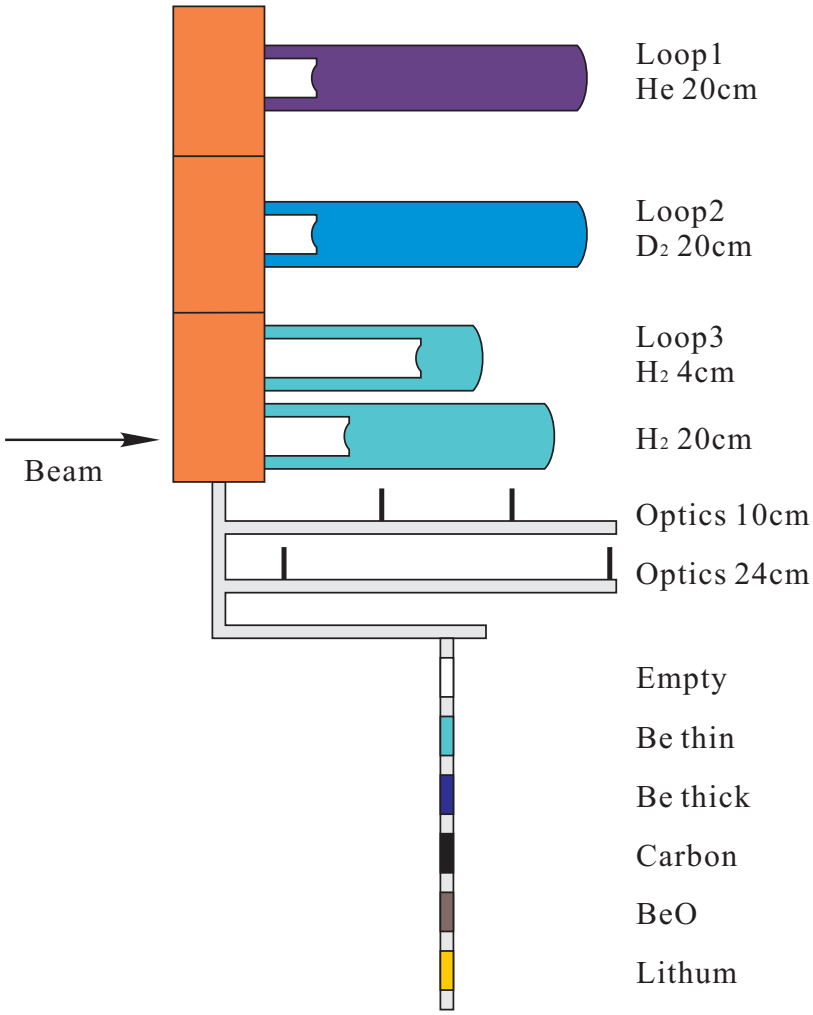

Figure 2-7: Side view of the Hall A cryotarget.

2.5.2 Cryogenic Target

A 15 cm liquid hydrogen cryogenic target [65] was used for the experiment's production data taking. The target system was mounted inside the scattering chamber along with sub-systems for cooling, gas handling, temperature and pressure monitoring, target control and motion, and an attached calibration and solid target ladder (see Figure 2-7).

The target system had three independent target loops: a liquid hydrogen (LH_2) loop, a liquid deuterium (LD_2) loop and a gaseous helium loop. The LH_2 loop had two aluminum cylindrical target cells, 15 cm and 4 cm length, mounted on the vertical

stack which can be moved from one position to another by remote control. Both the LD_2 and gaseous helium loops had only single 20 cm aluminum cell. All the liquid target cells had diameter ϕ=63.5 mm, and the side walls were 178 μm thick, with entrance and exit windows approximately 71 and 102 μm thick, respectively. The upstream window consisted of a thick ring holder with an inner diameter of 19 mm, large enough for the beam to pass through.

Below the cryogenic targets were two sets of carbon foil optics targets constucted of two thin pieces of carbon foils spaced by 10 or 24 cm. A solid target, attached at the bottom, had six target positions: an empty target, two Be targets with different thickness, a single carbon foil (can also be used for optics data taking), a BeO foil (typically used for direct beam observation), and a lithium target.

The LH_2 (LD_2) target were sub-cooled by 3 K at 19 K (22 K) with pressure of 0.17 MPa (0.15 MPa), about 3 K below their boiling temperature. Under this condition, they have a density of about 0.0723 g/cm^3 and 0.167 g/cm^3. The nominal operating condition for ^{4}He (^{3}He) was 6.3 K at 1.4 MPa (1.1 MPa). The coolant (helium) was supplied by the End Station Refrigerator (ESR). The helium from ESR is available at 15 K with a maximum cooling power of 1 kW, and at 4.5 K with a lower maximum cooling capacity near 600 W. Typically 15 K coolant is used for liquid cells while 4.5 K for gaseous cells. At the full 1 kW load of 15 K coolant, up to 130 μA beam current may be incident on the liquid target with temperature slightly over 20 K. In this configuration the beam heating alone deposits 700 W in the target where the rest of power arises from for circuiting fans and small heaters required to stabilize the target's temperature. The coolant supply is controlled with Joule-Thompson (JT) valves, which can be adjusted either remotely or locally.

To minimize the uncertainty in the target density, the pressure is monitored by pressure transducers at several locations with a typical precision of better than 0.34 MPa, which contributes less than 0.1% to the density uncertainty. The primary temperature sensors are LakeShore Cernox, precision semiconductor sensors with a high radiation resistance. The precision of the temperature measurement is about 0.05 K, which contributes less than 0.1% uncertainty to the density. Other types of

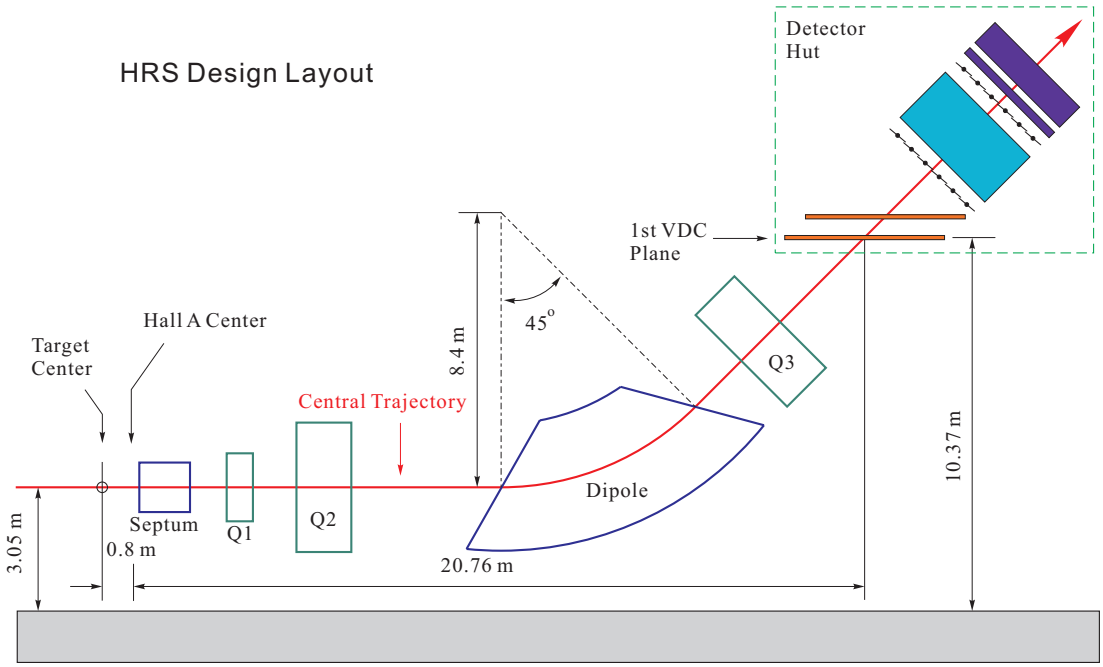

Figure 2-8: Schematic layout of a HRS device, showing the geometrical configuration of the three quadrupole, one dipole magnets and one septum magnet.

temperature sensors are also used to checks and controls, and details can be found in ref [59]. Low-power heaters, up to 60 W, are controlled by the Oxford Temperature Control Model ITC 502 to keep the temperature stable. High-power heaters, up to 1 kW, are used to compensate the power of beam when beam is off. The temperature control is automated by a PID (Proportion, Integral and Derivative) feedback loop.

2.6 Hall A Spectrometers

The core of the Hall A equipment is a pair of identical 4 GeV/c High Resolution Spectrometers (HRS). The spectrometers were designed for detailed investigations of the structure of nuclei, and have high resolution to be able to isolate the different reaction channels in nuclei to achieve a clean comparison with theory can be achieved. To achieve such requirements, a QQD$_n$Q (Quadrupole-Quadrupole-Dipole-Quadrupole) magnet configuration was selected. The basic lay out is shown in Figure 2-8. The 45°'s vertically bending design includes a pair of superconducting cos(2θ) quadrupoles

Configuration	QQD_nQ
Bending Angle	45°
Optical Length	24.2 m
Momentum Range	0.3∼4.0 GeV/c
Momentum Acceptance ($\delta p/p$)	±4.5%
Momentum Resolution	2×10^{-4}
Dispersion at the focus (D)	12.4 m
Radial Linear Magnification (M)	-2.5
D/M	5.0
Angular Range	$6 \sim 12.5°$
Angular Acceptance Horizontal	±25 mrad
Angular Acceptance Vertical	±50 mrad
Solid Angle at $\delta p/p = 0$, $y_{\rm tg} = 0$	4.3 msr
Angular Resolution Horizontal	1.5 mrad
Angular Resolution Vertical	4.0 mrad
Transverse Position Resolution	2.5 mm

Table 2.1: Main characteristics of the Hall A high resolution spectrometers; the resolution values are for the FWHM

followed by a 6.6 m long dipole magnet with focusing entrance and exit polefaces and including additional focusing from a field gradient n in the dipole. Following the dipole is a third superconducting $\cos(2\theta)$ quadrupole. The first quadrupole Q1 is convergent in the dispersive (vertical) plane. Q2 and Q3 are identical and both provide transverse focusing. With this setup, both spectrometers can provide a momentum resolution better than 2×10^{-4} in a 9% acceptance.

Because of the giant volume of HRSs, they can only be positioned with forward angle larger than 12.5°. To fulfill the special needs to reach lab scattering angles of 6 degrees for experiments [66, 67, 68], a pair of pre-bending septum magnets were required. A cold iron superconducting "C" magnet design was selected [55]. With a maximum central field of 4.23 Tesla and effective field length of 0.67 m, the septum magnets bend 4 GeV/c particles at any angle from 6 to 12.5 degrees and match the HRS optics from 12 to 24 degrees. Installation of septum magnets also required the target center to be displace by 0.8 m upstream. It has been verified that the overall new magnetic system is consistent with preservation of spectrometer performance. The main characteristics of the spectrometers are shown in Table 2.1.

2.6.1 Detector Packages

The detector packages of the two spectrometers were designed to perform various functions in the characterization of charged particles passing through the spectrometer. These include: providing a trigger to activate the data-acquisition electronics, collecting tracking information (position and direction), coincidence determination, and identification of the scattered particles.

The configuration of the detectors on the left and right spectrometers for E04-012 experiment is show in Figure 2-9. The detector package of left HRS was used to detect K and π mesons and included:

- a set of two Vertical Drift Chambers (VDCs) to provide tracking information,
- three scintillator planes to provide basic triggers,
- two Aerogel Cherenkov counters to provide particle identification (PID),
- a ring imaging $\tilde{\text{C}}$erenkov detector (RICH) for PID, and
- a pair of lead glass pion rejectors for PID.

The right HRS collected scattered electrons with

- a set of two Vertical Drift Chambers (VDCs) for tracking,
- two scintillator planes for trigger, and
- a CO_2 gas Cherenkov counter for PID.

2.6.2 Vertical Drift Chambers

The Vertical Drift Chamber (VDC) [69, 70] provides a precise measurement of the incident positions and angles of charged particles at the spectrometer focal planes[2]. The tracking information from the VDC measurement is combined with the knowledge

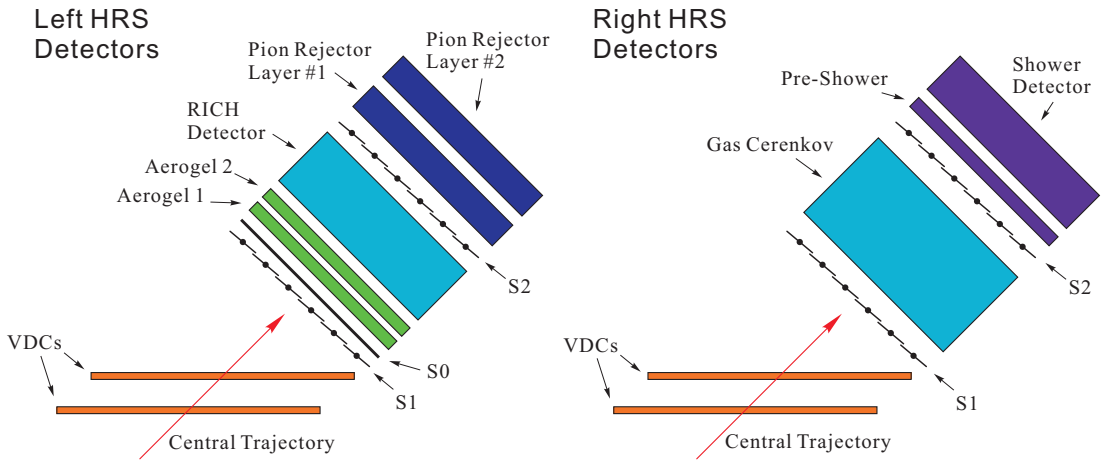

Figure 2-9: Configuration of left and right HRS detectors (side view).

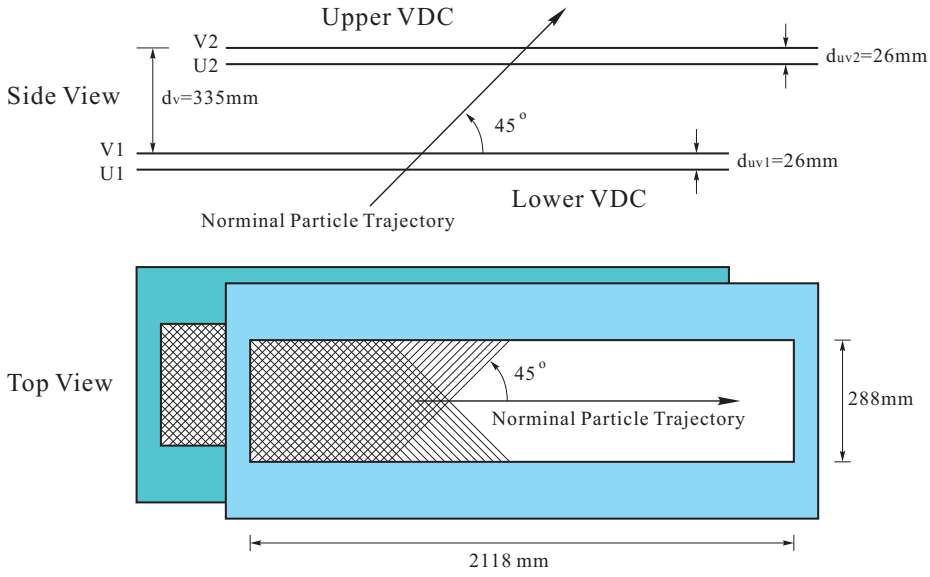

Figure 2-10: Schematic lay-out of a pair of Vertical Drift Chambers for one HRS (not to scale).

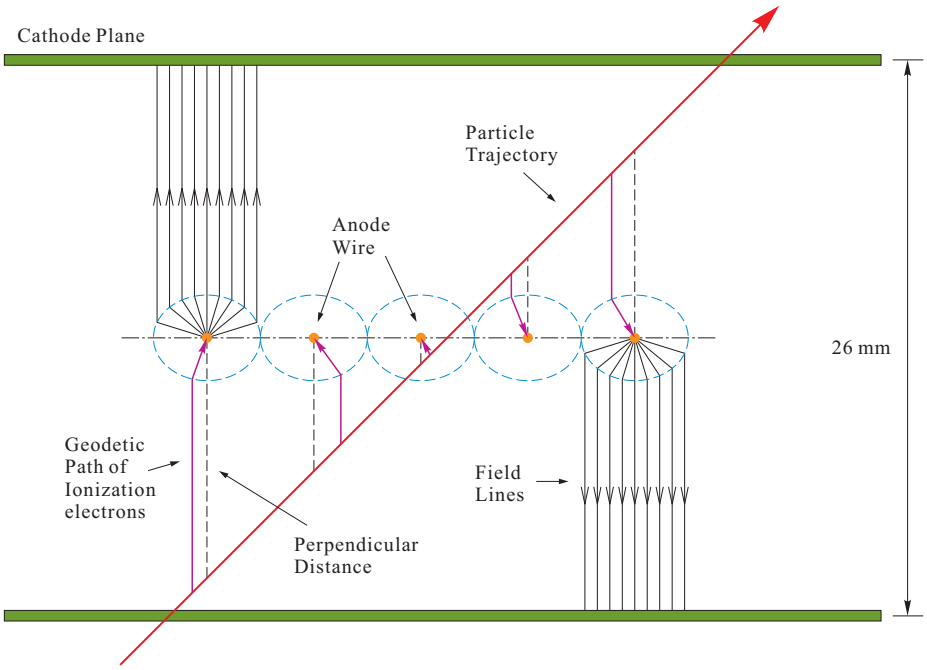

Figure 2-11: Configuration of wire chambers.

of the spectrometer optics to reconstruct the position, angle and momentum of the particles in the target system.

Each spectrometer has a pair of identical VDCs and all of them are laid horizontally. The top VDC is placed 33.5 cm above the bottom VDC and shifted by another 33.5 cm in the dispersive direction to fit the 45° central particle trajectory, see Figure 2-10. Each VDC contains two planes of wires in a standard UV configuration - the wires of each successive plane are oriented at 90° to one another, and lie in the laboratory horizontal plane. There are a 368 sense wires in total in each plane, spaced 4.24 mm apart.

In operation, the VDC chambers have their cathode plane at about -4 kV and the wires at ground. The gas supplied to the VDCs is a 62%/38% argon-ethane (C_2H_6) mixture, with a flow rate of 10 liter/hour [59]. When a charged particle travels through the camber, it ionizes the gas inside the chamber and leaves behind a track of electrons and ions along its trajectory. The ionization electrons accelerate toward

[2]Focal plane is a plane associated with the lower VDC of each spectrometer. Its detailed description and the definition of related coordinate systems can be found in section A.1.

the wires along the path of least time (geodetic path). The Hall A VDCs feature a five cell design, i.e a typical 45° track will fire five wires as shown in Figure 2-11. The fired wires are read out with Time-to-Digital converters (TDCs) operating in common stop mode. In this configuration, a smaller TDC signal corresponds to a larger drift time. With a 50 μm/ns drift velocity and time shift constants the distances of the track to each fired wires are precisely reconstructed. The position and direction of the track is then determined. In the focal plane the position resolution is $\sigma_{x(y)} \sim 100$ μm, and the angular resolution $\sigma_{\theta(\phi)} \sim 0.5$ mrad.

2.6.3 Scintillator Trigger Planes

There are two planes of trigger scintillators S1 and S2 in each spectrometer, separated by a distance of about 2 m. Each plane is composed of six overlapping paddles made of thin plastic scintillator (5 mm BC408) to minimize hadron absorption, see Figure 2-12. Each scintillator paddle has an active area of 29.5×35.5 cm^2 and 37.0×54.0 cm^2 for S1 and S2, and is viewed by two photomultiplier tubes (PMTs) (Burle 8575).

The scintillators are mainly used to generate triggers for the data acquisition system and the time resolution of each plane is about 0.30 ns. The scintillators may also be used for particle identification by measuring the Time-of-flight (TOF) between the S1 and S2 planes. In this experiment only the trigger feature was used.

On the left HRS, an additional S0 scintillator counter was installed. The 10 mm thick S0 counter was viewed by two 3" PMTs XP2312 and provided trigger efficiency information which will be discussed in section 2.7.

2.6.4 Aerogel Cherenkov Counter

The two Aerogel courters (A1 and A2) [71] are threshold Cherenkov detectors based on the Cherenkov effect [72, 73]. The combination of these detectors is used to identify different hadron types: pions, kaons and protons. The Cherenkov effect refers to the effect that when a high energy charged particle travels through transparent materials with a velocity v larger than the phase velocity of light in that material (c/n) a

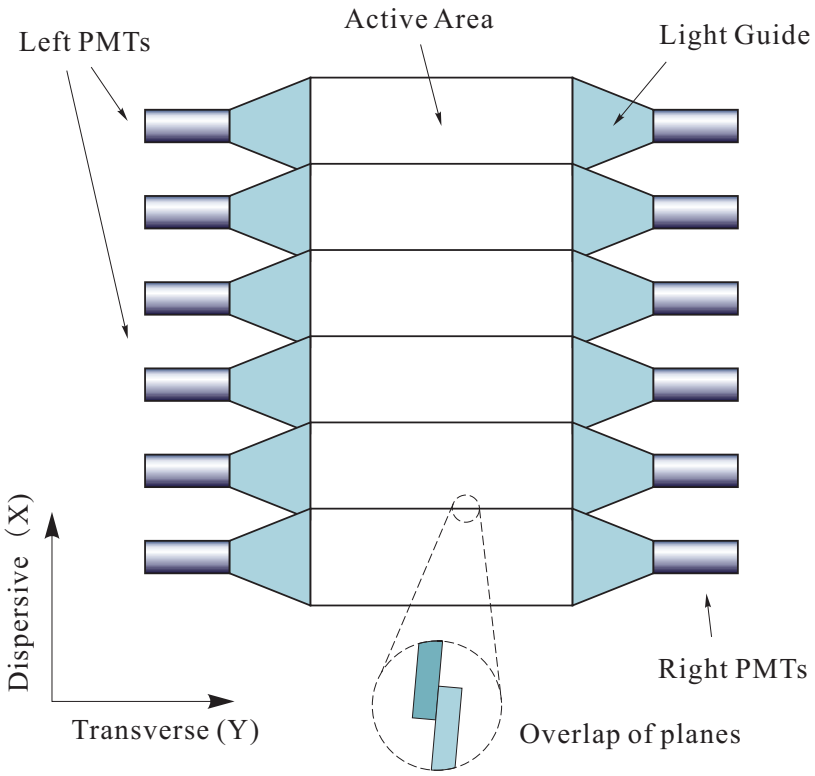

Figure 2-12: Layout of Scintillator Counters.

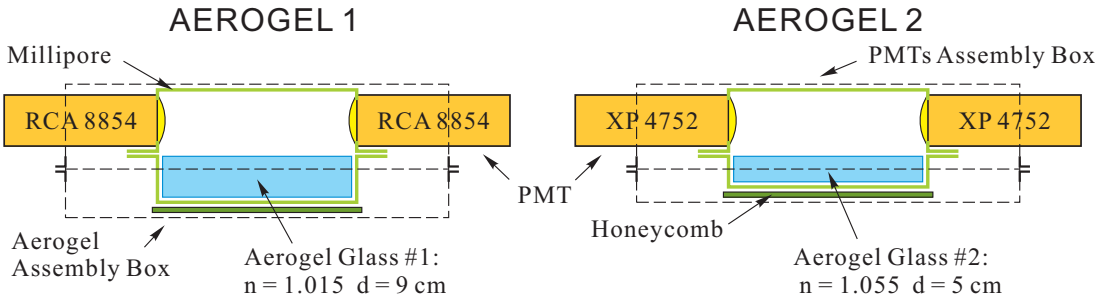

Figure 2-13: Section View of Aerogel Cherenkov Counters.

characteristic electromagnetic radiation is emitted, called the Cherenkov radiation (Cherenkov light). The Cherenkov light has a fixed angle to the particle path:

$$\theta_c = \arccos(1/n\beta), \tag{2.7}$$

and the number of photons has the following production formula,

$$\frac{d^2N}{dxd\lambda} \propto \frac{z^2}{\lambda^2}(1 - \frac{1}{\beta^2 n^2(\lambda)}), \tag{2.8}$$

where the λ is the wavelength of photons and the z is the charge number of the material element. The net effect is that faster particles generate more photons with wavelength typically in the blue region (shorter wavelength favored) of the visible spectrum.

For the two sets of Aerogel detectors, a diffusion technique of light collection evaluated in Refs. [74, 75, 76] was used. A 9 cm thick Aerogel radiator used in A1 has a refraction index of 1.015, giving a threshold of 2.84(0.803) GeV/c for kaons(pions). 24 PMTs (RCA 8854) are used to collect the emitted photons and the average number of photo-electrons for GeV/c electrons is about 3.8. The A2 counter has a 5 cm thick Aerogel glass with index $n = 1.055$, giving a threshold of 2.8(1.5/0.415) GeV/c for protons(kaons/pions). It has 26 PMTs (XP4572) and collects average 14.5 photo-electrons for GeV/c electrons. Therefore during normal operations with HRS-L momentum $p_{\rm L}$ between 0.42 - 2.8 GeV/c, pions will fire both counters, kaons can only fire A2 and protons fire nothing.

2.6.5 RICH Detector

The Hall A ring imaging Cherenkov (RICH) detector was mainly designed for better kaon identification during JLab Experiment E94-107 "Hypernuclei Spectroscopy" [66]. Its design is conceptionally identical to the CERN Alice HMPID detector [77], but adapted to the special needs of experiment E94-107 and the Hall A environment. A description of the Hall A RICH detector is found in reference [78, 79]. The RICH has a proximity focusing geometry (no mirrors involved) which makes the detector compact (total thickness less than 50 cm) and relatively thin (18% X_0). Figure 2-14 shows the working principle of the adopted solution. The Cherenkov effect takes place in the liquid freon when a charged particle crosses it. The liquid radiator, 1.5 cm thick, is housed in a vessel made of NEOCERAM[3] on all sides but the exit window which is made of pure quartz, 0.5 cm thick. The use of a liquid radiator has been imposed by the momentum range (around 2 GeV/c) of the particles to be identified. The Cherenkov photons, emitted along a conical surface, are refracted by the freon-quartz-methane interfaces and strike a pad plane after traveling a proximity gap of 10 cm filled with methane.

The pad plane is covered by a thin substrate of CsI which acts as photon converter. The emitted photo-electron is accelerated by an electrostatic field (2100 V/2 mm) between the pad plane and an anode wire plane in front of the pads, forming a multi-wire proportional chamber (MWPC). While the anode wires collect the electron avalanche, the counterpart ions are collected by clusters of pads, each of which is connected to the input channel of a multiplexed sample-and-hold electronics, housed on the back of the pad plane. At the end of this process, the clusters of pads hit by the photons should be scattered around a ring (ellipse) while one cluster coming from the charged particle track should be located in the central region of the ring. A drift electrode operated at 250 V and located close to the quartz window, prevents electrons produced by ionization of the counting gas by charged particles in the proximity gap from reaching the MWPC. The MWPC of the RICH detector has to be operated with

[3]NEOCERAM is a glass-ceramic material with mechanical and thermal properties almost identical to quartz.

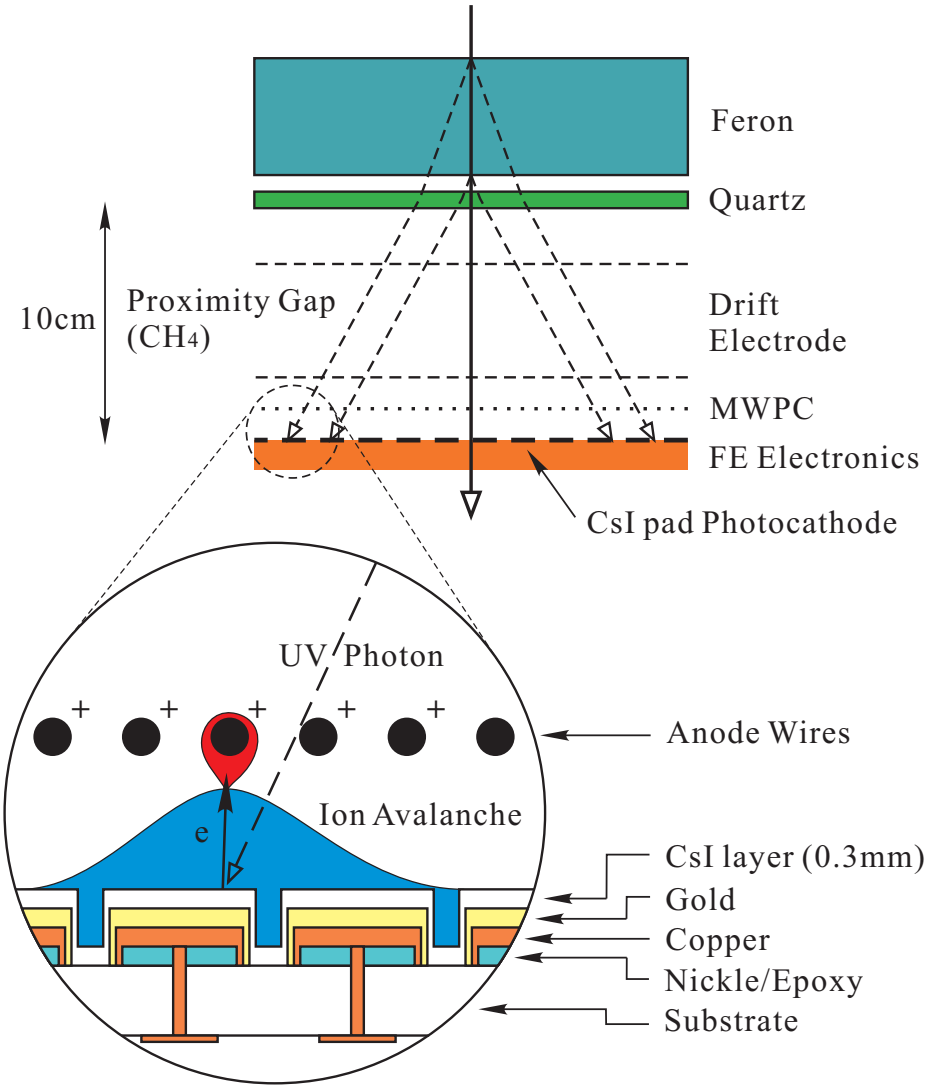

Figure 2-14: Working principle of the freon CsI proximity focusing RICH.

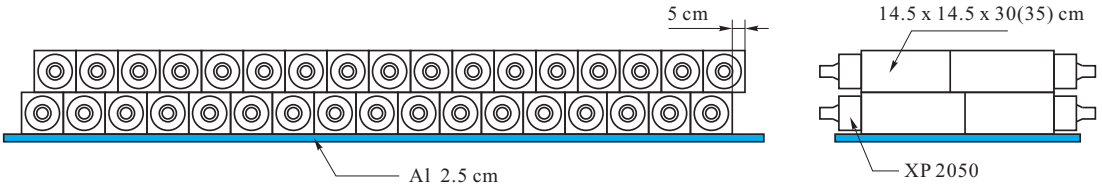

Figure 2-15: Configuration of Lead Glass Pion Rejectors.

pure methane to achieve the designed performances.

The RICH detector has Cherenkov angle resolution $\sigma \sim 5$ mrad which gives a 4σ separation of pion and kaon peak at 2 GeV/c momentum.

2.6.6 Pion Rejector

During the experiment the polarity of left HRS was changed to negative for the Θ^{++} setting. In this period, the scattered electrons became a large background in left arm since Aerogel and RICH detectors are unable to distingwish them from pions. Therefore a pair of lead glass counters, so-called "pion rejectors", were used for particle identification. For GeV/c charged particles passing through the detector, only electrons are able to develop electromagnetic showers, whereas hadronic showers do not develop much due to the longer hadronic mean free path. Therefore, we are able to identify the incident particles according to the energy deposition in the counter: low ADC signal for hadrons and high ADC signal for electrons.

The two layers of pion rejectors have the same geometry. Each layer consists 17 short blocks and 17 long blocks of lead glass, forming a 2(transverse)×17(dispersive) array, as shown in Figure 2-15. All lead glass blocks are oriented transversely with respect to the direction of the incoming particles. Short and long lead glass blocks are arranged interchangeably in the dispersive direction for each row. The gap between blocks of the first layer is covered by a lead glass block of the second layer, and vice versa.

2.6.7 Gas Cherenkov Counter

In the right HRS, only electrons were selected all the time. Therefore a CO_2 threshold gas Cherenkov detector is used sololy for this PID. This detector was filled with CO_2 at atmospheric pressure. The refraction index is 1.00041 which give a threshold momentum $\sim$ 17 MeV/c for electrons and 4.8 GeV/c for pions. Therefore within a momentum range of 0.02 $\sim$ 4.8 GeV/c, only electrons emit Cherenkov light and generate ADC signal.

The Gas Cherenkov detector is made of steel with thin entry and exit window made of tedlar [80]. Then spherical mirrors positioned in a 2(horizontal)$\times$5(vertical) array are used to collect Cherenkov light. These mirrors are specially built to be light weight resulting in a very small total thickness (0.23 g/cm^2) [81] traversed by the particles. The position and orientation of these mirrors were designed in a way such that the Cherenkov light emitted by the scattered electrons can be efficiently collected. Each mirror is coupled to a PMT. The mirrors have radius of curvature of 90 cm and the PMTs are placed at a distance of $90/2 = 45$ cm from the mirrors, where the parallel rays of incident light on the mirrors are approximatively focused. The light is converted to electronic signals by PMTs and fed to ADCs. The summed signal of all ten ADCs gives information about the total light emitted by the particle.

Though pions should not produce any Cherenkov light directly, they can interact with the matter they pass through and create δ-electrons [82]. These δ-electrons Will produce Cherenkov light and trigger the ADCs. However, these pion events can be removed with the selection of coincidence events between two HRS and the details will be described in the following chapter.

2.7 Trigger electronics

In this experiment, six different types of triggers were generated and used in the data acquisition. Four of them are single arm triggers, T1 - T4, and the rest two, T5 and T7, are coincidence triggers. The trigger system was basically built from commercial CAMAC and NIM discriminators, delay units, logic units and memory lookup units

(MLU).

2.7.1 Signal Arm Triggers

T1 and T2 triggers were generated from right HRS while T3 and T4 were from the left HRS. As illustrated in Figure 2-16, the primary triggers, T1 and T3, are formed using combination of signals from S1 and S2 scintillators on each arm. They require

- one scintillator bar is called "fired" when both the left and right PMTs have signals,
- both S1 and S2 have at least one fired scintillator bars and they are close enough: the difference between number of bars is 0 or 1.

T3 and T4 triggers were used to measure the inefficiency of T1 and T3 triggers, therefore they were formed in the following way with such purpose

- both S1 and S2 have at least one fired bars and none of them are close,
- *OR* only one of S1 or S2 have fired bars and at the same time gas Cherenkov (S0 in left HRS) get fired.

The trigger inefficiency was measured from high yield elastic runs (in order to minimize the dilution from cosmic events and have all outgoing particles to be electrons which can fire gas Cherenkov counter). The value is given by:

$$\text{Inefficiency}_{R(L)} = \frac{T_{2(4)}}{T_{1(3)} + T_{2(4)}}. \tag{2.9}$$

The trigger efficiencies for both arms were determined to be less than 1% and negligible. During normal production runs, the trigger efficiency was monitored by the ratio of T2(T4) rate to T1(T2) rate. A less than 5% ratio indicates an efficient trigger.

2.7.2 Coincidence Triggers

The diagram of coincidence triggers is shown in Figure 2-17. T5 coincidence trigger is simply an "AND" of T1 and T3 triggers. To reduce the pion background counts in

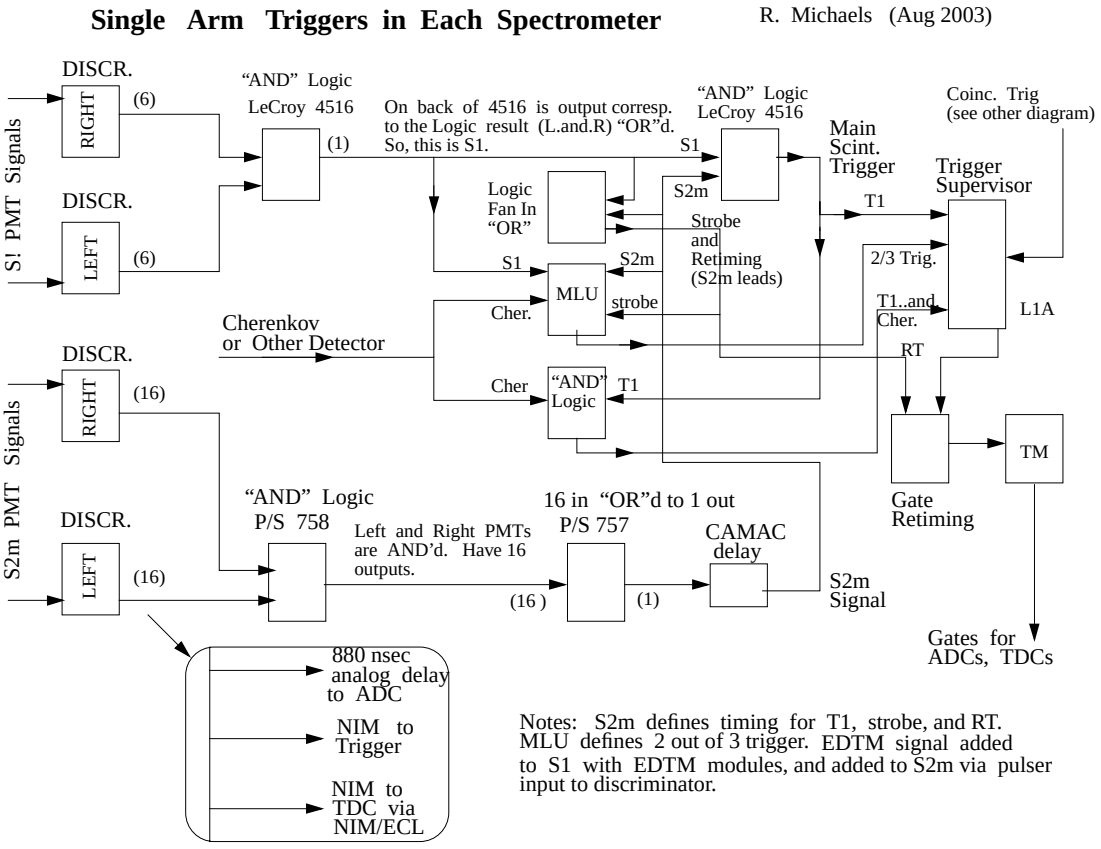

Figure 2-16: Diagram for single arm triggers.

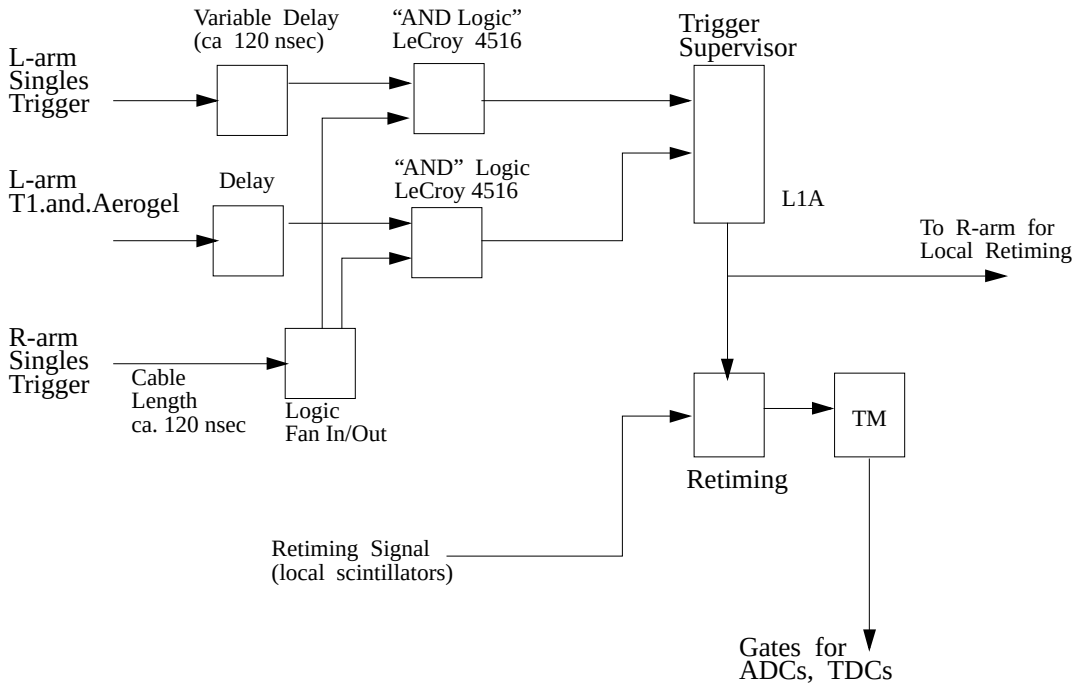

Figure 2-17: Diagram for coincidence triggers.

coincidence events, the signals of two Aerogel and gas Cherenkov detectors were used to form a PID coincidence trigger: T7. A T7 trigger is generated when a T5 signal is coincident with a signal from Aerogel 2 and gas Cherenkov, with Aerogel 1 quiet.

2.7.3 Trigger Selection

A summary of triggers used in E04-012 is found in Table 2.2. After generated, all types of triggers have their copies sent to a scaler unit for counting and a trigger supervisor (TS) unit to trigger data acquisition. The TS unit has a pre-scale function. If the pre-scale factor for a specific trigger type is N, then only 1 out of N triggers of that type is recorded in the data stream. This function is very useful to decrease the computer dead time caused by frequent data record while keeping all events with useful physics information. Therefore, during the production data taking, all single

Trigger	Logic Definition
T1	$S1^R_N$ AND $S2^R_{N\ or\ N\pm1}$
T2	(($S1^R_N$ NOT $S2^R_{N\ or\ N\pm1}$)OR($S2^R_N$ NOT $S1^R_{N\ or\ N\pm1}$))AND Cherenkov
T3	$S1^L_N$ AND($S2^L_{N\ or\ N\pm1}$)
T4	(($S1^L_N$ NOT $S2^L_{N\ or\ N\pm1}$)OR($S2^L_N$ NOT $S1^L_{N\ or\ N\pm1}$))AND S0
T5	T1 AND T3
T7	T1 AND T3 NOT A1 AND A2 AND Cherenkov

Table 2.2: Summary table for trigger logics

arm triggers were heavily pre-scaled and coincidence triggers T5 and T7 were less or not pre-scaled.

2.8 Hall A Data Acquisition System

The Hall A data acquisition (DAQ) system uses CODA (CEBAF On-line Data Acquisition) [83] developed by the Jefferson Lab Data Acquisition Group.

CODA is composed of a set of software and hardware packages from which a data acquisition system can be constructed, including front-end Fastbus and VME digitization devices (ADCs, TDCs, scalers), the VME Interface to Fastbus, single-board VME computers running VxWorks operating system, Ethernet networks, Unix or Linux workstations, and a mass storage tape silo (MSS) for long-term data storage. The custom software components of CODA are:

- a readout controller (ROC) which runs on the front-end crates to facilitate the communication between CODA and detectors;
- an event builder (EB) which collects all the ROC data fragments, and incorporates all the necessary CODA header information needed to describe and label and event and the data fragments to build the event;
- an event recorder (ER) to write the data built by EB to disk;
- an event transfer (ET) system which allows distributed access to the data stream from user processes and inserts additional data into the data stream every a few

seconds from the control system, scalers or some text information;

- a graphical user interface (Run Control) to set experimental configuration, control runs, and monitor CODA components.

A recorded CODA file consists the following major components:

- Header file including a time stamp and other run information like run number, pre-scale factors and event number.
- CODA events from the detectors.
- CODA scaler events: the DAQ reads the scaler values every 1 - 4 seconds and feeds them into the main data stream. Since counted by stand-alone units, the scaler values are not effected by the DAQ dead time therefore they can be used to correct DAQ dead time.
- EPICS [84] data from the slow control software used at JLAB, eg. the spectrometer magnet settings and angles, target temperature and pressure.

The Total volume of data accumulated during this experiment was about 1.0 TBytes.

2.9 Kinematics

The kinematics of the experiments are listed in Table 2.3. Since K and π were detected in left arm at the same time, each kinematics included both $H(e,e'\pi)X$ and $H(e,e'K)X$ channels. And they were selectively used for the following purposes:

- Kin 1 and 3 were used for missing mass calibration by collecting data from neutron, $\Lambda^0(1116)$ and $\Sigma^0(1193)$ photo-productions: $H(e,e'\pi^+)n$, $H(e,e'K^+)\Lambda^0(1116)$ and $H(e,e'K^+)\Sigma^0(1193)$.
- Kin 4 measured the production of $\Lambda^0(1520)$ in $H(e,e'K^+)\Lambda^0(1520)$ reactions. The integral cross-section of $\Lambda^0(1520)$ would be used as comparison for pentaquark states.

- Kin 5 - 13 were settings searching for Σ_5^0 and N_5^0 in $H(e,e'K^+)\Sigma_5^0$ and $H(e,e'\pi^+)N_5^0$ reactions. Each setting covers around 130 MeV/c^2 effective missing mass range. The overall range for Σ_5^0 was 1.535 - 1.820 GeV/c^2 and 1.595 - 1.895 GeV/c^2 for N_5^0.

- Kin 14 was done before the change of the left spectrometer to negative polarity for the Θ^{++} search. During this setting, only data from left arm were taken and its central momentum was set at 0.55 GeV/c. In this case, only π^+ can radiate in the RICH detector and has a very similar speed as K^+ at 2 GeV/c. Therefore the RICH efficiency for 2 GeV/c kaon detection was easily calculated using the π^+ data.

- Kin 17 was used for Θ^{++} search in $H(e,e'K^-)\Theta^{++}$ reaction. It has similar momentum settings to Kin 4 of $\Lambda^0(1520)$ and missing mass coverage is 1.470 - 1.600 GeV/c^2. The left spectrometer was set at negative polarity and the pair of Pion Rejectors was used for electron background rejection.

Kin	E_{beam} (GeV)	θ_R	P_R (GeV/c)	Right Polarity	θ_L	P_L (GeV/c)	Left Polarity	Q^2 (GeV/c)^2	Missing Mass M_X (GeV/c^2)		Comments
									$H(e,e'\pi)X$	$H(e,e'K)X$	
1	5.01	-6°	2.50	-	6°	2.49	+	0.137	0.765-1.065	0.730-1.010	Neutron
3	5.01	-6°	2.50	-	6°	2.22	+	0.137	1.045-1.270	0.995-1.215	$\Lambda^0(1116)/\Sigma^0(1193)$
4	5.01	-6°	2.00	-	6°	2.10	+	0.110	1.505-1.645	1.450-1.580	$\Lambda^0(1520)$
5	5.01	-6°	2.00	-	6°	1.93	+	0.110	1.610-1.730	1.550-1.660	$\Sigma_5^0/\mathrm{N}_5^0$
6	5.01	-6°	1.93	-	6°	1.93	+	0.106	1.650-1.770	1.585-1.695	$\Sigma_5^0/\mathrm{N}_5^0$
7	5.01	-6°	1.70	-	6°	1.90	+	0.093	1.795-1.895	1.725-1.820	$\Sigma_5^0/\mathrm{N}_5^0$
10	5.01	-6°	1.83	-	6°	1.93	+	0.100	1.705-1.820	1.640-1.745	$\Sigma_5^0/\mathrm{N}_5^0$
11	5.01	-6°	1.98	-	6°	1.93	+	0.109	1.620-1.745	1.560-1.670	$\Sigma_5^0/\mathrm{N}_5^0$
12	5.01	-6°	2.02	-	6°	1.93	+	0.111	1.595-1.725	1.535-1.650	$\Sigma_5^0/\mathrm{N}_5^0$
13	5.01	-6°	1.85	-	6°	1.89	+	0.102	1.715-1.830	1.650-1.750	$\Sigma_5^0/\mathrm{N}_5^0$
14	5.01	-6°	N/A	-	6°	0.55	+	N/A	N/A	N/A	RICH Efficiency
17	5.01	-6°	2.00	-	6°	2.06	-	0.110	1.530-1.665	1.470-1.600	Θ_5^{++}

Table 2.3: Kinematics of Pentaquark Search

Chapter 3

Data Processing

3.1 Analysis Overview

The Hall A C++ Analyzer [85] was used to replay the raw data and analyze the physics for this experiment. The Analyzer is developed by Hall A software group based on ROOT [86], a powerful object-oriented (OO) framework that has been developed at CERN by and for the nuclear and particle physics community.

The flow-chart of the E04-012 analysis procedure is illustrated in Figure 3-1. Raw data from detector readouts were first transformed into physics variables or corrected by Analyzer replay using calibrated database. Then for each kinematics settings, missing mass spectra were turned into differential cross sections by adding luminosities, acceptance and efficiency factors as well as accidental background subtraction. After all individual spectra were obtained, they were finally combined together into a larger range cross section spectrum for further resonance search analysis.

3.2 Detector Calibration and Alignment

3.2.1 One-Track-Only Cut

Before proceeding further, the One-Track-Only cut must be defined. As described in section 2.6.2, the tracks of one event are reconstructed from VDC clusters. The

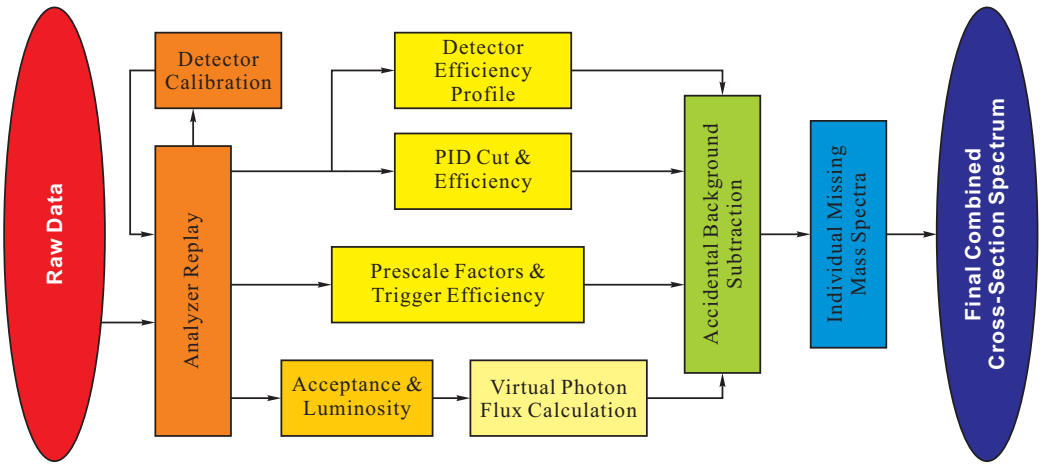

Figure 3-1: Data processing procedure of this experiment.

drifting time ranges from 0 to 300 ns. In the C++ analyzer, a software cut of 400 ns is applied after the first wire fires to ensure the completeness of the track. If only one track is observed in an event, the track reconstruction will be accurate. However, if multiple tracks in an event are seen in the analysis, the first track may not be accurately reconstructed due to the interference of a close second track.

On the other hand, the particle identification is also complicated for multiple tracks since it might be difficult to distinguish which track triggered the detector if they are close enough in both time and position.

Therefore, in the following analysis if it is not specially mentioned, the One-Track-Only cut is applied all the time. It is assumed that the fraction of good events in the multiple track events is the same as that in the one track events so that the number of good events dropped in the multiple track events is recovered by applying the one track ratio which is defined as

$$\eta(ONE) = \frac{N(n_{track} = 1)}{N(n_{track} > 0)}. \tag{3.1}$$

3.2.2 Detector Calibration

The scintillator trigger planes, S1 and S2, were confirmed to be working properly during the commissioning of E04-012. Since none of them would be used in particle

identification (PID), no further calibration was required.

The VDC database was calibrated during the Hall A Hyper-Nuclear experiment which is described in Chapter A.2.2.

Single Photon Peak Alignment of PMTs

Except for the RICH detector, all of the PID detectors: Aerogel 1/2, Gas Cherenkov and Pion Rejector 1/2 used Photo-Multiplier Tubes (PMTs) as their output. When a certain high voltage applied, the PMT output is proportional to the number of photo-electrons(P.E.) released from the photo-cathode. According to the principle of photo emission, one electron at most will be released by one photon. The probability that such reaction occurs is called the quantum efficiency η_Q of the photo-cathode [87]. With same type of photo-tube used, the quantum efficiencies are generally the same [88]. Therefore all the single photon peaks from PMTs were aligned to one position and the total number of P.E. were read by adding all PMTs' output together. This detector sum was then used for particle identification. Figure 3-2 shows the alignment for Aerogel 1 PMTs.

Detector Shape Regularity

Even after the single photon peak calibrations, the total (summed) amplitudes of detectors were still not aligned very well in the out-of-plane direction. The left plot of Figure 3-3 shows such problem in Aerogel 1 detector and the horizontal axes x is the out-of-plane position in detector system. The reasons could be the difference of quantum efficiencies of individual PMTs or the properties of detector blocks. Since the PID cuts are based on the total amplitude, such irregularity was removed to get a uniform cut efficiency.

To do so, the following procedure is carried out:

- For each kinematics setting, there was always one major type of particle dominating the singles events. When left HRS is set to positive polarity, π^+ was overwhelming. When set to negative polarity, both arms mostly collect electrons. Therefore, pion events were selected for Aerogel calibration and electron

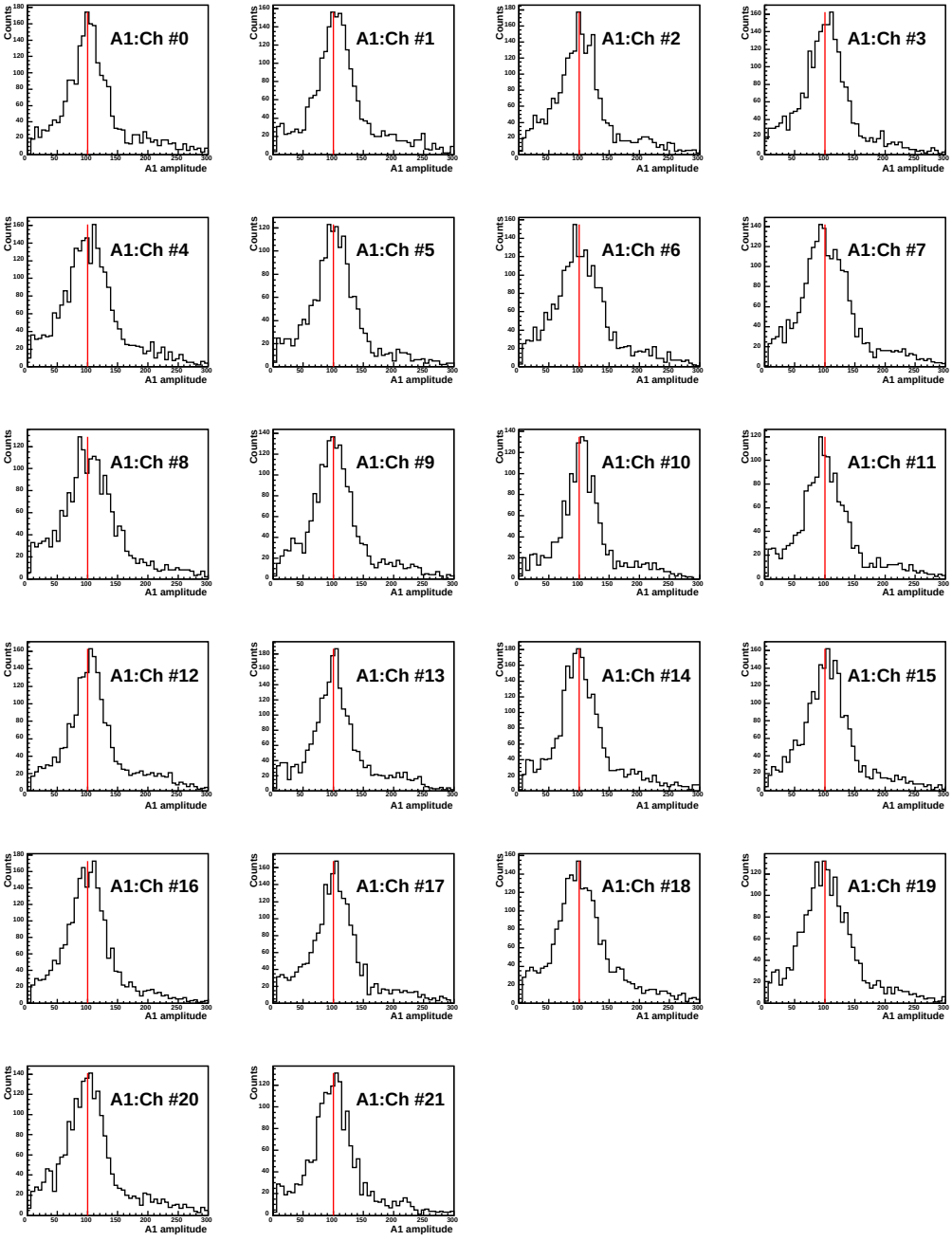

Figure 3-2: Alignment of single photon peak from Aerogel 1 detector.

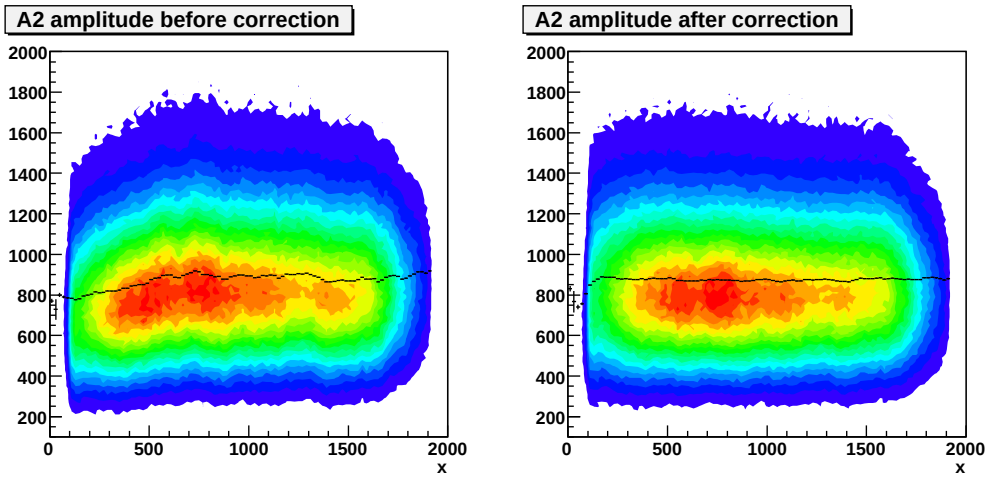

Figure 3-3: Detector amplitude spectra and profiles from A2 detectors. The black curves are profiles.

events were selected for the Gas Cherenkov Detector and Pion Rejectors. Even without very good PID, the samples were still very clean.

- Next, the average amplitude for different x was calculated and formed as a function of position, called a profile.

- Finally, correction factors for all positions were calculated by comparing these profiles values to the averaged profile value in the middle of the detector.Dear

After applying this correction to all of the detectors, the profiles from kaon events were checked, and the data clearly showed good uniformity in all detectors. An example from Aerogel 2 detector is shown in Figure 3-4

3.3 Momentum Acceptance

For both spectrometers only the data within the flat regions of momentum acceptance were used, as shown in Figure 3-5:

$$-0.034 \; < \; \delta_L \; < \; 0.032 \tag{3.2}$$

$$-0.033 \; < \; \delta_R \; < \; 0.034. \tag{3.3}$$

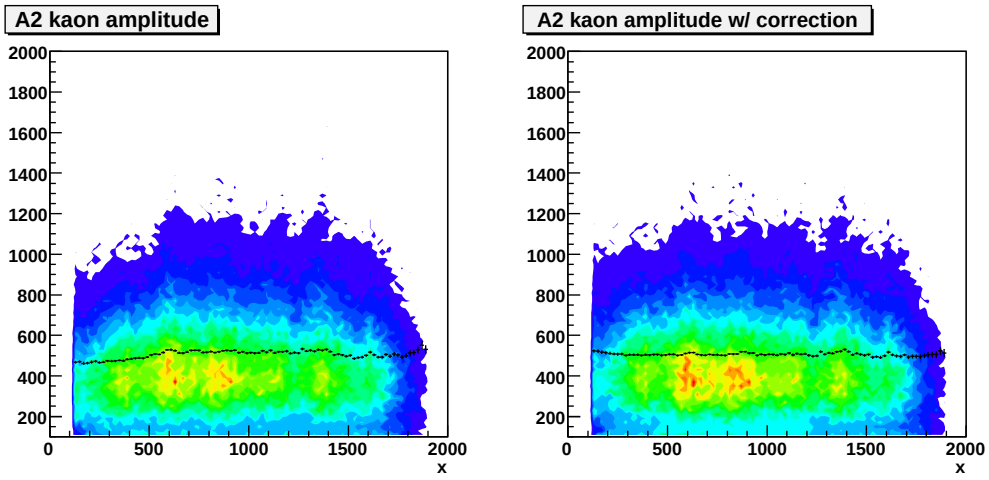

Figure 3-4: Kaon profiles before and after corrections from A2 detectors.

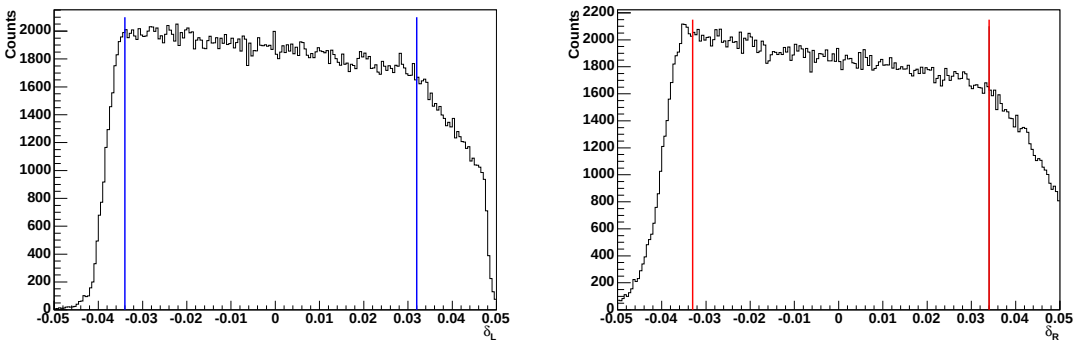

Figure 3-5: Momentum acceptance cuts for the analysis.

3.4 Coincidence System

Before going into more details about detectors, the coincidence system of E04-012 will be described. Two different coincidences were used in the experiment and they are corresponding to time and space.

3.4.1 Time-of-Flight Coincidence

The Time-of-Flight (TOF) is defined as the amount of time elapsed from the creation of a particle to its detection by a spectrometer. The coincidence time (CT) is defined as the time difference between when two particles are created in the reaction. The reconstruction needs the knowledge of both particle's types. In this analysis, the CT is calculated by assuming a pion in left arm and an electron in right arm:

$$CT = T_R(e) - T_L(\pi) = \Delta T_{raw} - \frac{L_R}{v(e)} + \frac{L_L}{v(\pi)}, \tag{3.4}$$

where the ΔT_{raw} is the raw time difference of triggers from both spectrometers, the $L_{L/R}$ is the distance from target to focal planes of each arm as they are reconstructed from the focal plane variables using an optics matrix. The path length is 27.25±0.16 m for both arms.

The upper plot in Figure 3-6 shows the electron-pion coincidence time spectrum. In this case, the coincidence time is calculated with correct particle types so the pion coincidence peak stands out at $CT = 0$. The time resolution of the TOF is measured to be around 600 ns FWHM. The background of the spectrum shows a very regular oscillation which corresponds to the 2 ns period of beam structure.

The lower plots shows the spectrum of electron-kaon coincidence. With the incorrect mass, the kaon peak is shifted by around 2 ns from zero where pion peak is located. Compared to 600 ns resolution, such a shift provides a very clean separation between $e\pi$ and eK coincidence events and the coincidence events are selected by a cut of ±1 ns from the center of CT peaks.

The accidental background is uniformly distributed in the time spectrum and

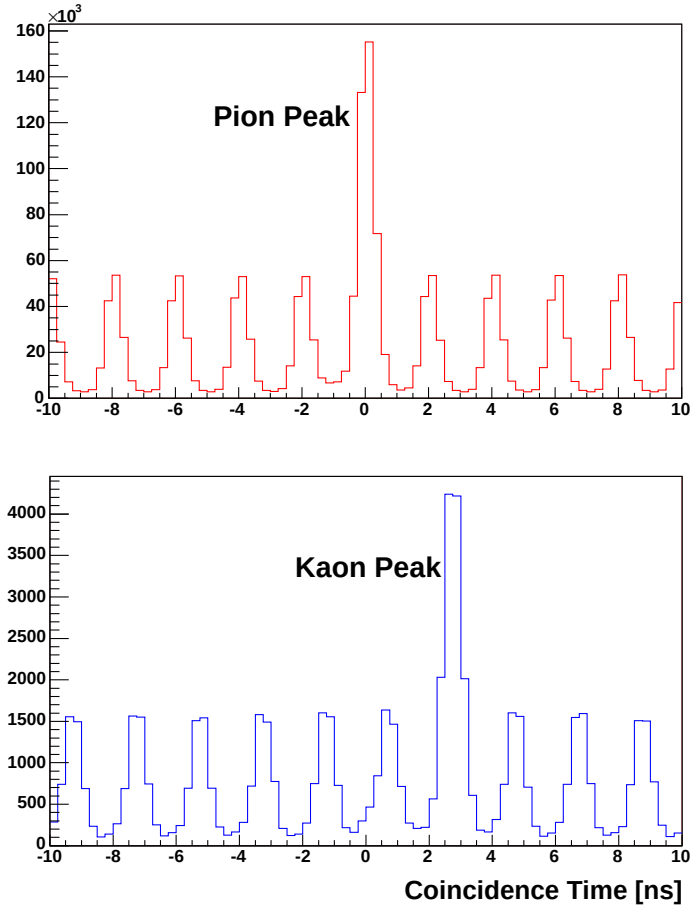

Figure 3-6: Coincidence time spectra of $e\pi$ and eK events.

therefore the actual number of coincidence events can be extracted by subtracting the averaged background:

$$N_{sig} = N_{coin} - \frac{W_{coin}}{W_{acc}} N_{acc}, \tag{3.5}$$

where N_{coin} and N_{acc} are numbers of events in coincidence and accidental windows: W_{coin} and W_{acc}. The former one is 2 ns and the latter is 40-50 ns[1].

Based on the time resolution and the pion rejection efficiency, the final contamination of pion after background subtraction in kaon events is less than 0.01% and the loss of good events for that 2 ns cuts is less than 0.1%.

3.4.2 Reaction Vertex Coincidence

The reaction vertex Z is defined along the beam position. Its reconstruction has a 2.5 cm FWHM resolution for the ideal un-rastered beam condition. With raster turned on (to prevent target from being locally overheated, see Section 2.4.3), the resolution becomes a little bit worse.

For coincidence events, the spatial correlation of two spectrometers is plotted in Figure 3-7 as a two dimensional histogram of Z_L and Z_R which are the vertices reconstructed by the two spectrometers. The resolution of the $Z_L - Z_R$ coincidence peak is determined to be $\sigma_{zCorr} \approx 2.5\ cm$ throughout the effective length of the liquid hydrogen target (15 cm). And by applying the $|Z_L - Z_R| < 5\ cm$ cut, the accidental background is reduced by about a factor of two, as shown in Figure 3-8.

3.5 Particle Identification and Efficiency

With all detectors calibrated, proper cuts need to be selected for particle identification. As described in the instrumentation section (Section 2.6), the responses of all PID detectors to different particles are summarized in Table 3.1.

Therefore the following cut combinations were used to identify different particles:

[1] In the middle of the experiment, the hardware coincidence window was reduced to lower the accidental background.

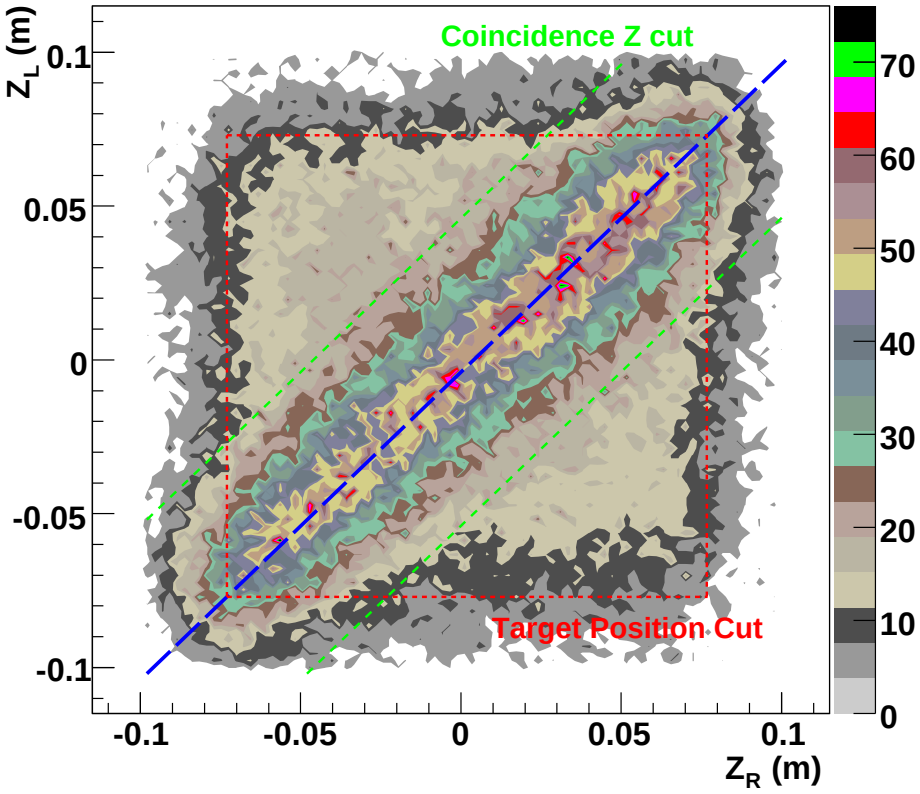

Figure 3-7: Reaction vertex coincidence of two spectrometers.

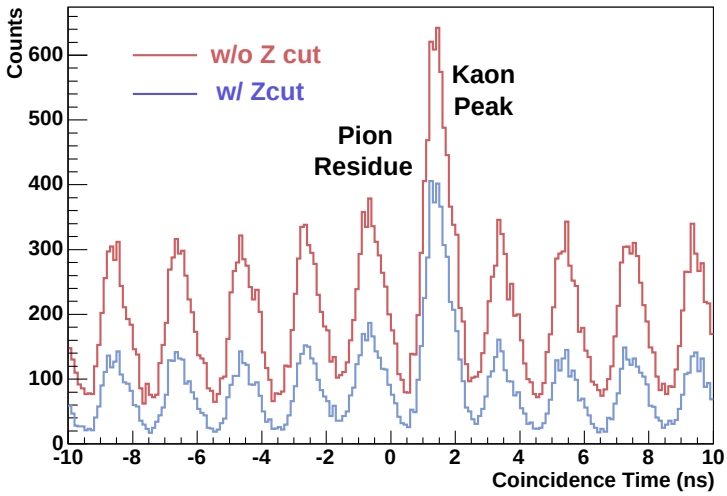

Figure 3-8: Accidental background suppressed by applying vertex coincidence cut.

Detector\Particle	electron	pion	kaon	proton	single photon amplitude
Aerogel 1 (n=1.015) (A1)	large	middle	-	-	100
Aerogel 2 (n=1.055) (A2)	large	large	small	-	60
RICH (n=1.29)	large	large	middle	small	-
Pion Rejector (PR)	large	small	small	small	200
Gas Cherenkov (GC)	large	-	-	-	100

Table 3.1: Response signals of detectors to different particles (p$\sim$2 GeV/c)

$$
\begin{aligned}
e^- \text{ (R)} &: GC, \\
\pi^+ \text{ (L)} &: A1\&\overline{A2}, \\
\mathrm{K}^+ \text{ (L)} &: A1\&\overline{A2}\&RICH(\theta = \theta_K), \\
\pi^- \text{ (L)} &: A1\&\overline{A2}\&PR(\text{small}), \text{ and} \\
\mathrm{K}^- \text{ (L)} &: A1\&\overline{A2}\&RICH(\theta = \theta_K)\&PR(\text{small}).
\end{aligned}
$$

The RICH cut is not used in $\pi^{\pm}$ identification because the kaon contamination is really small and negligible when the pion production dominates.

3.5.1 Aerogel Detectors

Output Shape

The spectrum of Aerogel detectors output can be treated as a Poisson distribution convoluted with Gaussian distributions [88]. The Poisson distribution shows the probability of n photo-electrons collected by the PMTs and the Gaussian shapes stand for the response of PMTs to different number of photo-electrons. Analytically, the spectrum shape can be expressed as following.

$$
\begin{aligned}
\text{Poisson}(n, \mu) &= \frac{e^{-\mu}\mu^n}{n!} && (3.6) \\
\text{Gaus}(x, n, \sigma) &= \frac{1}{\sqrt{2\pi}\sqrt{n}\sigma} e^{-\frac{(x-nA_0)^2}{2n\sigma^2}} && (3.7) \\
A(x) &= C \cdot \sum_n \text{Poisson}(n, \mu) \cdot \text{Gaus}(x, n, \sigma). && (3.8)
\end{aligned}
$$

where C, μ and σ are three free parameters: C is the amplitude factor, μ is the average number of photo-electrons and σ is the width of single photo-electron response. A_0 is

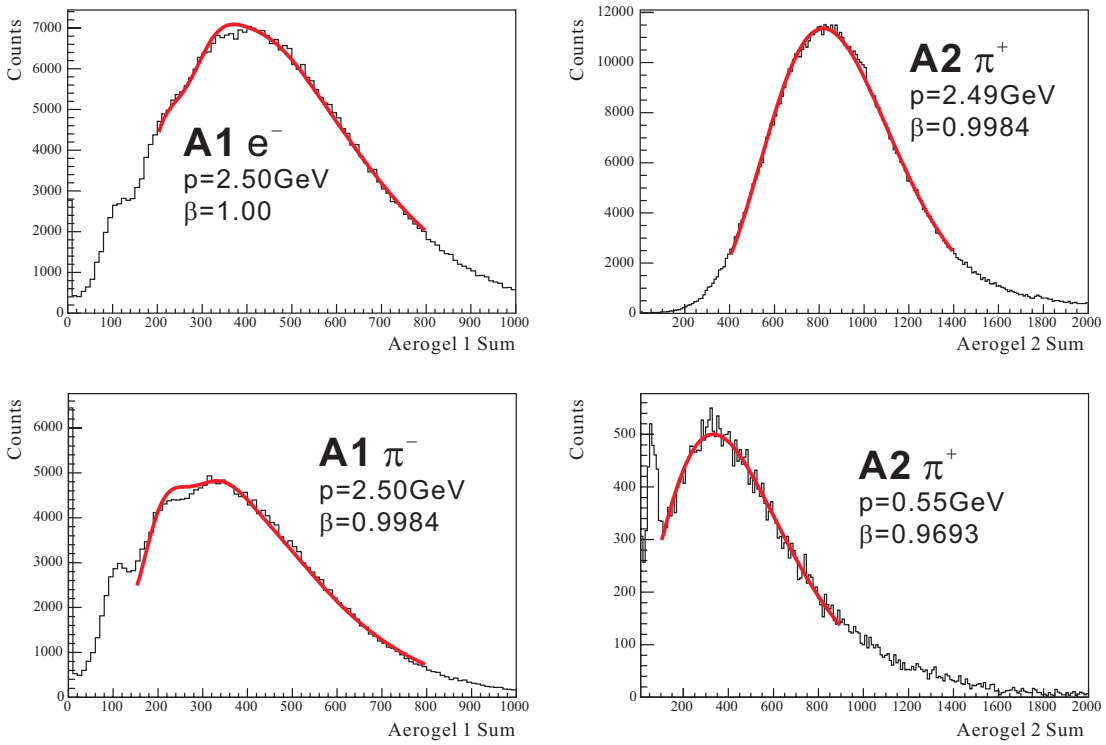

Figure 3-9: ADC sum spectra of Aerogel Detectors from particles with different velocities fitted by theoretical function.

the average amplitude of single photo-electron response and is 100 for Aerogel 1 and 60 for Aerogel 2. The response width changes according to the number of collected photo-electron, and obeys basic statistics:

$$\sigma_n = C_\sigma \sqrt{n \cdot N} = \sqrt{n} \cdot C_\sigma \sqrt{N} = \sqrt{n} \cdot \sigma, \tag{3.9}$$

where N is the total number of electrons collected by the PMT anode after amplification from single photo-electron emission.

The function in equation (3.8) was used to fit the data from Aerogels. As seen in figure 3-9, the theoretical function agrees very well with the Aerogel 2 data. However, the function does not fit Aerogel 1 data. The electron data looks fine but the pion data has a big discrepancy with Poisson distribution. This was discovered, after the experiment, to be an aging problem of the Aerogel 1 material. Fortunately, further analysis has confirmed that this problem does not have much effect on the veto

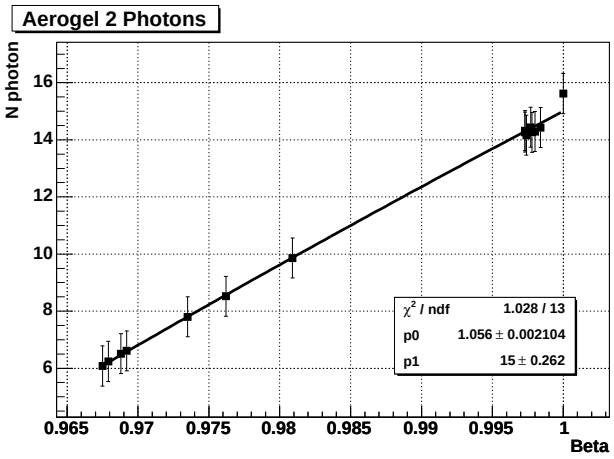

Figure 3-10: Number of photo-electrons as a function of velocity β.

efficiency of A1 to kaons and PID efficiency for pions.

Number of Photo-Electrons

According to the formula (2.8),

$$\frac{d^2N}{dxd\lambda} \propto \frac{z^2}{\lambda^2}(1 - \frac{1}{\beta^2 n^2(\lambda)}),$$

the average number of photo-electrons (N.P.E.) is a function of incident particle's velocity. Therefore, the maximum N.P.E at $\beta = 1$ was extracted by fitting the function using data from different particles and momenta.

Figure 3-10 shows such fit of Aerogel 2. The data points are from e^-, $\pi^\pm$ and $K^\pm$. The formula describes the data very well and not only was the maximum N.P.E. obtained but also the index of Aerogel 2, which is in very good agreement with it's actuall value[2]:

$$N.P.E._{A2}(\beta = 1) = 15.00 \pm 0.26 \quad (3.10)$$

$$\sigma = 42.0 \pm 0.1 \quad (3.11)$$

$$n_{A2} = 1.056 \pm 0.002. \quad (3.12)$$

[2]The index of Aerogel 2 was measured by Lingyan Zhu using optics method [88], and she got $n_{A2} = 1.053 \pm 0.002 \pm 0.003 \pm 0.000$.

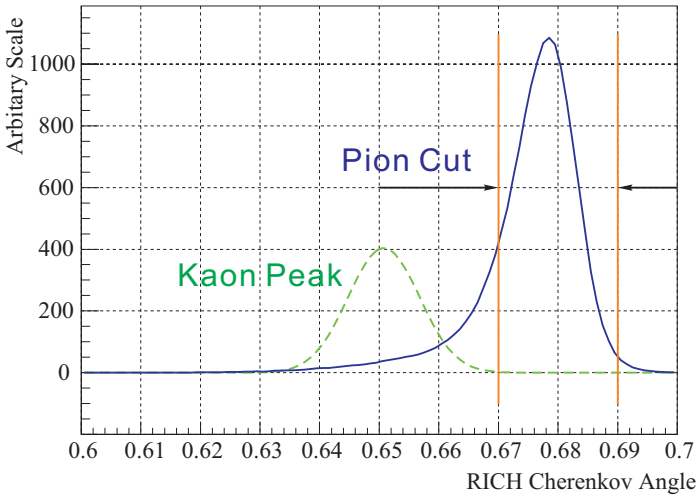

Figure 3-11: RICH angle cut used in pion selection, there will be less than 0.1% kaon remaining after the cut.

For Aerogel 1 this method was not valid since the N.P.E. could not be extracted by using equation 3.8, except for the electrons. Therefore, by only fitting the electron data ($\beta \approx 1$), the maximum N.P.E. was obtained:

$$N.P.E._{A1} = 3.82 \pm 0.15. \tag{3.13}$$

A1 Efficiency

Because the A1 ADC spectrum could not be reproduced analytically, the efficiency of Aerogel 1 was calculated using experimental data. Since π^+ dominated the singles data of left HRS at positive polarity, the selection of pions was very clean with simple cuts, as shown in Figure 3-11.

With such pure pion samples, the efficiency of the Aerogel 1 cut for pion ($A1 > 20$), was obtained:

$$\eta_\pi(A1) = 95.6 \pm 1\%, \tag{3.14}$$

as shown in Figure 3-12.

Unlike pion, the kaon efficiency of A1 could not be calculated directly since the kaon identification depends greatly on A1. Therefore another method was used to

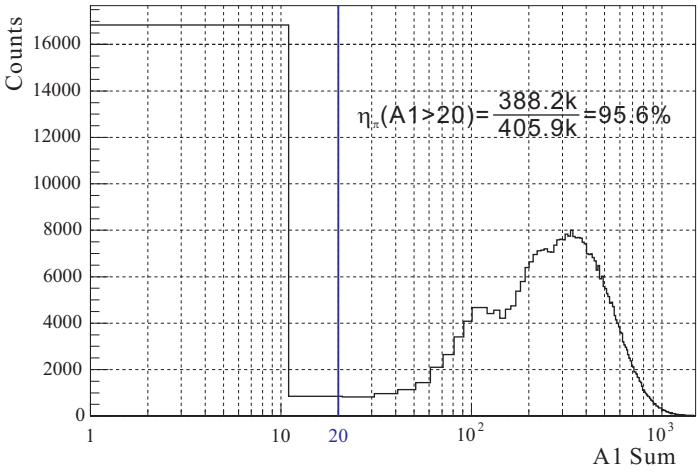

Figure 3-12: Aerogel 1 PID efficiency for pions.

bypass it. The low momentum (550 MeV/c) pion data were taken for this purpose. At 550 MeV/c, the pion has very similar velocity as kaon at 2.0 GeV/c:

$$\beta_\pi(550 \text{ MeV}/c) = 0.9712 \tag{3.15}$$

$$\beta_K(2.0 \text{ GeV}/c) = 0.9707. \tag{3.16}$$

The response of Aerogel 1 to these two kinds of particles should be very similar. On the other hand, the π^+ is the only particle which can fire Aerogel 2 at this momentum, and was easily identified. The efficiency was

$$\eta_K(A1) \approx \eta_\pi(A1 : 550 \text{ MeV}/c) = 90.8 \pm 2\%, \tag{3.17}$$

as shown in Figure 3-13.

A2 Efficiency

The Aerogel 2 detector was only used in kaon identification. Since the experimental shape agreed very well with the analytical description, the efficiency was calculated using formula (3.8) and parameters obtained in (3.10-3.12). As mentioned before, at around 2 GeV/c both kaon and pion fire Aerogel 2. Therefore the A2 cut selection needed to take account both the kaon selection and pion rejection. Figure 3-14

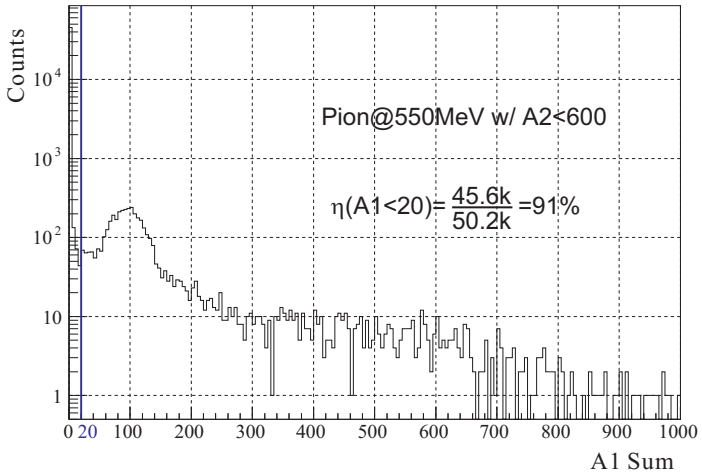

Figure 3-13: Aerogel 1 veto efficiency for kaons (using pion data at 550 MeV/c).

demonstrates the cut selection at 2.2 GeV/c: the blue squares show the ratio of kaons passing the cut while the red triangles show the ratio of remaining pions.

The cut on kaons was finally selected at the 96% level. At this level, the pions are greatly rejected while the majority of kaons survive. For 2.22 GeV/c, around 45% of pions get rejected and as the momentum decreases the rejection ratio goes up to 70% for 1.89 GeV/c.

3.5.2 RICH Detector

The RICH detector was used to enhance the performance of pion rejection in kaon data. Because the detector needed at least 3 points on a Cherenkov ring to calculate the Cherenkov angle, the efficiency was defined as ratio of kaons with at least 3 photons detected by the RICH detector. To evaluate its efficiency a clean sample of kaon was also required, therefore the low momentum 550 MeV/c pion data were used once again to simulate the kaon at about 2 GeV/c. The efficiency using this method was determined to be

$$\eta_K(RICH) = 62 \pm 2\%. \tag{3.18}$$

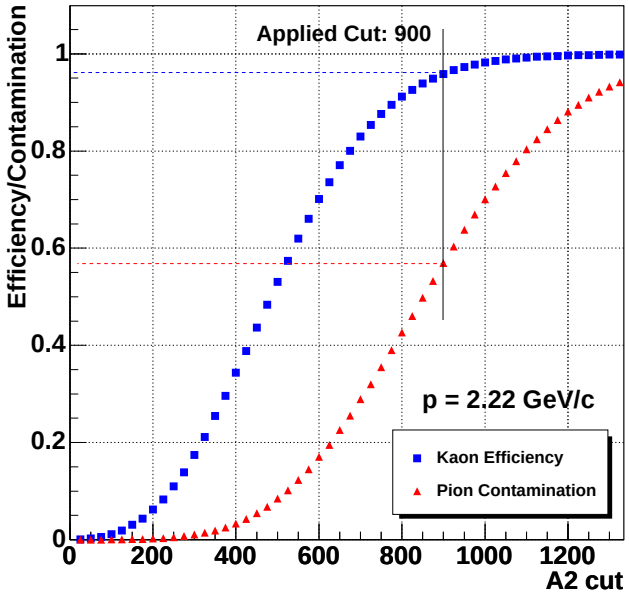

Figure 3-14: Selection of Aerogel 2 cut for kaons.

3.5.3 Gas Cherenkov

The CO_2 gas Cherenkov was used to select electron events in the right spectrometer. It was the only PID detector used in this arm because only electrons had enough speed to create Cherenkov light in the gas media.

To get the efficiency, pion-electron coincidence from neutron production was used:

$$e(p, e'\pi^+)n.$$

The neutron was identified in the missing mass spectrum. There was a competitive coincidence reaction which also introduced π^- in the right spectrometer:

$$e(p, \pi^-\pi^+)ep.$$

At 2 GeV/c, the difference between the pion and electron TOF was only around 0.2 ns. This difference could not be resolved with the experimental $\sigma_{TOF} \approx 600\ ns$ (see section 3.4.1). In this reaction, the coincidence missing mass is the invariant

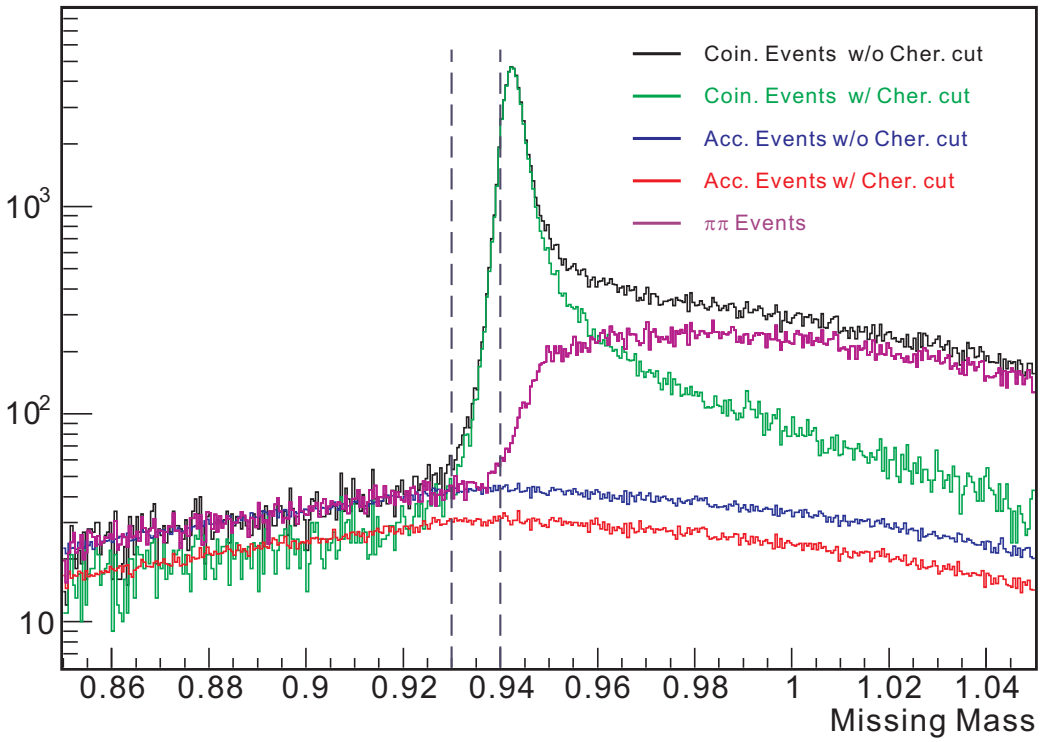

Figure 3-15: Efficiency measurement of gas Cherenkov detector. The accidental events are scaled by the ratio of coincidence window to accidental window.

mass of ep system starting from certain threshold.

In the missing mass reconstruction, all particles detected in right spectrometer were treated as electrons and the mis-identified pions, in this reaction, shifted the distribution due to its mass. Considering the mass difference between neutron and proton, the total shift of this threshold from neutron peak was calculated as

$$M_{ep}^{min} = M_n + 3.126 \text{ MeV}/c^2. \tag{3.19}$$

The neutron peak was measured at 942.5 MeV/c^2 with resolution $\sigma = 1.86$ MeV/c^2 therefore the threshold started from 945.6 MeV/c^2. Since the missing mass resolution smeared the contamination even lower than the threshold, a cut of 946.6 MeV/$c^2 - 2\sigma$ was used to exclude the $\pi^-\pi^+$ coincidence events as shown in Figure 3-15.

The electron detection efficiency for the gas Cherenkov was calculated using the ratio of pure neutron coincidence events after accidental background subtraction, with

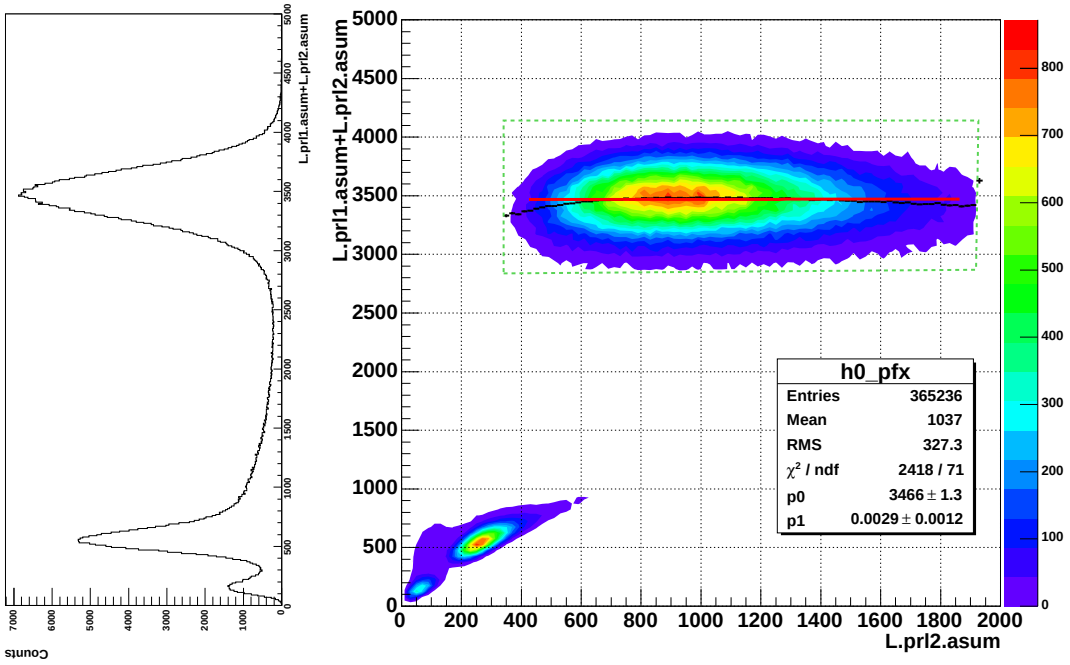

Figure 3-16: Left plot: sum of both pion rejectors' output amplitudes. Right plot: sum vs signal from pion rejector 2. The red markers show the average amplitude of electrons selected by the green dots. The fit using first order polynomial which is presented in red line indicates a negligible slope.

or without gas Cherenkov selection:

$$\eta_e(Gas) = \frac{\int_{930\ \mathrm{MeV}/c^2}^{M_n+3.126-3\sigma}(\text{Events selected by Cherenkov cut})}{\int_{930\ \mathrm{MeV}/c^2}^{M_n+3.126-3\sigma}(\text{Events without Cherenkov selection})} = 99.3 \pm 0.5\%. \quad (3.20)$$

3.5.4 Pion Rejector

The pair of pion rejectors installed in the left HRS was used to veto electron events when the polarity of the arm was set to negative. In this kinematic setting, only the kaon channel, $H(e, e'K^-)X$, was interesting.

The single photon peak calibration for both pion rejectors provided a very good separation between electrons and hadrons in the summed amplitude to the two pion rejectors, as shown in Figure 3-16. The larger amplitudes came from electron showers and the smaller signals are from hadrons. To select a proper cut on the total ampli-

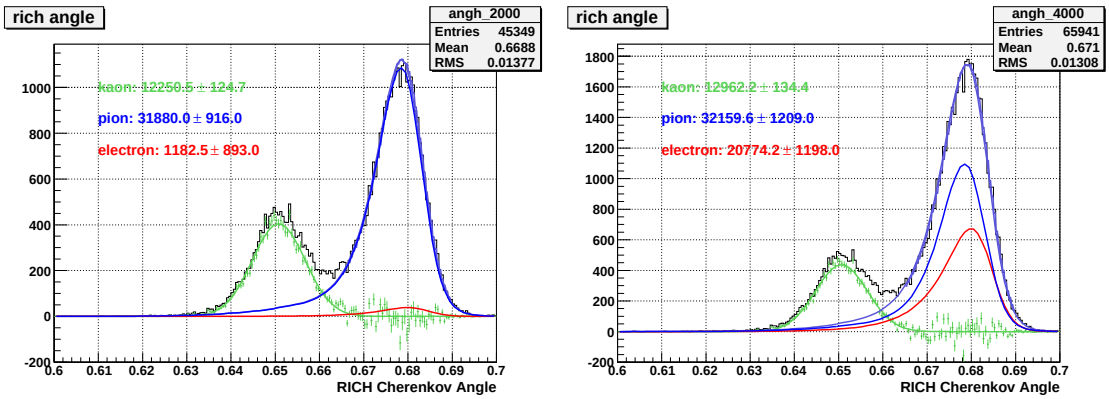

Figure 3-17: The fit of Cherenkov angle distribution reconstructed by RICH detector. The shapes of pions (blue) and electrons (red) are obtained using tight identification on both pion rejector and Aerogel detectors. The kaon contamination in these samples is extremely low and negligible.

tude, the surviving rates for kaons and electrons were studied using RICH Cherenkov angle spectra.

At 2 GeV/c, electrons and pions have very similar velocity and could not be separated by Cherenkov angles reconstructed by RICH. Fortunately, the distributions of Cherenkov angles of these two particles are not exactly the same and were obtained by using clean samples selected by tight Aerogel and pion rejector cuts. To get the number of kaons, one first fits the larger peak in the RICH angle using the linear combination of the electron and pion shapes. Then the distribution and the number of kaons are calculated by subtracting the electron and pion parts from the total spectrum. Figure 3-17 shows the fit using different pion rejector cuts (only events with less amplitude than that cut are selected) and Figure 3-18 plots the number of kaons and electrons after different cuts.

In the plot of kaons, the total number of events was found to be 1.3×10^4 by averaging the last few points and the cut of 2500 was selected. The efficiency of kaon selection was

$$\eta_K(PR < 2500) = 98.0 \pm 1.1\% \tag{3.21}$$

while the electron rejection ratio was about 93%.

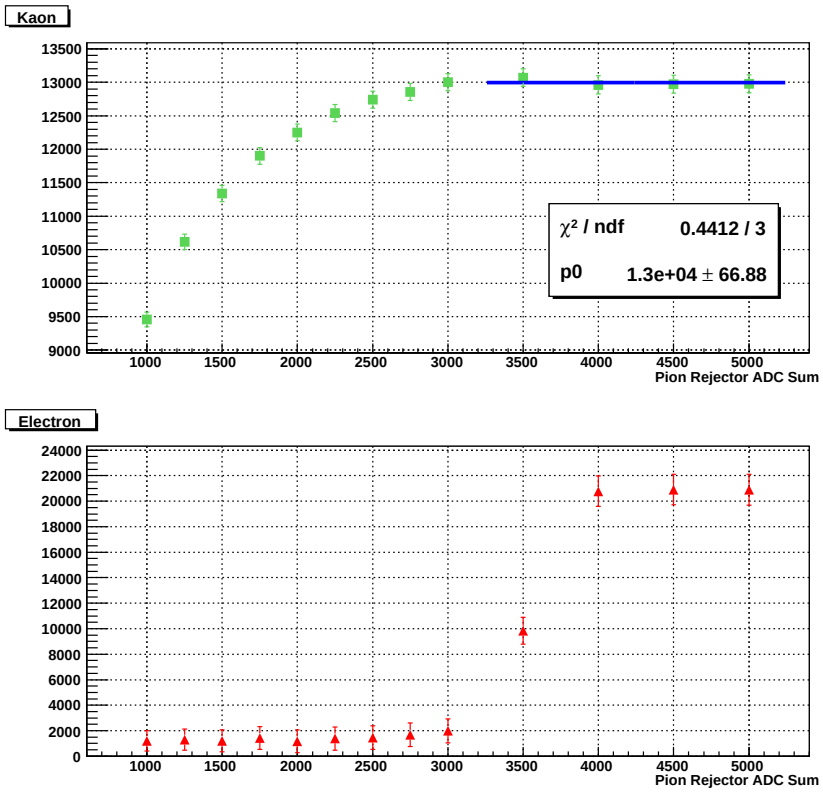

Figure 3-18: The number of kaons and electrons survived from different pion rejector cuts.

3.6 Correction Profiles and Trigger Efficiency

Before the missing mass spectra were finally extracted, it was very crucial to verify the uniformity of single arm momentum spectra. There are several factors which contributed to an nonuniform shape:

- VDC tracking efficiency,
- Solid angle acceptance, and
- PID trigger efficiency: T7[3].

3.6.1 VDC tracking efficiency

Particles with different momenta have different bending angles in septum magnets and dipoles. With the focusing feature of HRS dipoles the vertical (out-of-plane) position $x_{\rm fp}$, where particle pass the focal plane, is dominately a function of relative momentum δ. Therefore, the VDC tracking efficiency can simply be expressed as a function of δ:

$$\eta_{VDC}(x_{\rm fp}) = \eta_{VDC}(\delta).$$

The relative efficiency profile of the focal plane with respect to the center, where $x = 0$ and roughly $\delta = 0$, was determined using a "white spectra" technique during earlier experiments [89, 90, 91].

The basic principal of the white spectra technique is to measure the same cross section at several points along the focal plane. The change in the yield measured at different points reflects the variation of focal plane efficiency among these points. The use of a white spectrum (a smoothly varying distribution) instead of a sharp peak allows one to cover the entire focal plane in several steps. Such analysis shows the absolute efficiency at the center of the focal plane is $100.0 \pm 3.0\%$ for both spectrometers.

Therefore, it's safe to define the relative efficiency profile by comparing the efficiency at other positions to the central point $\delta = 0$.

[3]The definition of T7 can be referred in Section 2.7.2

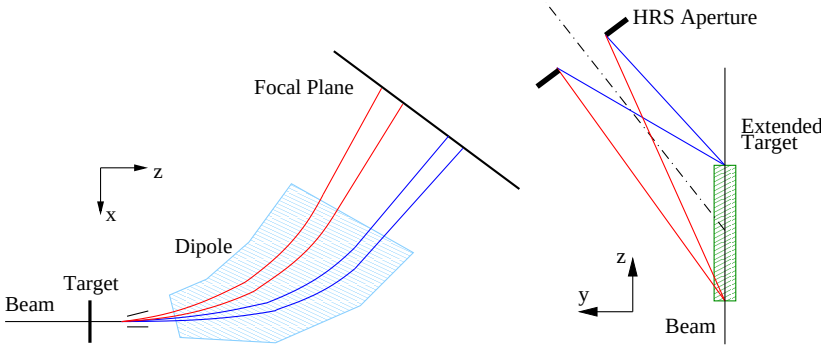

Figure 3-19: The dispersion of the dipole magnet and the relations between solid angle acceptance and reaction position in target.

3.6.2 Angular Acceptance Parametrization

The solid angle coverage is a different story. As can be seen in Figure 3-19, the solid angle acceptance is a function of reaction point $Z_{\rm react}$ and relative momentum δ: $\Delta\Omega(z,\delta)$. For a fixed collimator, the more forward the reaction point, the larger the observed acceptance.

The total efficiency of the single arm momentum spectrum is the convolution of detector efficiency and solid angle acceptance:

$$A(\delta) = \eta_{VDC}(x) \otimes d\Omega(Z,\delta) = \frac{1}{\Delta Z}\int \eta_{VDC}(\delta)\cdot d\Omega(Z,\delta)dZ. \qquad (3.22)$$

Since the VDC efficiency is a single-parameter function of the relative momentum δ, it is more convenient if such $Z_{\rm react}$ dependence of $d\Omega$ can be integrated over and removed. To the contrary, if $Z_{\rm react}$ and δ have strong correlation in $d\Omega$, the two-parameter solid angle function needs to be calculated.

3.6.3 Separation of $Z_{\rm react}$, δ in $d\Omega$

To obtain the relations between Z_{react}, δ and $d\Omega$, each arm were sampled at 6 positions of Z in the total 15 cm extended target. At each position the acceptance was measured at 6 different δ. This results in each spectrometer having 36 solid angle acceptance values. The results are listed in Table 3.2 and Table 3.3. Figure 3-20 shows part of

$\Delta\Omega_L$ (msr)		Reaction Z (cm)					
		-6.25±1	-3.75±1	-1.25±1	1.25±1	3.75±1	6.25±1
δ	-3%±0.5%	4.11±0.08	4.22±0.06	4.29±0.06	4.39±0.14	4.35±0.10	4.16±0.18
	-1.5%±0.5%	4.09±0.06	4.22±0.14	4.40±0.16	4.47±0.16	4.44±0.07	4.26±0.15
	0±0.5%	4.00±0.18	4.16±0.06	4.34±0.12	4.47±0.14	4.49±0.09	4.30±0.11
	1.5%±0.5%	3.93±0.08	4.14±0.12	4.29±0.11	4.47±0.13	4.54±0.11	4.35±0.14
	3%±0.5%	3.94±0.08	4.11±0.12	4.25±0.11	4.41±0.12	4.49±0.08	4.35±0.14
	4%±0.5%	3.38±0.27	3.51±0.24	3.64±0.22	3.79±0.23	3.81±0.24	3.74±0.23

Table 3.2: The solid angle measured in left HRS.

$\Delta\Omega_R$ (msr)		Reaction Z (cm)					
		-6.25±1	-3.75±1	-1.25±1	1.25±1	3.75±1	6.25±1
δ	-3%±0.5%	4.14±0.47	4.42±0.07	4.70±0.08	4.80±0.09	4.77±0.08	4.60±0.09
	-1.5%±0.5%	3.92±0.06	4.27±0.08	4.44±0.06	4.55±0.05	4.71±0.05	4.58±0.05
	0±0.5%	4.02±0.09	4.20±0.06	4.36±0.04	4.62±0.07	4.68±0.05	4.66±0.06
	1.5%±0.5%	3.99±0.07	4.23±0.08	4.38±0.06	4.57±0.07	4.75±0.08	4.59±0.05
	3%±0.5%	3.88±0.07	4.06±0.07	4.23±0.07	4.41±0.06	4.50±0.06	4.43±0.06
	4%±0.5%	3.23±0.14	3.53±0.09	3.80±0.08	3.95±0.09	4.02±0.08	4.06±0.10

Table 3.3: The solid angle measured in right HRS.

the solid angle plots from left HRS.

The ratios of solid angles for different reaction points to the center of target with different momenta were then calculated and such curves are plotted in Figure 3-21. As one can see, the ratios from different momentum have at most 4 % deviation at the two edges of the target. The average ratio shows a even smaller difference, as shown in the right panel of Figure 3-21. Therefore one can conclude that the δ and $Z_{\rm react}$ are approximately independent in solid angle.

Thus, equation(3.22) can be rewritten as

$$A(\delta) = \frac{1}{\Delta Z}\int \eta_{VDC}(\delta)\cdot\eta_{\Omega}(\delta)\cdot d\Omega(Z,\delta=0)dZ = \eta(\delta)\cdot\Delta\Omega, \tag{3.23}$$

where

$$\eta(\delta) = \eta_{VDC}(\delta)\cdot\eta_{\Omega}(\delta) \tag{3.24}$$

$$\Delta\Omega = \frac{1}{\Delta Z}\int d\Omega(Z,\delta=0)dZ. \tag{3.25}$$

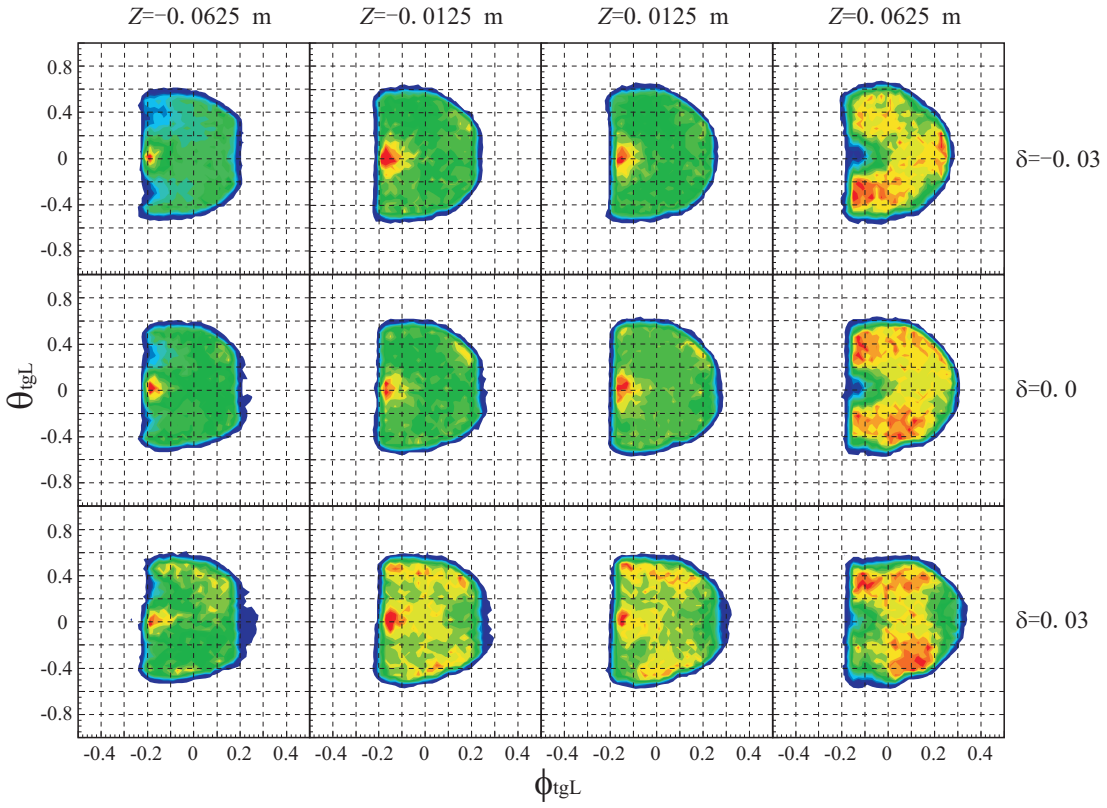

Figure 3-20: Solid Angle Acceptance of left HRS as a function of momentum and position.

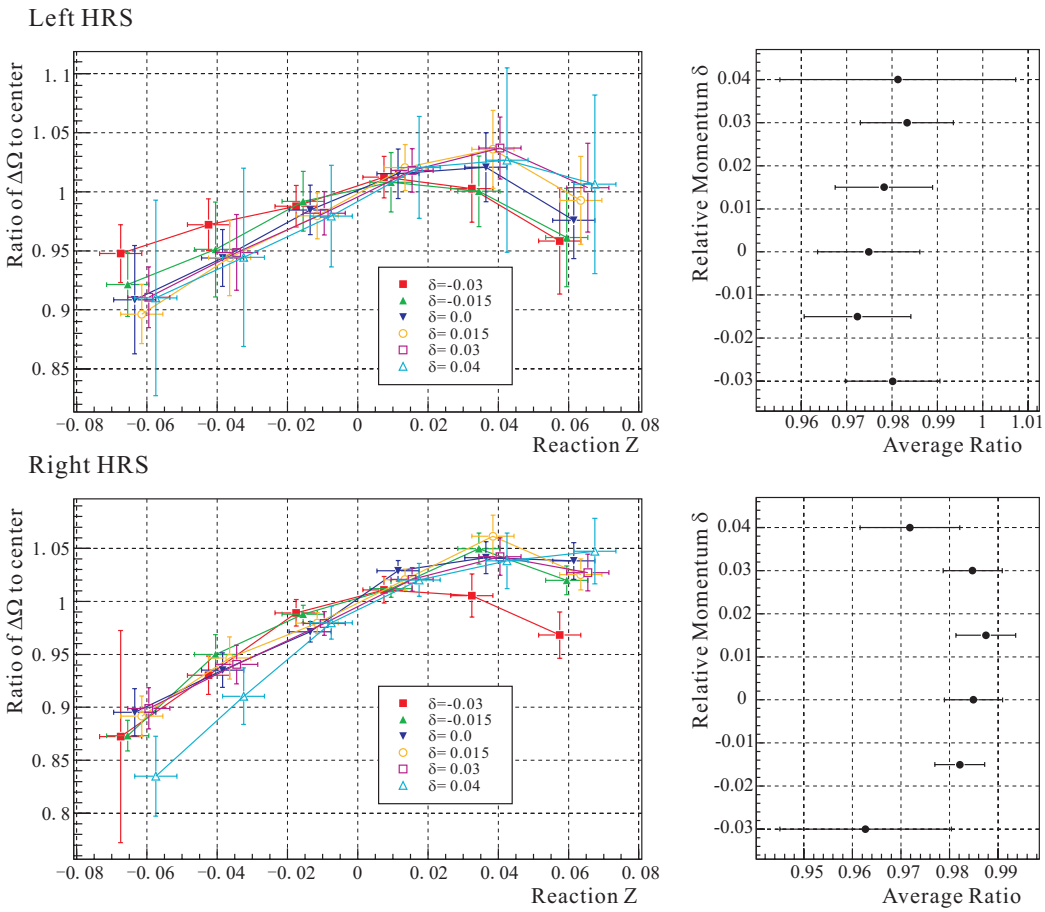

Figure 3-21: Left: the ratios of solid angles to the central ($Z_{\rm react}$=0) value with different δ (note that the curves of different δ are shifted a little bit in Z_{react} for a better presentation). Right: averages of ratios for different δ.

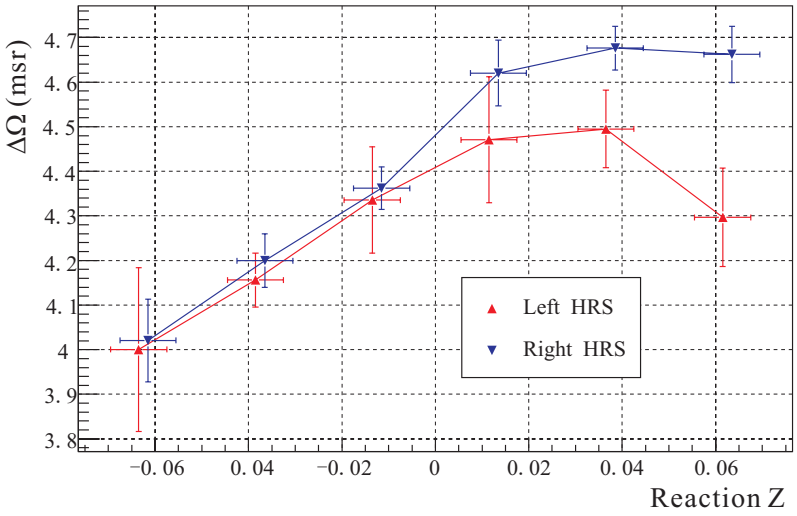

Figure 3-22: Solid angle acceptances measured from different target positions at central momentum ($\delta = 0$).

Based on the measurements of solid angle at central momentum, plotted in Figure 3-22, the average solid angles for both HRS were obtained:

$$\Delta\Omega_L = 4.29\ msr \tag{3.26}$$

$$\Delta\Omega_R = 4.42\ msr. \tag{3.27}$$

3.6.4 Cross Section Slopes

From the understanding of angular acceptance and the separation of equation (3.23), the single arm correction is now simplified into a profile of momentum as equation (3.24). To calculate it, the production cross section slope along the momentum for one kind of particular particle , π in our case, in each spectrometer needed to be determined.

For each momentum setting, the yield of particles was measured in a very narrow slice around central momentum ($|\delta| < 0.5\%$) to bypass the complicated convoluation of efficiency $\eta(\delta)$ and cross section $\sigma(p)$. The yield can be expressed as following,

$$N(p_0) = L \cdot \sigma(p_0) \cdot \eta_s(p_0) \cdot \eta(\delta = 0) \cdot \Delta\Omega(\delta = 0) \cdot \Delta p, \tag{3.28}$$

where p_0 is the central momentum of the setting, η_s is survival rate of this type of particle traveling from target to S2 scintillator, $\eta(\delta)$ is total efficiency defined in equation (3.24) and $\Delta p = p_0 \cdot \Delta\delta$ is the 1% momentum cut.

One problem arose from this method. During the running of E04-012, the single arm triggers: T1 and T3 for right and left HRSs were always strongly pre-scaled so that the direct analysis of the such data was impossible. On another hand, the rates of coincidence events were dependent on the cross section on both arm and complicated the effort to extract singles cross sections.

Fortunately, the total numbers of T1 and T3 triggers were recorded with scalers for every run. And the ratio of the interesting events to total events were found from coincidence triggers (T5 or T7) by applying an accidental cut on coincidence time spectrum. The multiplication of these two numbers resulted in the yield $N(p)$.

Yield Ratio

To reiterate, T5 and T7 were two types of the coincidence triggers. T5 was a plain trigger with only signals from scintillators and T7 had additional kaon identification cut to suppress pion events. The detailed definitions of these triggers are found in section 2.7.

To reduce the computer dead time and get more eK coincidence events, T5 triggers were typically pre-scaled by a factor of 3-6 and T7 triggers were all kept. For each event, it is possible to have multiple trigger types. So the total number of actual coincidence event was obtained as

$$N_{tot} = N_7 + PS_5 \cdot N_{\bar{7}5}, \tag{3.29}$$

where N_7 is the total number of T7 events (whether or not they were coincident with a T5 event), PS_5 is the pre-scale factor for T5 and $N_{\bar{7}5}$ is the number of events with only T5.

The following types of events were obtained in the accidental window:

N_7^L : Number of events of T7 in left HRS,

$N_{\bar{7}5}^L$: Number of events of T5 only in left HRS,

$N_7^\pi(\delta=0)$: Number of π^+ of T7 in left HRS with $\delta \approx 0$,

$N_{\bar{7}5}^\pi(\delta=0)$: Number of π^+ of T5 only in left HRS with $\delta \approx 0$,

N_7^R : Number of events of T7 in right HRS,

$N_{\bar{7}5}^R$: Number of events of T5 only in right HRS,

$N_7^e(\delta=0)$: Number of e^- of T7 in right HRS with $\delta \approx 0$,

$N_{\bar{7}5}^e(\delta=0)$: Number of e^- of T5 only in right HRS with $\delta \approx 0$.

The ratio of π^+ and e^- in each arm are calculated as

$$P(\pi^+) = \frac{N_7^\pi + PS_5 \cdot N_{\bar{7}5}^\pi}{N_7^L + PS_5 \cdot N_{\bar{7}5}^L} \tag{3.30}$$

$$P(e^-) = \frac{N_7^e + PS_5 \cdot N_{\bar{7}5}^e}{N_7^R + PS_5 \cdot N_{\bar{7}5}^R}. \tag{3.31}$$

The Singles Cross Section

Following equation (3.28), the cross section of certain type of particles (π^+ for example) in left HRS is

$$\sigma^\pi(p_0^L) = \frac{N_3 \cdot P_\pi}{L \cdot \eta_s^\pi(p_0^L) \cdot \eta(\delta=0) \cdot \Delta\Omega(\delta=0) \cdot p_0^L \cdot \Delta\delta}. \tag{3.32}$$

where N_3 is the total number of triggers collected in left HRS during the run, P_π is the ratio of the number of pions within the 1% δ cut to the total number of events detected by the left HRS, L is the luminosity which is proportional to the total charge of the run, and η_s^π is the π^+ survival rate from decay. $\eta(\delta=0)$, $\Delta\Omega$ and $\Delta\delta$ are constants for all momentum settings.

η_s^π can be calculated using exponential decay principle: after travel through 27.25 m's HRS path, the survival rate of pion is

$$\eta_s^\pi(p_0^L) = e^{-\frac{t}{\gamma\tau}} = e^{-\frac{L}{\beta\gamma\tau c}}, \tag{3.33}$$

where $\tau = 2.603 \times 10^{-8}$ s, $L = 27.25$ m.

The actual number of pions produced in left spectrometer with central momentum is

$$N_\pi = \frac{N_3 \cdot P_\pi}{\eta_s^\pi(p_0^L)}. \tag{3.34}$$

Then equation (3.32) can be simplified:

$$\sigma^\pi(p_0^L) \propto F_\pi = \frac{N_\pi}{Charge \cdot p_0^L}, \tag{3.35}$$

and the plot of this new quantity F_π will give the curve of π^+ production cross section with an arbitrary scale.

In a similar way, the quantities for e^- in right HRS are

$$N_e = N_1 \cdot P_e \tag{3.36}$$

$$F_e = \frac{N_e}{Charge \cdot p_0^R}. \tag{3.37}$$

The values F_π and F_e calculated from different momentum settings are listed in Table 3.4.

π^+ Production Cross Section in HRS-L

The plot of F_π is shown in Figure 3-23. The error bars include statistical error combined with the uncertainty of beam charge and PID. The fit of the data shows good agreement with a linear function with higher order polynomials bring no significant χ^2 improvement. The cross section curve is numerically expressed as

$$\sigma^{\pi^+}(p) = Const. \cdot F_\pi(p) = Const. \cdot (1282 - 377 \cdot p). \tag{3.38}$$

Electron Cross Section in HRS-R

The cross section of electron scattering can only be well fitted with a second-order polynomial as shown in Figure 3-24. It gives

$$\sigma^{e^-}(p) = Const. \cdot F_e(p) = C \cdot (1374 - 805.6 \cdot p + 184.8 \cdot p^2). \tag{3.39}$$

	kin1	kin3	kin4	kin5	kin6	kin7	kin10	kin11	kin12	kin13
E_{beam} (GeV)	5.01									
p_0^L (GeV/c)	2.49	2.22	2.10	1.93	1.93	1.90	1.93	1.93	1.93	1.89
p_0^R (GeV/c)	2.50	2.50	2.00	2.00	1.93	1.70	1.83	1.98	2.02	1.85
η_s^π (%)	82.38	80.46	79.47	77.87	77.87	77.55	77.87	77.87	77.87	77.45
Charge (C)	0.07833	0.07236	0.07447	0.07269	0.07454	0.17981	0.15328	0.08164	0.08800	0.09001
N_L	706.11M	758.70M	824.83M	869.31M	892.34M	2177.88M	1838.34M	977.26M	1053.40M	1095.32M
N_R	1442.59M	1317.47M	1239.85M	1209.93M	1231.25M	2869.34M	2497.55M	1357.77M	1470.35M	1467.62M
P_π (%)	7.86	7.54	7.34	6.99	6.99	6.88	6.95	7.00	6.99	6.84
P_e (%)	7.03	7.03	6.03	6.04	5.94	5.74	5.82	6.00	6.03	5.83
N_π	55.47M	57.18M	60.56M	60.77M	62.35M	149.82M	127.83M	68.40M	73.67M	74.90M
N_e	101.40M	92.60M	74.80M	73.07M	73.17M	164.76M	145.27M	81.50M	88.67M	85.57M
F_π	345.20	442.40	487.30	556.30	556.60	565.50	554.90	557.50	557.00	568.50
F_e	517.80	511.90	502.20	502.60	508.60	539.00	517.90	504.20	498.80	513.90

Table 3.4: Arbitrary yield of π^+ and e^- in different kinematics settings.

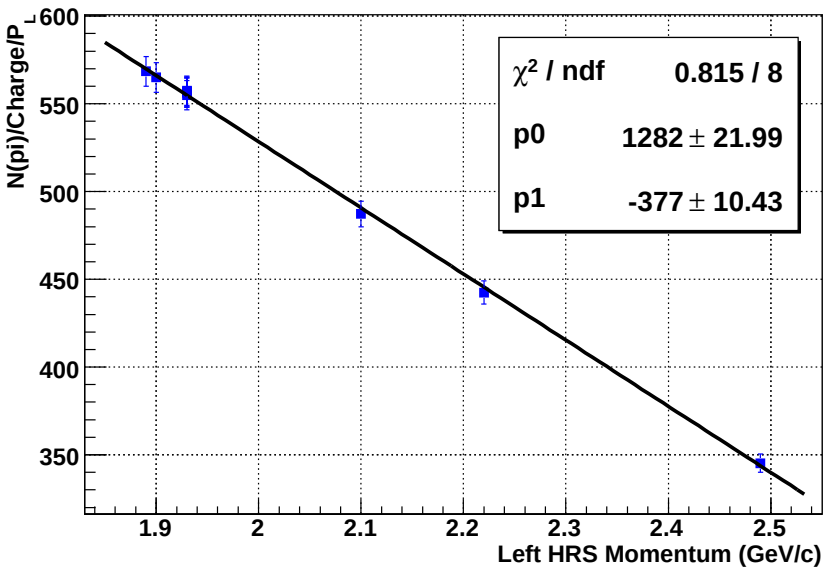

Figure 3-23: π^+ production rate measured by the left HRS.

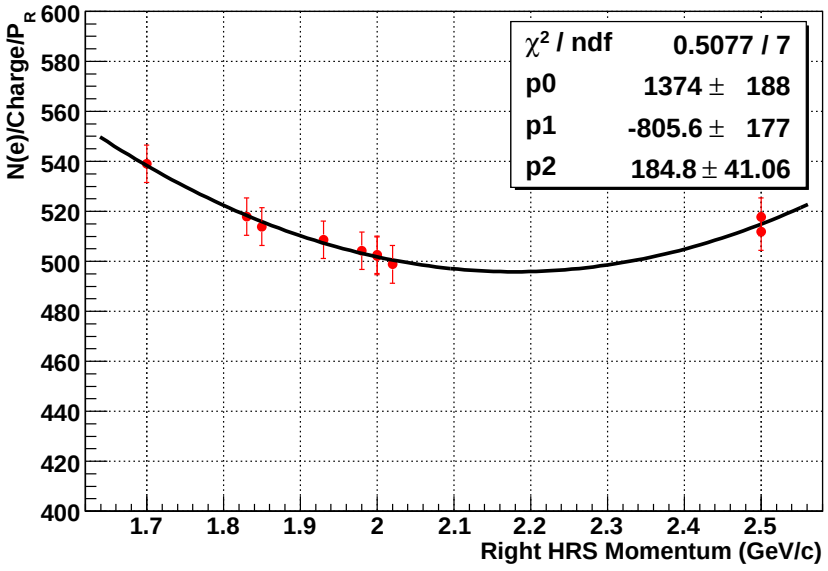

Figure 3-24: e^- production rate measured by the right HRS.

3.6.5 Efficiency Profile

Once the singles slopes are known, it's quite easy to get the efficiency $\eta(\delta)$ which is defined in equation (3.24). Assuming the 100% efficiency at the center of the focal plane, the left HRS efficiency for example, was calculated using the following formula

$$\eta_L(\delta) = \frac{\eta_s^\pi(p_0^L) \cdot S_\pi^L(\delta) \cdot F_\pi(p_0^L)}{\eta_s^\pi((1+\delta)p_0^L) \cdot S_\pi^L(\delta=0) \cdot F_\pi((1+\delta)p_0^L)}, \tag{3.40}$$

where $S_\pi^L(\delta)$ is the counts at δ in the accidental π^+ momentum spectrum of left HRS and p_0^L is the central momentum.

For electrons, since there's no decay of free electrons, the η_s for survival rate was dropped:

$$\eta_R(\delta) = \frac{S_e^R(\delta) \cdot F_e(p_0^R)}{S_e^R(\delta=0) \cdot F_e((1+\delta)p_0^R)}. \tag{3.41}$$

3.7 Trigger Efficiency And Pre-scale Factors

As previously mentioned, T7 can be treated as a trigger of T5 plus kaon identification:

$$T_7 \subset T_5. \tag{3.42}$$

Since T5 was a simple trigger without combining any signals from PID detectors it has no efficiency issue. However, T7 suffered a huge efficiency loss due to the varying response of the detector blocks. Figure 3-25 shows accidental momentum spectrum with T7 compared to T5 events. Clearly, the T7 trigger efficiency was not uniform and the average efficiency was estimated to be about 60%.

With the pre-scale factor of T5 trigger, good events are categorized into 4 groups: N_{57}, $N_{\bar{5}7}$, $N_{5\bar{7}}$ and $N_{\bar{5}\bar{7}}$, as shown in Figure 3-26. With the average T7 efficiency η_7 and pre-scale factor of T5 PS_5, there are following relations with large statistics:

$$N_{tot} = N_{57} + N_{\bar{5}7} + N_{5\bar{7}} + N_{\bar{5}\bar{7}} \tag{3.43}$$

$$PS_5 = \frac{N_{tot}}{N_5} = \frac{N_{\bar{7}}}{N_{5\bar{7}}} = \frac{N_7}{N_{57}} \tag{3.44}$$

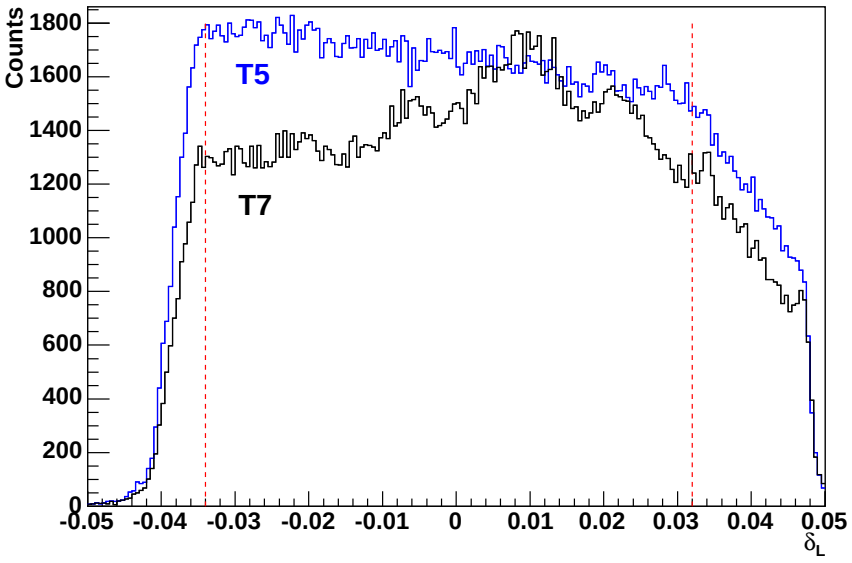

Figure 3-25: Left HRS momentum spectrum of trigger type 7 compared to T5 events (blue histogram with arbitrary scale). The dashed lines show the momentum acceptance cut.

$\bar{7}$	$N_{5\bar{7}}$	$N_{\bar{5}\bar{7}}$
7	N_{57}	$N_{\bar{5}7}$
	5	$\bar{5}$

Figure 3-26: The distribution of coincidence events.

$$\eta_7 = \frac{N_7}{N_{tot}} = \frac{N_{57}}{N_5} = \frac{N_{\bar{5}7}}{N_{\bar{5}}}. \tag{3.45}$$

$N_{\bar{5}\bar{7}}$ was easily calculated with two separate methods:

$$\begin{aligned} N_{\bar{5}\bar{7}} &= (PS_5 - 1) \cdot N_{5\bar{7}} \qquad \text{or} \\ N_{\bar{5}\bar{7}} &= N_{\bar{5}7} \cdot (\frac{1}{\eta_7} - 1) = \frac{N_{5\bar{7}} \cdot N_{\bar{5}7}}{N_{57}}. \end{aligned} \tag{3.46}$$

Obviously, if PS_5 equals to 1 (which means all trigger 5 data were recorded) there would be no $N_{\bar{5}\bar{7}}$ events. On another hand, a 100% kaon trigger efficiency ($\eta_7 = 1$) also leads to no $N_{\bar{5}\bar{7}}$ events.

3.7.1 Statistical Error for Pre-scaled Events

Before proceeding to the section on how to fill the hole of $N_{\bar{5}\bar{7}}$ events, it is important to understand how the statistical error of pre-scaled events should be calculated. Here is the discussion:

Probability Distributions [92]

First, two relevant probability distributions are described as following.

- **Poisson Distribution**

  The Poisson distribution gives the probability of finding exactly n events in a given interval of x when the events occur independently of one another and of x at an average rate of ν per given interval.

  The probability distribution function, p.d.f., mean and variance of Poisson are:

$$\begin{aligned} f(n;\nu) &= \frac{\nu^n e^{-\nu}}{n!} \\ \mu &= \nu \\ \sigma^2 &= \nu. \end{aligned} \tag{3.47}$$

The Poisson distribution approaches the limit of Gaussian distribution with infinite ν.

- **Binomial Distribution**

  If the probability of obtaining a certain outcome in each trail is p, then the probability of obtaining exactly r successes in N independent trials, without regard to the order of the successes and failures, is given by the binomial distribution:

$$\begin{aligned} f(r;N,p) &= \frac{N!}{r!(N-r)!}p^r(1-p)^{N-r} \\ \mu &= Np \\ \sigma^2 &= Np(1-p). \end{aligned} \tag{3.48}$$

  When the probability of p approaches the limit of 0, binomial distribution is becomes Poisson distribution.

Valid Distribution

Assuming N total events, after pre-scale factor S, the recorded number of events becomes N/S. Among these events the ratio of good events, kaons for example, is p. Obviously the average number of recorded kaons is:

$$\langle n_K \rangle = \frac{Np}{S} \tag{3.49}$$

According to the Binomial p.d.f. the variance of these data in the condition of fixed N is

$$\sigma_K^2 = \langle (n_K - \langle n_K \rangle)^2 \rangle = \frac{N}{S}p(1-p), \tag{3.50}$$

and the relative fluctuation is

$$\Delta\sigma_K = \frac{\sigma_K}{\langle n_K \rangle} = \sqrt{\frac{(1-p)S}{Np}} = \sqrt{\frac{1-p}{\langle n_K \rangle}}. \tag{3.51}$$

Now considering the fluctuation from N, according to Poisson Distribution the

relative fluctuation caused by N is

$$\Delta\sigma_N = \frac{\sigma_N}{N} = \sqrt{\frac{1}{N}}. \tag{3.52}$$

Combining the two fluctuations gives the overall fluctuation:

$$\Delta\sigma = \sqrt{(\Delta\sigma_N)^2 + (\Delta\sigma_K)^2} = \sqrt{\frac{p + (1-p)S}{Np}} = \sqrt{\frac{S}{Np} - \frac{S-1}{N}}. \tag{3.53}$$

If $p << 1$, the relative error becomes

$$\Delta\sigma = \sqrt{\frac{p + (1-p)S}{Np}} \approx \sqrt{\frac{S}{Np}} = \frac{1}{\sqrt{\langle n_K \rangle}}. \tag{3.54}$$

This result is consistent with the fact that in the limit of $p \to 0$, the binomial distribution turns to Poisson distribution.

On the contrary, in the limit of $p \to 1$ the error changes to

$$\Delta\sigma = \frac{1}{\sqrt{N}}, \tag{3.55}$$

and obviously, those unrecorded, pre-scaled events still contribute to the total statistics in this situation.

In the case of spectra analysis, counts in each bins are the objects being calculated. The p of good events in certain bin from total number of counts is always very small since hundreds of bins are "sharing the cake". Therefore, only those recorded events contribute to the statistical error and the data dropped by pre-scale factors are lost forever.

3.7.2 Best Estimation for Pre-Scaled Events

With the understanding of the statistical error, it is time to select an appropriate method to recover $N_{\bar{5}\bar{7}}$ data from equations of (3.46).

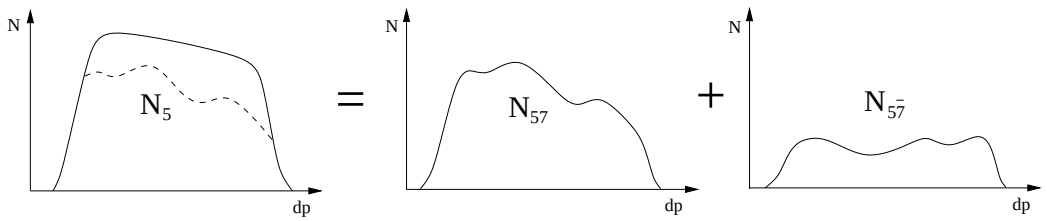

Figure 3-27: The constituent of T5 data.

Estimation for Kaons

- $N_{5\bar{7}}$ **approach**

  This method is very straight forward. The $N_{5\bar{7}}$ can be calculated using the first equation of (3.46):

  $$N_{5\bar{7}} = (PS_5 - 1) \cdot N_{5\bar{7}},$$

  and the uncertainty is

  $$\sigma_{5\bar{7}} = (PS_5 - 1) \cdot \sigma_{5\bar{7}} = (PS_5 - 1)\sqrt{N_{5\bar{7}}}. \tag{3.56}$$

  Due to the correlation of $N_{5\bar{7}}$ and $N_{\bar{5}\bar{7}}$, the total uncertainty is

  $$\begin{aligned} \sigma_{tot} &= \sqrt{(\sigma_{5\bar{7}} + \sigma_{\bar{5}\bar{7}})^2 + \sigma_{57}^2 + \sigma_{\bar{5}\bar{7}}^2} \\ &= \sqrt{N_{5\bar{7}} \cdot PS_5^2 + N_{57} + N_{\bar{5}\bar{7}}}. \end{aligned} \tag{3.57}$$

- $N_{\bar{5}7}$ **approach**

  This method comes from the second formula in (3.46) and the key is T7 efficiency η_7. As shown in Figure 3.7.2, the two components of T5 events, N_{57} and $N_{5\bar{7}}$, have opposite efficiencies. For $N_{\bar{5}7}$ and $N_{\bar{5}\bar{7}}$, we can expect similar result as expressed in (3.45).

A new quantity is defined from η_7 for convenience:

$$R_{\bar{7}7} = \frac{N_{\bar{7}}}{N_7} = \frac{1-\eta_7}{\eta_7}. \tag{3.58}$$

Clearly, the missing $N_{\bar{5}\bar{7}}$ is then given by

$$N_{\bar{5}\bar{7}} = R_{\bar{7}7} \cdot N_{\bar{5}7}. \tag{3.59}$$

There are two ways to calculate $R_{\bar{7}7}$ and they are given together with their errors:

$$R_{\bar{7}7} = \frac{N_{5\bar{7}}}{N_{57}} \pm \frac{1}{N_{57}}\sqrt{\frac{N_{5\bar{7}}(N_{57}+N_{5\bar{7}})}{N_{57}}} \tag{3.60}$$

and

$$R_{\bar{7}7} = \frac{PS_5 \cdot N_{5\bar{7}}}{N_{57}+N_{\bar{5}7}} \pm \frac{PS_5}{N_{57}+N\bar{5}7}\sqrt{\frac{N_{5\bar{7}}(N_{57}+N_{5\bar{7}}+N_{\bar{5}7})}{N_{57}+N\bar{5}7}}. \tag{3.61}$$

Obviously, the latter has smaller statistical error and was used in following analysis.

Not like the acceptance efficiency profile $\eta(\delta)$, $R_{\bar{7}7}$ is sensitive to the spectrometer momentum settings due to the fact that the T7 efficiency comes from the signal shape of Aerogel detectors and hardware threshold settings for triggers. The settings with higher momentum give larger Cherenkov signals in Aerogel detectors so that higher T7 efficiency is expected in these settings. Therefore such efficiency profile has to be prepared setting by setting. One complication arises from the uncertainty of $R_{\bar{7}7}$ becoming comparable to the statistical error of coincidence events because the accidental events have only about 10 times larger statistics than the coincidence events. To lower the uncertainty of $R_{\bar{7}7}$, the counts in each bin of the accidental kaon spectrum are replaced by the average value of the 10 adjacent bins. This is equivalent to reducing the total number of bins by a factor of 10 (from 600 to 60), and is reasonable because there were only 24 A1 PMTs and 26 A2 PMTs and 60 bins provides enough resolution to this variance.

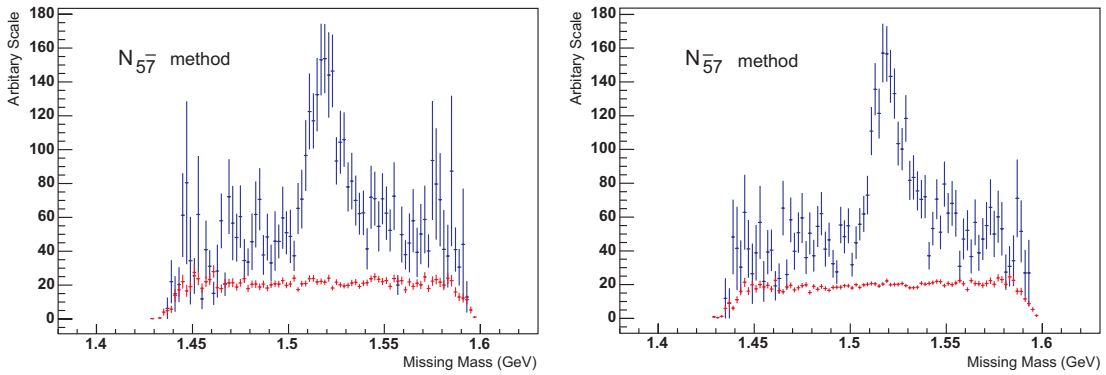

Figure 3-28: The comparison plots from $\Sigma(1520)$ peak (kin4). The blue points are coincidence events and red points are accidental background.

With such effort, the uncertainty of $R_{\bar{7}7}$ is at least one magnitude smaller than $N_{\bar{5}7}$ and is neglected in the calculation. The error of $N_{\bar{5}\bar{7}}$ is now given by

$$\sigma_{\bar{5}\bar{7}} = R_{\bar{7}7} \cdot \sigma_{\bar{5}7} = R_{\bar{7}7}\sqrt{N_{\bar{5}7}}, \tag{3.62}$$

and the total uncertainty of this approach is

$$\begin{aligned} \sigma_{tot} &= \sqrt{\sigma_{5\bar{7}} + \sigma_{\bar{5}7}^2 + (\sigma_{\bar{5}7} + \sigma_{\bar{5}\bar{7}})^2} \\ &= \sqrt{N_{5\bar{7}} + N_{\bar{5}7} + N_{\bar{5}7} \cdot (1 + R_{\bar{7}7})^2}. \end{aligned} \tag{3.63}$$

In kaon case, $N_{\bar{5}7}$ is typically 7 times larger than $N_{\bar{5}7}$ for $PS_5 = 6$ and $\eta_7 = 60\%$. According to the above discussion, the $N_{\bar{5}7}$ method brings 30% less uncertainty than $N_{5\bar{7}}$. The difference of these two approaches can be clearly identified from the comparison in Figure 3-28.

Estimation for Pions

For pions, since $N_{\bar{5}7}$ is overwhelmingly larger than $N_{5\bar{7}}$, the original $N_{\bar{5}7}$ approach is the best choice.

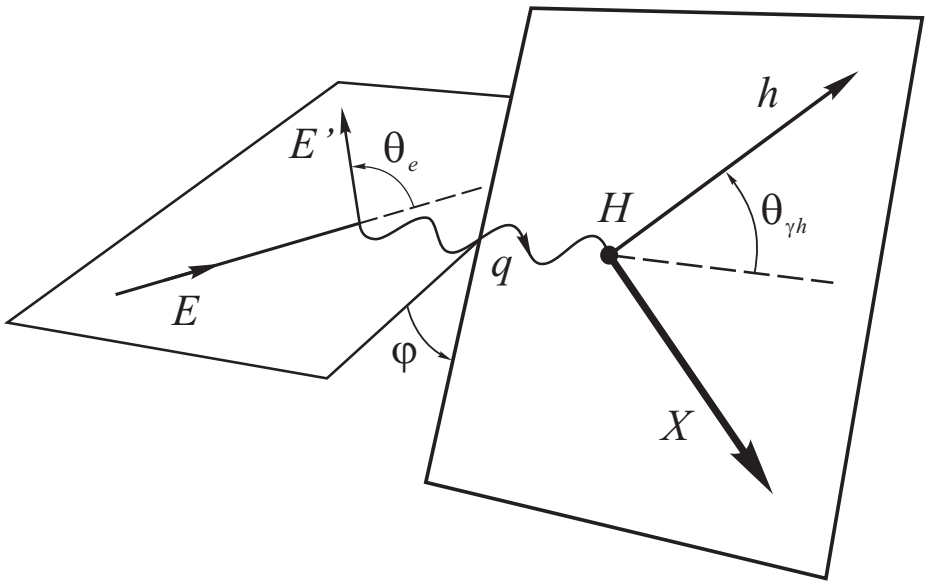

Figure 3-29: Kinematics for the $H(e,e'h)X$ reaction.

3.8 Cross Section Spectrum Calculation

The goal of this part of analysis is to calculate the differential cross section for the pentaquark production by virtual photons:

$$\gamma^* + H \rightarrow h + X. \tag{3.64}$$

3.8.1 Kinematics Variables and the Cross Section

As shown in Figure 3-29, in the reaction

$$e + H \rightarrow e' + h + X \tag{3.65}$$

there are five 4-momenta involved:

$e = (E, \vec{e})$ for the incident electron,

$e' = (E', \vec{e'})$ for the scattered electron,

$H = (M_H, 0)$ for the proton target,

$h = (E_h, \vec{h})$ for the produced meson: kaon or pion, and

$X = (E_X, \vec{x})$ for the residual system.

A few Lorentz invariants and other kinematics variables are defined below:

$$\begin{aligned} q^2 &= (e-e')^2 = -Q^2 \\ \nu &= E - E' \\ \epsilon &= [1 + 2\frac{\nu^2+Q^2}{Q^2} tan(\frac{\theta_e}{2})]^{-1} \\ s &= (q+H)^2 = W^2 \\ M_X^2 &= (e-e'+H-h)^2. \end{aligned}$$

The differential cross section for the electro-production of hadron h is presented as [8] [93]

$$\frac{d^4\sigma}{dE'd\Omega_{e'}d\Omega_h dM_X} = \Gamma \cdot \frac{d^2\sigma}{d\Omega_h dM_X}. \tag{3.66}$$

Γ is the virtual photon flux, given by

$$\Gamma = \frac{\alpha}{2\pi^2}\frac{E'}{E}\frac{s-M^2}{2MQ^2}\frac{1}{1-\epsilon} \tag{3.67}$$

and $\frac{d^2\sigma}{d\Omega_h dM_X}$ is the differential cross section for hadron h production by the virtual photon. Furthermore, if this cross section is represented in the central-mass system (CMS) of $\gamma^* H$, the cross section can also be used for the pentaquark production in an opposite direction:

$$\frac{d^2\sigma}{d\Omega_h dM_X}(\theta_{\gamma h}) = \frac{d^2\sigma}{d\Omega_X dM_X}(\theta_{\gamma X} = \pi - \theta_{\gamma h}). \tag{3.68}$$

In H(e,e'h)X coincidence experiments, what is measured is the counts over finite intervals of angular acceptance as well as energy for both the electron and the meson. Keeping the total degrees of freedom of the differential cross section, the energy of meson in the denominator can be replaced by the mass of residual. The cross section is expressed as

$$\frac{d^4\sigma}{dE'd\Omega_e d\Omega_h dM_X} = \frac{N_{M_X}}{L\Delta E'\Delta\Omega_e\Delta\Omega_h\Delta M_X}R, \tag{3.69}$$

where

N_{M_X}	is the number of counts in a single bin of missing mass,
L	is the luminosity,
$\Delta E'$	is energy acceptance of scattered electron,
$\Delta\Omega_e, \Delta\Omega_h$	are angular acceptance,
ΔM_X	is the bin size of missing mass spectrum, and
R	is the total correction factor including dead time, efficiency, etc..

Now the cross section for photo-production in lab system can be written as

$$\frac{d^2\sigma}{d\Omega_h dM_X}|_{lab} = \frac{N_{M_X} R}{\Gamma L \Delta E' \Delta\Omega_e \Delta\Omega_h \Delta M_X}. \tag{3.70}$$

The next step is to transform the cross section from lab system to CMS. The Jacobian is calculated as

$$\begin{aligned} J &= \begin{vmatrix} \frac{\partial\Omega_L}{\partial\Omega_C} & \frac{\partial\Omega_L}{\partial M_C} \\ \frac{\partial M_L}{\partial\Omega_C} & \frac{\partial M_L}{\partial M_C} \end{vmatrix} = \left|\frac{\partial\Omega_L}{\partial\Omega_C}\right| = \left|\frac{sin(\theta_L)}{sin(\theta_C)}\frac{\partial\theta_L}{\partial\theta_C}\right| \\ &= \left|\frac{sin(\theta_L)}{sin(\theta_C)}\gamma(1-\beta_C cos(\theta_L)/\beta_L)\right|. \end{aligned} \tag{3.71}$$

The cross section in CMS is given by

$$\begin{aligned} \frac{d^2\sigma}{d\Omega_h dM_X}|_{CMS} &= \frac{d^2\sigma}{d\Omega_h dM_X}|_{lab} \cdot J \\ &= \frac{N_{M_X} R J}{\Gamma L \Delta E' \Delta\Omega_e \Delta\Omega_h \Delta M_X}. \end{aligned} \tag{3.72}$$

3.8.2 Photon Flux Acceptance

In the final expression of the cross section, (3.72), all the other factors can be calculated event-by-event, except for $\Delta E'$.

As shown in Figure 3-30, the momentum acceptance cut selected a rectangular area in the two dimensional momentum plot (red dash frames). For very forward angle settings, as in this experiment, the missing mass of X can be approximated to

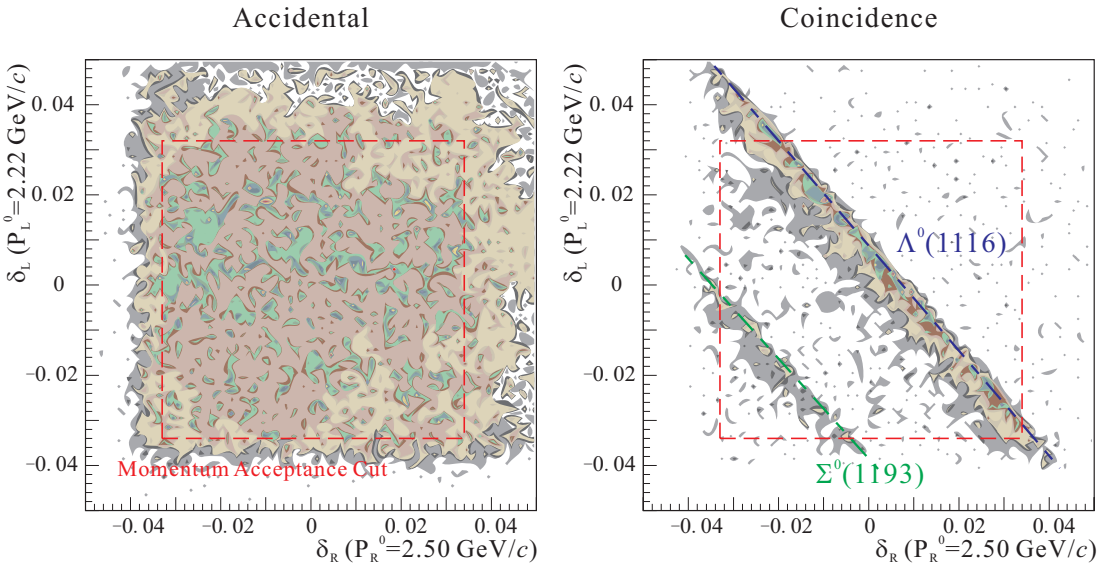

Figure 3-30: 2 Dimensional Momentum Acceptance.

a linear combination of momenta of the two detected particles:

$$M_X = \sqrt{(e + H - e' - h)^2} \approx C_1 - C_2 \cdot E_{e'} - C_3 \cdot E_h \approx C_1' - C_2' p_R^0 \delta_R - C_3' p_L^0 \delta_L, \quad (3.73)$$

with a precision better than 0.1% within the acceptance and C_2' and C_3' are very close to 1.

The events with the same missing mass form a straight line in the momentum acceptance plot, as $\Lambda^0(1116)$ and $\Sigma^0(1193)$ shown in Figure 3-30.

The $\Delta E'$ for a event is the total E' coverage of that missing mass: $\Delta E' = p_R^0 \Delta\delta_R$ and is proportional to the length of the missing mass contour in the momentum acceptance. With such knowledge, the missing mass spectrum of counts now can be corrected to a cross section spectrum with a scale factor as demonstrated in Figure 3-31.

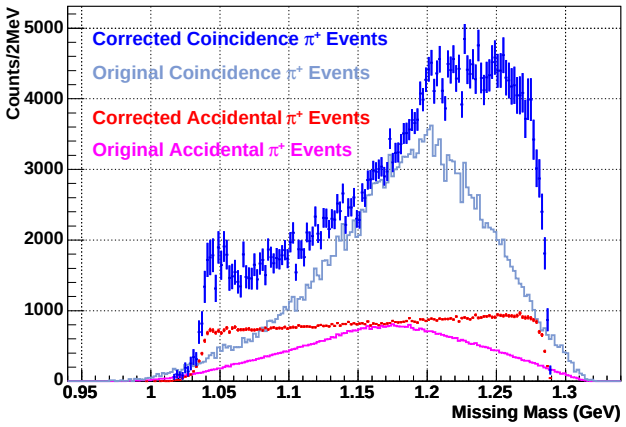

Figure 3-31: Demonstration of acceptance correction. The original accidental spectrum has a triangular shape with a small flat top. After photon-flux correction, it became completely straight. The $\Delta^0(1232)$ in the coincidence spectrum also shows correct position after correction.

3.8.3 Correction Factor: R

The correction factor R in equation (3.72) is a collection of all efficiencies:

$$R = \frac{1}{\eta\delta \cdot \eta_{PID} \cdot \eta_Z \cdot \eta_{ONE} \cdot \eta_s^h(\delta, p_0^L) \cdot L.T.}, \tag{3.74}$$

where

$\eta(\delta)$	is the relative efficiency for VDC and the solid angle,
η_{PID}	is the total efficiency for particle identification,
η_Z	is the efficiency for reaction vertex coincidence cut,
η_{ONE}	is the ratio for only one track events,
$\eta_S^h(\delta, p_0^L)$	is the survival ratio of meson h in left HRS, and
$L.T.$	is live time of the DAQ system.

Live Time

The DAQ live time is not 100% due to two factors:

Electronic Dead time Electronic dead time is due to the dead time of various electronic components and the pulse width of the trigger signals. Such dead

time is normally less than 100ns. With both arm's rates around 200 kHz, the total electronic dead time is estimated less than 1% and was thus negleted.

Computer Dead time Because the data acquisition system needs about 100 μs to acquire an event and the coincidence event rate was about 1 kHz, some of the coincidence events were not recorded to the data file. Such dead time is called computer dead time and the correction factor, so-called "live time", for coincidence events number can be calculated as

$$L.T. = \frac{T_5 \cdot PS_5}{S_5}, \tag{3.75}$$

where T_5 is the number of the events recorded in the data file, PS_5 is the pre-scale factor and S_5 is the total number of plain coincidence event triggers. During the experiment, the live time was typically 90%.

3.8.4 Background Subtraction

As described in section 3.4.1, the accidental background was subtracted by the ratio of the time-of-flight window according to equation (3.5):

$$N_{sig} = N_{coin} - \frac{W_{coin}}{W_{acc}} N_{acc}.$$

This method brought a very clean result. As Figure 3-32 shows, the cross section in the below-threshold region in both π^+ (neutron peak) and K^+ ($\Lambda^0(1116)$ peak) channels are consistent to 0.

The statistics of background spectrum is about one magnitude larger than the coincidence spectrum. Therefore in subtraction, the errors from background could be neglected. To make later analysis simpler and completely bypass such error, the background spectra were fitted by simple polynomials which have less than order of 2. The fitting functions were used to replace the background histograms in subtraction and introduce no additional error.

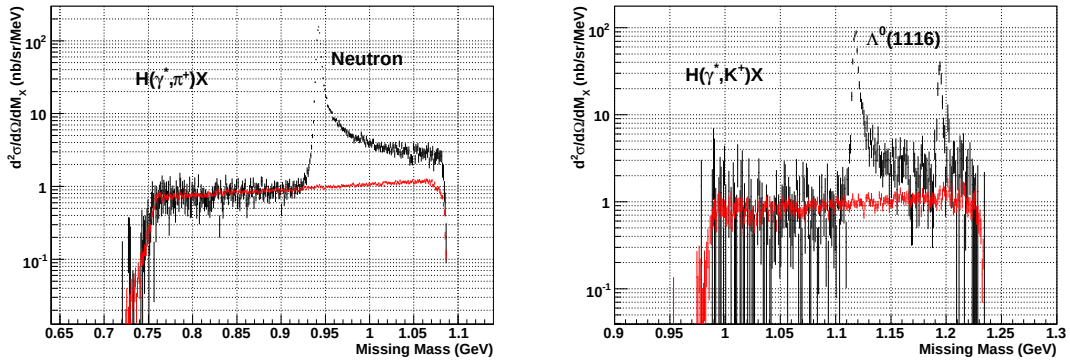

Figure 3-32: Accidental background subtraction.

3.9 Spectrum Combination

Once all cross section spectra from individual kinematics settings are extracted, they are summed together to span the entire missing mass ranges. The individual data sets overlapped to some extent, allowing for verification of the weighting and normalization. The complete list for kinematics settings can be found in Table 2.3. The $H(e,e'k^+)\Sigma_5^0$ and $H(e,e'\pi^+)N_5^0$ channels each have 8 settings and require such sum while the $H(e,e'k^-)\Theta^{++}$ channel has data from only one setting.

In an individual spectrum, the final cross section value in the i^{th} bin can be expressed as

$$S_i = (N_i - B_i) \cdot C_i, \tag{3.76}$$

where N_i is the original count for this bin, B_i is background level and C_i is the total correction factor applied to this bin. Since the background B_i contributes no error[4], the total error for this bin is

$$e_i = C_i \cdot \sqrt{N_i}. \tag{3.77}$$

To combine the values from different kinematics settings, the weight, w_{ij}, is taken into account according to the statistics, where the second subscript j is for the j^{th}

[4]See discussion in previous section.

histogram. The average with weight is

$$\overline{N_i} = \frac{\sum_j N_{ij} w_{ij}}{\sum_k w_{ik}} \tag{3.78}$$

and the average error is

$$\overline{e_i} = \sqrt{\sum_j (w_{ij} e_{ij} / \sum_k w_{ik})^2}. \tag{3.79}$$

Naively, $w_{ij} = 1/e_{ij}^2$, and equation (3.78) and (3.79) now become

$$\overline{N_i} = \frac{\sum_j N_{ij}/e_{ij}^2}{\sum_k 1/e_{ik}^2} \tag{3.80}$$

$$\overline{e_i} = 1/\sqrt{\sum_j 1/e_{ij}^2}. \tag{3.81}$$

This is the typical method to combine data with statistical errors, however there is a problem for low statistics, as was the cases in this experiment. Because the errors of individual bins are calculated by Poisson distribution, obviously the smaller the n_{ij} the greater the weight w_{ij}. The result is that the average has a trend to become smaller if more spectra are summed together.

It can be easily proved mathematically: the probablity of a measurement of a physics observable μ get n counts satisfies the Poission distribution

$$p(n, \mu) = \frac{\mu^n e^{-\mu}}{n!}, \tag{3.82}$$

and with $e = \sqrt{n}$ as the error of each measurement, the weighted average is expected to be

$$\langle n \rangle = \frac{\sum n/e^2}{\sum 1/e^2} = \frac{\sum_{i=1}^{\infty} \frac{i}{i} p(i, \mu)}{\sum_{i=1}^{\infty} \frac{1}{i} p(i, \mu)}. \tag{3.83}$$

The ratio of the average $\langle n \rangle$ to the actual average μ was calculated and plotted in Figure 3-33. Despite the range with extremely small μ ($\mu < 1.5$) the ratio is always smaller than 1 and approaches 1 as μ gets larger. This estimation may not accurately model the situation since the background subtraction is included in the actual analysis. Nevertheless it qualitatively shows the issue for low statistics cases.

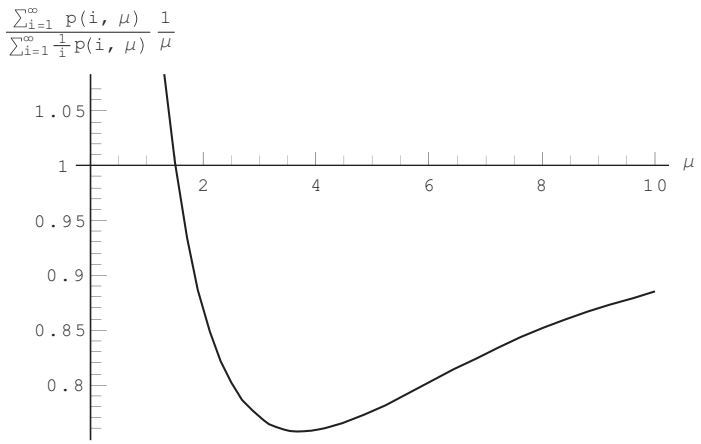

Figure 3-33: The ratio of weighted average to true value μ as a function of μ.

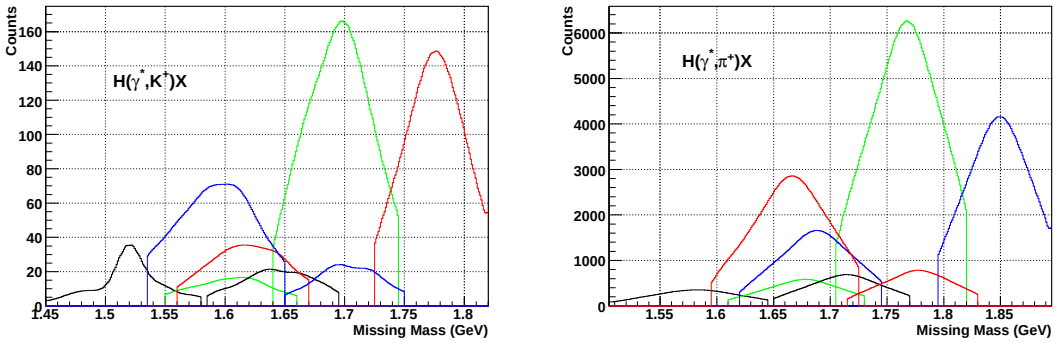

Figure 3-34: Static of K^+ and π^+ channels from different kinematics settings.

The statistics of different settings is shown in Figure 3-34, all the curves are smoothed to remove statistical fluctuation. As one can see, at some missing mass points, only few counts are expected, which will probably introduce about a 10% decrease in the average value if the naive adding method is used.

To solve this problem, another more stable variable needs to be used as weight rather than the error which is calculated from counts. Going back to the above example, the proper way to proceed is to average the measurements with no weight. In other words, the same weight is used globally because these measurements share the same expected value which means the same probably distribution for all measurements.

Therefore, the expected average value $\langle N_{ij} \rangle$ for each bin of individual spectrum is a better choice to calculate the weight. Furthermore, the averaged cross section values $\langle S_i \rangle$ is also used to replace $\langle N_{ij} \rangle$. The evolution of the weight is then

$$w_{ij} = \frac{1}{e_{ij}^2} = \frac{1}{C_{ij}^2 N_{ij}} = \frac{1}{C_{ij}(S_{ij} + B_{ij}C_{ij})} \rightarrow w_{ij} = \frac{1}{C_{ij}(\langle S_i \rangle + B_{ij}C_{ij})}. \tag{3.84}$$

The physics idea behind this method is simple: use the charge and all correction factors as weight to sum up the data. However the total correction factor C_{ij} of single bin is actually an average of correction factors coming from different momentum bins and such average inevitably has statistical fluctuation.

To get a set of stabilized C_{ij}, the following procedure was taken:

Step 1 Sum spectra using naive way, then fit the total spectrum with a smooth curve to get initial average value, $\langle S_i \rangle$, and calculate initial C_{ij}:

$$C_{ij} = \frac{\langle S_i \rangle}{\widetilde{N_i} - B_i}, \tag{3.85}$$

where $\widetilde{N_i}$ is the smoothed counts shown in Figure 3-34.

Step 2 Use the C_{ij} and $\langle S_i \rangle$ value from last step to do the sum, fit the total cross section spectrum again and get new sets of C_{ij} and $\langle S_i \rangle$.

Step 3 Repeat **Step 2** until C_{ij} and $\langle S_i \rangle$ stabilize.

Quantity	Effect on cross section		
	$H(e,e'K^+)X$	$H(e,e'\pi^+)X$	$H(e,e'K^-)X$
Beam charge	0.5%		
Target density	4.0%		
Electron angular acceptance	4.0%		
Hadron angular acceptance	4.0%		
PID	3.6%	2.2%	3.7%
Dead time	1.0%		
Total uncertainty	9.7%	9.3%	9.8%

Table 3.5: Systematic errors in experiment E04-012

After finalizing the combination of both Σ_5^0 and N_5^0 channels, all transitions between kinematics settings were found to be smooth, requiring no ad-hoc scaling, as shown in Figure 3-35 and 3-36.

The combined missing mass spectra obtained for all three reaction channels are shown in Figure 3-37.

3.10 Systematic uncertainty

The sources of systematic uncertainty in the measured cross section are listed in Table 3.5.

The two angular acceptances have errors which are strongly correlated due to the same method they are calculated. Therefore, the total error these two quantities giving is $4\% + 4\% = 8\%$. The rest of the individual uncertainties were added in quadrature to obtain the total uncertainties given in the last rows.

Since all these multiplicative factors were applied to the total cross sections, the total uncertainty affects the absolute cross section as whole.

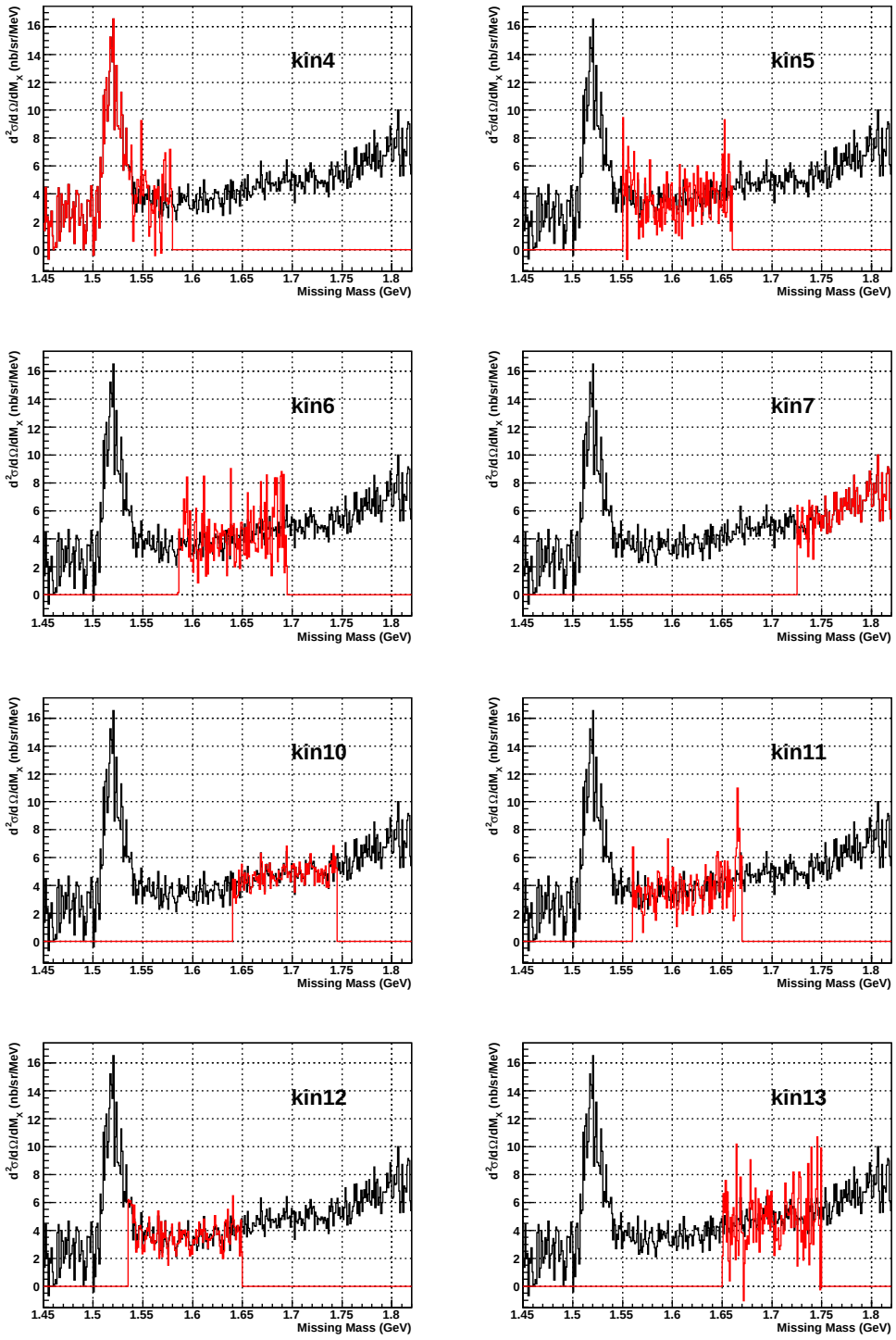

Figure 3-35: Individual cross section spectra of Σ_5^0 channel. The black background histogram shows the total averaged spectrum.

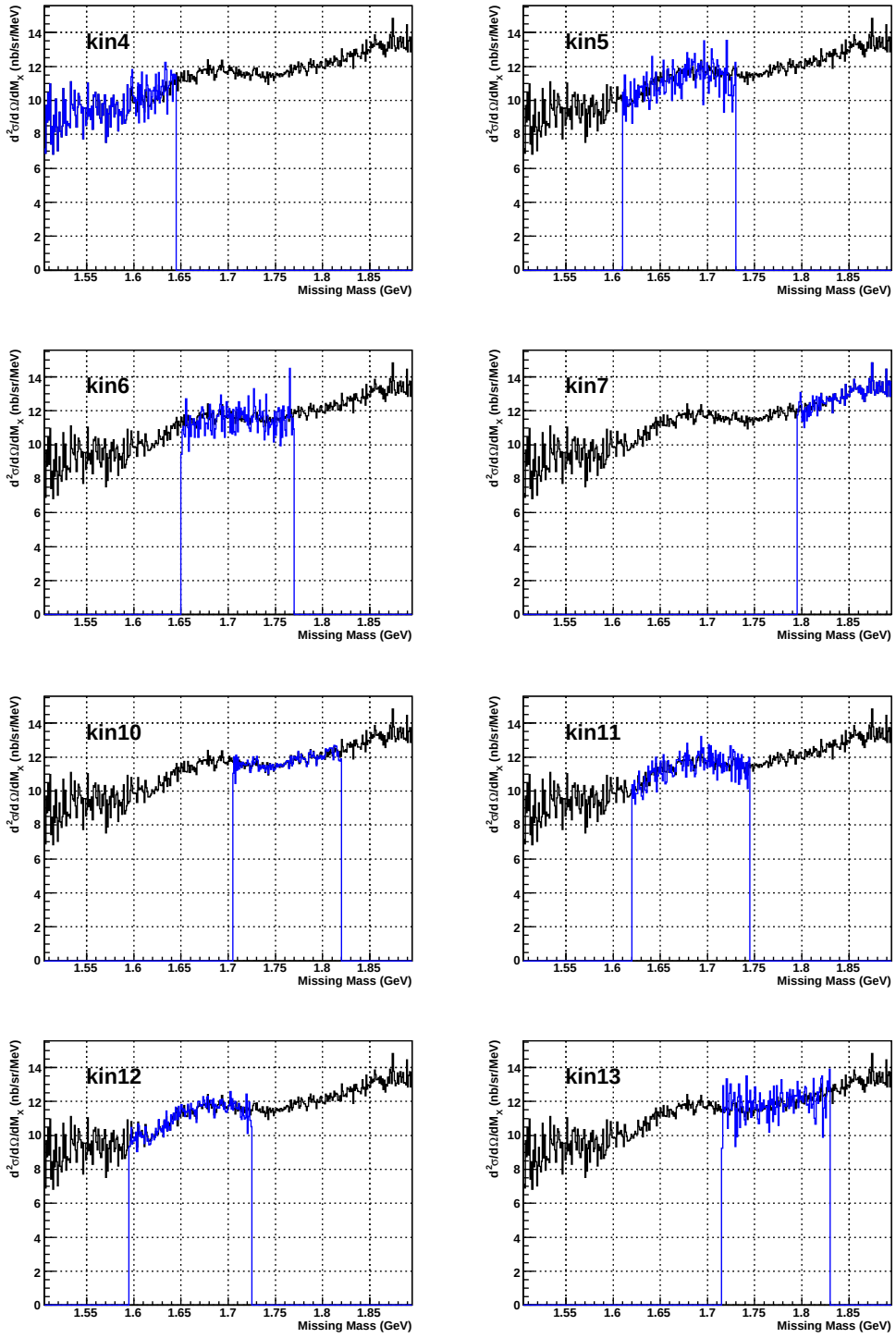

Figure 3-36: Individual cross section spectra of N_5^0 channel.

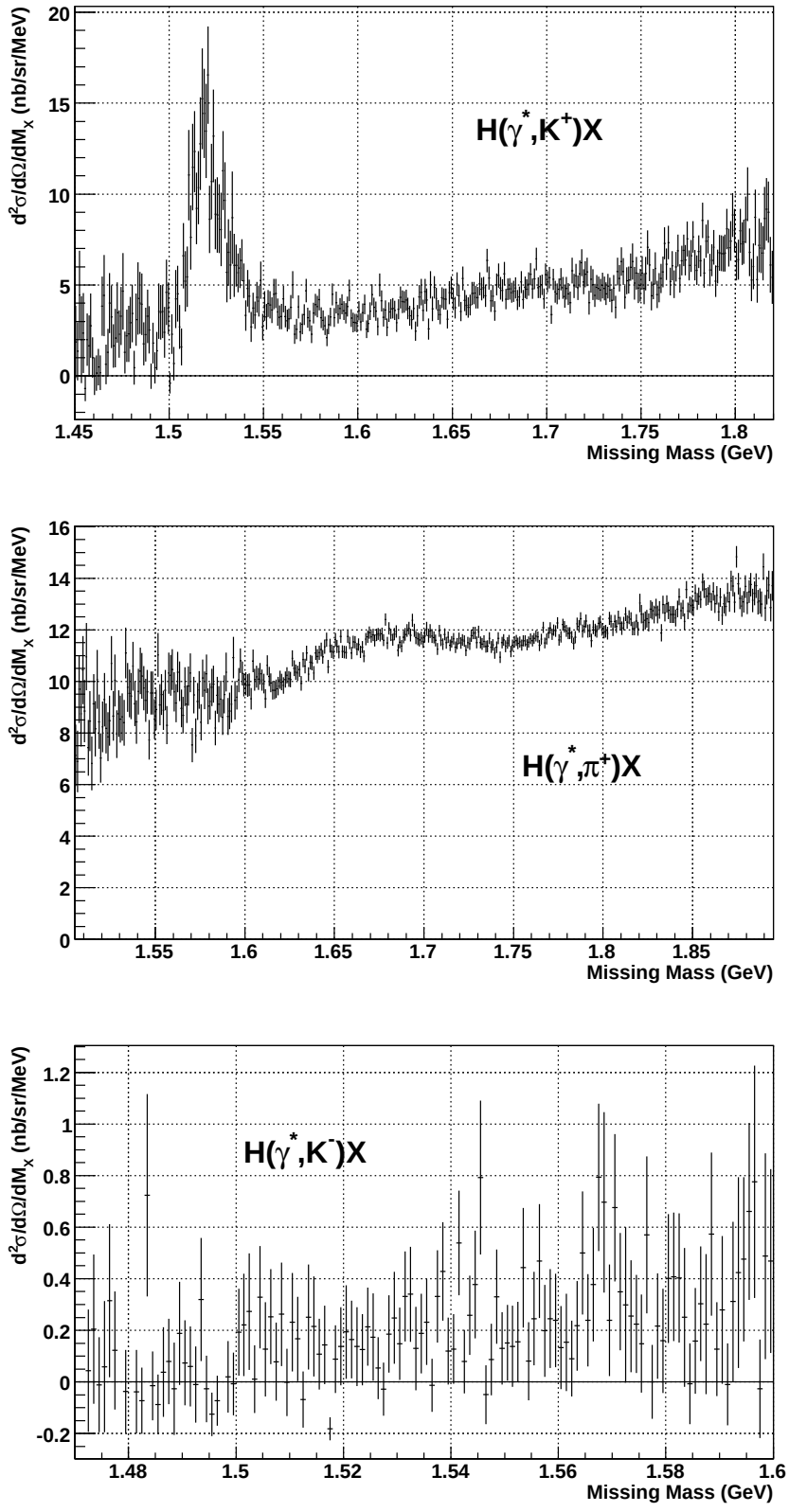

Figure 3-37: All three final cross section spectra.

Chapter 4

Spectrum Analysis and Conclusion

4.1 Missing Mass Calibration

Before searching for any signals in the total missing mass spectra, the quality of missing mass reconstruction was checked using productions of the following three particles, n, $\Lambda^0(1116)$ and $\Sigma^0(1193)$:

$$\gamma^* H \rightarrow \pi^+ n$$
$$\gamma^* H \rightarrow K^+ \Lambda^0(1116)$$
$$\gamma^* H \rightarrow K^+ \Sigma^0(1193).$$

The mass and resolution of all three particles were measured and compared to the values from particle data group (PDG) [94]. The results are listed in Table 4.1 and some quantities are discussed in Section 4.1.1.

Particle	Kin	Mass (GeV/c^2)	PDG (GeV/c^2)	Shift (MeV/c^2)	Resolution (MeV/c^2)	P_{0L} (GeV/c)	P_{0R} (GeV/c)
Neutron	1	942.62 ± 0.13	939.57	3.05	1.86 ± 0.03	2.5	2.5
$\Lambda^0(1116)$	3	1117.83 ± 0.56	1115.68	2.15	1.74 ± 0.06	2.2	2.5
$\Sigma^0(1193)$	3	1194.30 ± 1.00	1192.64	1.66	1.57 ± 0.14	2.2	2.5

Table 4.1: Missing Mass Calibration Results

4.1.1 Missing Mass Resolution

According to equation (3.73), the missing mass resolution is given by

$$\sigma_M^2 = \sigma_{P_L}^2 + \sigma_{P_R}^2 + \sigma_{E_{beam}}^2. \tag{4.1}$$

And for each spectrometer, the momentum resolution is proportional to its central momentum setting:

$$\sigma_P = P_0 \cdot \sigma_\delta, \tag{4.2}$$

where P_0 is the central momentum and σ_δ is the relative momentum resolution which is a constant to all momentum settings.

During the experiment, the beam energy had a spread about 5×10^{-5} and this gave $\sigma_{E_{beam}} = 0.25$ MeV for 5.0 GeV beam.

By using the resolutions obtained from all three particles, it's straightforward to get the σ_δ for each spectrometer:

$$\sigma_{\delta_L} = (6.08 \pm 1.28) \times 10^{-4} \tag{4.3}$$

$$\sigma_{\delta_R} = (4.16 \pm 1.77) \times 10^{-4}. \tag{4.4}$$

For the production momentum settings, both spectrometers were set at around 2 GeV/c and the expected missing mass resolution is

$$\sigma_M = 1.50 \pm 0.02 \text{ MeV}/c^2. \tag{4.5}$$

4.1.2 Absolute Missing Mass Uncertainty

The first two plots in Figure 4-1 show the obtained hadron missing mass spectra and the third one is the deviation of these particles' measured masses to the known PDG values. The error bars in this plot not only include the statistical errors which are quoted in Table 4.1 but also the beam energy spread $\sigma_{E_{beam}}$.

As one can see, the reconstructed missing mass is shifted by a couple of MeV/c^2

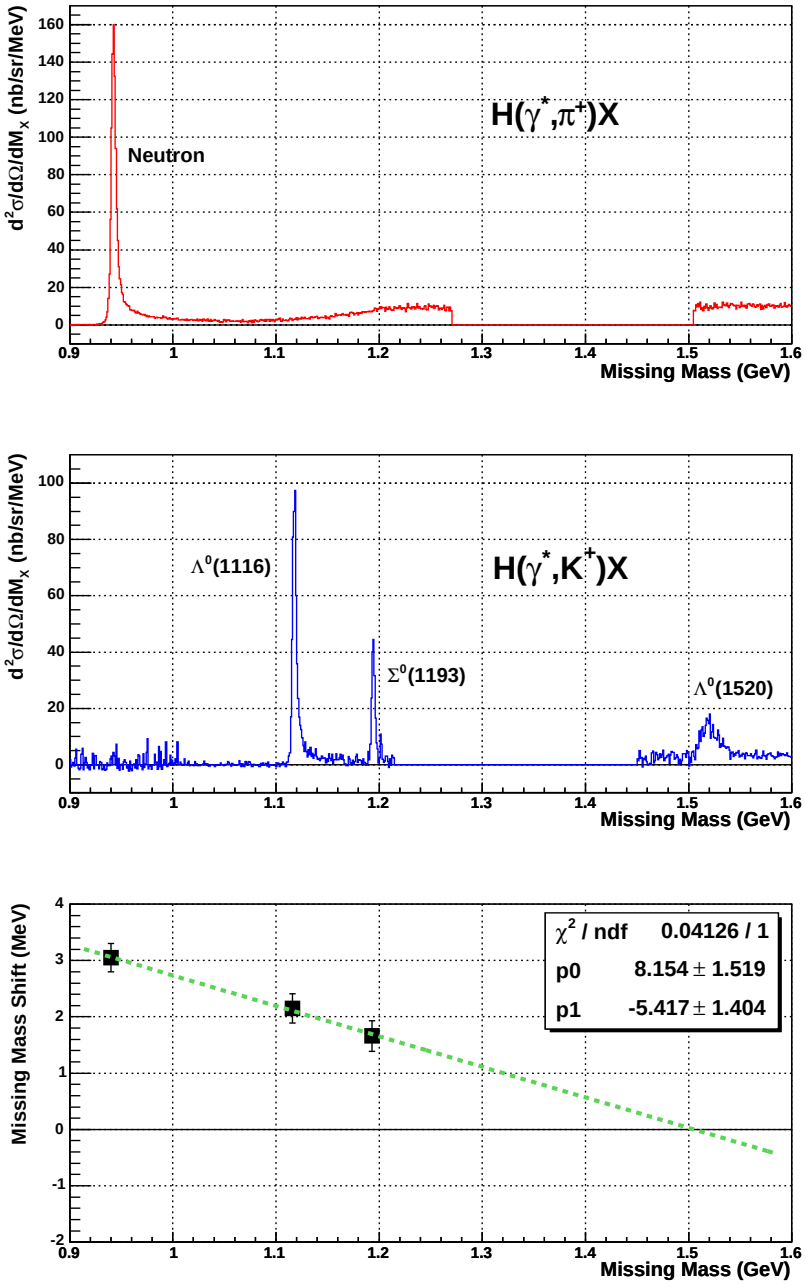

Figure 4-1: The missing mass measurement of neutron, $\Lambda^0(1116)$ and $\Sigma^0(1193)$, and the shifts from PDG values.

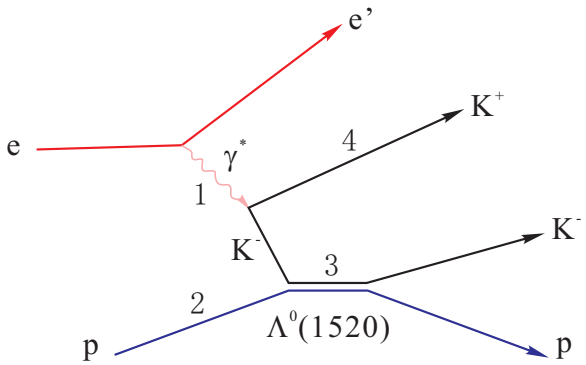

Figure 4-2: The diagram for $\Lambda^0(1520)$ electro-production. The numbers marked in the plot are used in following cross section formulas.

from the actual value. We could not fix this shift due to a lack of calibration data. There are at least 4 optics elements that need to be adjusted, 2 for each spectrometer: shift and scale. However, data from only three peaks does not give enough freedom to do the work.

It's also noticed that the deviation in missing mass shows trends to decrease as missing mass increases. As shown in the bottom plot of figure 4-1, the shifts match a linear function very well and the projected missing mass shift in the region of interests (1.5∼1.8 GeV) is very small. Actually, the central position of resonance $\Lambda(1520)$ obtained from next section (1519.9 MeV/c^2)[1] agreed with the PDG value (1519.5 MeV/c^2) quite well. Thus it's safe to say that the absolute mass uncertainty is less than 3 MeV/c^2 in the search region.

4.2 Properties of $\Lambda(1520)$ in Photoproduction

The production of $\Lambda^0(1520)$ is generally used as a comparison to pentaquark states [3][6], especially the $\Theta^+(1540)$, because of their similar mass and production mechanism.

On the other hand, the high resolution and moderate statistics of this experiment provides an opportunity to precisely measure the width of this resonance.

Because the $\Lambda^0(1520)$ has a mass very close to its NK threshold, it's suggested

[1]The reason why this position was not used in the missing mass calibration is due to the fact that $\Lambda(1520)$ has a relatively broad width (∼15 MeV/c^2) which is much larger than the shift.

by reference [95] that the width of $\Lambda^0(1520)$ production is affected by the centrifugal barrier. For its orbital angular momentum $L = 2$ and spin $J = 3/2$, the width Γ has the following presentation instead of it's native value Γ_0:

$$\Gamma(m_3) = \Gamma_0(\frac{m_3 - m_K - m_N}{M_\Lambda - m_K - m_N})^{5/2}, \tag{4.6}$$

while the matrix element still has the Breit-Wigner form:

$$|\mathscr{M}|^2 = \frac{\Gamma}{2\pi[(m_3 - M_\Lambda)^2 + (\Gamma/2)^2]}. \tag{4.7}$$

For the two body reaction, the differential cross section is written as [96]

$$d\sigma = \frac{(2\pi)^4|\mathscr{M}|^2}{4\sqrt{(\vec{p}_1 \cdot \vec{p}_2)^2 - m_1^2 m_2^2}} \times d\Phi(p_1, p_2; p_3, p_4). \tag{4.8}$$

In the center-of-mass frame

$$\sqrt{(\vec{p}_1 \cdot \vec{p}_2)^2 - m_1^2 m_2^2} = p_1\sqrt{s}, \tag{4.9}$$

and the two body final state phase space is

$$d\Phi(p_1, p_2; p_3, p_4) = \frac{d^3p_3}{E_3E_4} = \frac{|\vec{p}_3|^2 dp d\Omega}{E_3E_4}. \tag{4.10}$$

Now the cross-section is given by

$$\frac{d^2\sigma}{d\Omega dm_3} = \frac{(2\pi)^4|\mathscr{M}|^2|\vec{p}_3|^2}{4p_1E_3E_4\sqrt{s}}\frac{dp_3}{dm_3}. \tag{4.11}$$

From

$$|\vec{p}_3| = |\vec{p}_4| = \frac{[(s - (m_3 + m_4)^2)(s - (m_3 - m_4)^2)]^{1/2}}{2\sqrt{s}}, \tag{4.12}$$

it is straightforward to derive

$$|\frac{dp_3}{dm_3}| = \frac{m_3E_4}{p_3\sqrt{s}}. \tag{4.13}$$

Thus, equation (4.11) is finalized as

$$\frac{d^2\sigma}{d\Omega dm_3} = \frac{(2\pi)^4 |\mathscr{M}|^2 p_3 m_3}{2p_1\sqrt{s}(s + m_3^2 - m_4^2)}. \tag{4.14}$$

To fit the experimental spectrum, equation (4.14) is convoluted with a Gaussian function with $\sigma = 1.5$ MeV/c^2, which represents the missing mass resolution. Within the fitting area 1.45 - 1.60 GeV/c^2, the background includes [97][98]:

- the 3 body final state phase space $\gamma^* p \to K^+ K^- p$,
- the tail from a sub-threshold resonance $\Lambda(1405)$, and
- ϕ meson production[2] $\gamma^* p \to \phi p \to K^+ K^- p$.

The simulation shows that the *phi* production background has fairly flat shapes in the region and up to second order polynomials are good enough to describe it.

Therefore in the fit, the background is actually composed by a 3 body decay phase space, the tail of $\Lambda^0(1405)$ and a polynomial with order lower than 3 describing the ϕ production. With the order of polynomial n changing from 0 to 2, the resulting $\Lambda^0(1520)$ cross section varies less than 1% which is far smaller than its statistical error, therefore a ploynomial with $n = 0$ is used for the final fit.

On the other hand, due to the low statistics in some mass regions, the Log-likelihood method was used, and the details of such fit will be described in the following Section 4.3.2.

As shown in Figure 4-3, the fit gives

$$M_{\Lambda(1520)} = 1519.9 \pm 0.6 \text{ MeV}/c^2 \tag{4.15}$$

$$\Gamma_0 = 16.49 \pm 1.71 \text{ MeV}/c^2 \tag{4.16}$$

$$\frac{d\sigma}{d\Omega} = 356 \pm 25_{stat.} \pm 35_{sys.} \text{ nb/sr}. \tag{4.17}$$

In this reaction, the average four-momentum virtual photon transfer is $\langle Q^2 \rangle \approx 0.1$ (GeV/c)^2 and the average CM photon energy is $\langle E_\gamma^{\rm CM} \approx 1.1$ GeV$\rangle$. The CM K^+ production

[2]The two major mesons allowed by the kinematics are $f_2(1270)$ and $a_2(1320)$.

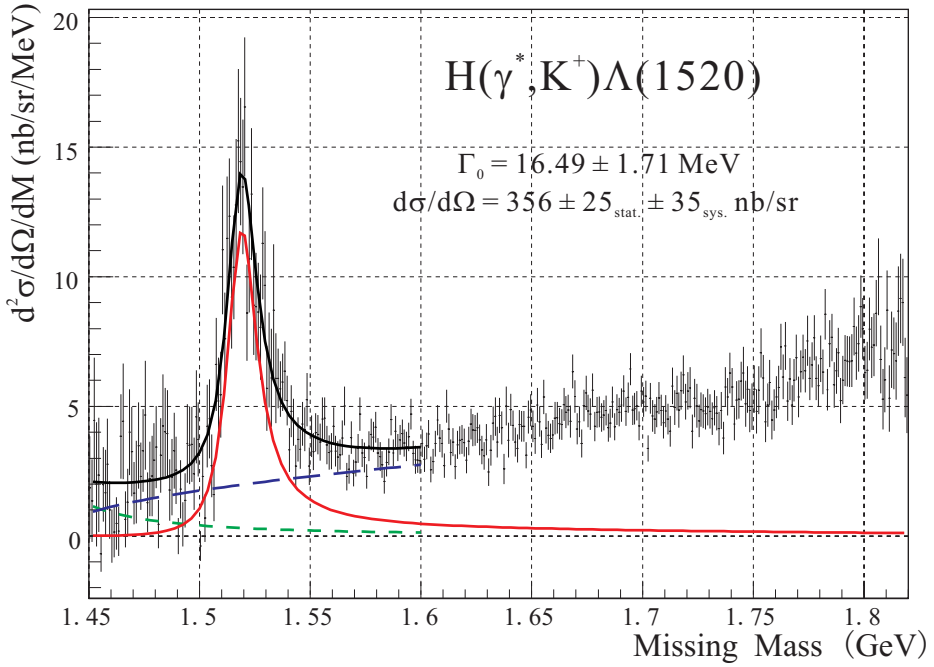

Figure 4-3: Photoproduction cross section of $\Lambda^0(1520)$ with $Q^2 \sim 0.1 \approx (\mathrm{GeV}/c)^2$, $E_\gamma^{\mathrm{CM}} \approx 1.1$ GeV and $\theta_{\gamma^* K}^{\mathrm{CM}} \approx 8.5^\circ \pm 2.9^\circ$. The black line shows the fit curve, the blue long dashed line shows the 3 body decay background, the green short dashed line shows the tail from sub-threshold resonance $\Lambda^0(1405)$ and the red line shows the net production of $\Lambda^0(1520)$.

angle is $5.6^\circ < \theta^{\rm CM}_{\gamma^* K} < 11.4^\circ$ and the angular acceptance is $\Delta^{\rm CM}_{\gamma^* K} \approx 38$ msr.

For comparison, the PDG width for $\Lambda^0(1520)$ is 15.6 ± 1.0 MeV/c^2 and most of the high precision data came from either direct experiments using bubble chambers or indirect particial wave analysis [94]. Normally, high energy spectrometers don't have enough resolution to do the direct measurement. With the help of Hall A HRSs the result of our experiment shows an exciting accuracy and agrees with global data very well.

4.3 Search For Narrow Resonances

As shown in Figure 3-37, all three spectra show no significant signals in the whole missing mass range:

$H(e,e'K^+)\Sigma^0_5$	1550 - 1810 MeV/c^2,
$H(e,e'\pi^+)N^0_5$	1610 - 1880 MeV/c^2, and
$H(e,e'K^-)\Theta^{++}$	1480 - 1590 MeV/c^2.

Therefore, the goal of the following analysis is to determine the the range in the cross section of a hypothetical narrow resonance that would be compatible with the missing mass spectrum at 90% confidence, without any *priori* assumptions of a non-zero resonance cross section. To accomplish this, the Feldman and Cousins [99] approach was adopted.

4.3.1 Feldman-Cousins Approach

Classical confidence intervals are the traditional way in which physicists report errors on results of experiments. The true confidence intervals can be obtained using the original (defining) construction of Neyman [100]. However, considerable dissatisfaction may occur when the result is an unphysical or an empty set interval. Such a problem often happens for experiments with small signals, as in our case. On the other hand, when considering the physical boundary for small signals, manually selecting the type of confidence interval based on the experimental data inevitably introduces bias and leads to doubtable results.

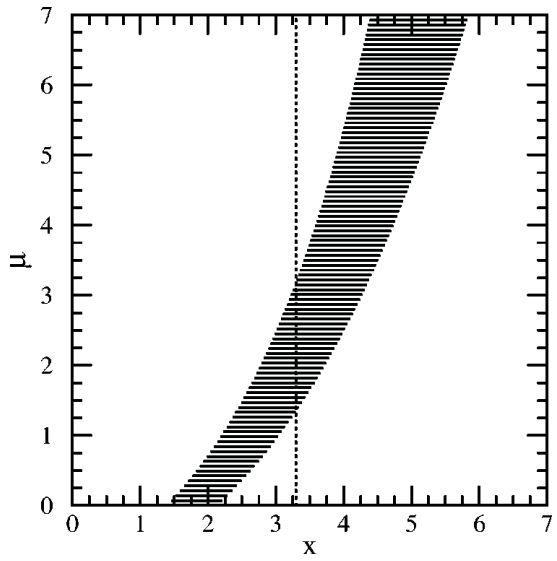

Figure 4-4: A generic confidence interval construction.

In contrast, the Feldman-Cousins unified set of confidence intervals satisfies (by construction) the classical criterion of frequentest coverage of the unknown true value, which means it automatically generates proper types of confidence intervals without bias. This method was first used in neutrino oscillation searches and we managed to generalize this approach for our pentaquark search.

Classical Confidence Intervals

Suppose that we wish to make an inference about a parameter μ whose true value is unknown. Assume that we do this by making a single measurement of an observable x such that the probability density function (pdf) for obtaining the value x depends on the unknown parameter μ in a known way: we call this pdf $P(x|\mu)$. A confidence interval $[\mu_1, \mu_2]$ corresponding to a confidence level α is a member of a set, such that the set has the property that

$$P(\mu \in [\mu_1, \mu_2]|x) = 1 - \alpha. \tag{4.18}$$

The traditional way to construction a classical confidence interval is illustrated by Figure 4-4.

For each value of μ, one examines $P(x|\mu)$ along the horizontal line through μ. One selects an interval $[x_1, x_2]$ which is a subset of this line such that

$$P(x \in [x_1, x_2]|\mu) = 1 - \alpha. \tag{4.19}$$

Such intervals are drawn as horizontal line segments in Figure 4-4, at representative values of μ. For an experiment to measure x and obtain the value x_0, one draws a vertical line (shown as a dashed line through x_0 on the horizontal axis). The confidence interval is the union of all values of μ for which the corresponding acceptance interval is intercepted by the vertical line, and typically this is a simply connected interval $[\mu_1, \mu_2]$.

The type of interval $[x_1, x_2]$ as the "acceptance region" for such analysis must be selected. For "central confidence intervals" one may choose

$$P(x < x_1|\mu) = P(x > x_2|\mu) = \alpha/2, \tag{4.20}$$

and for "upper confidence limits" the choice is

$$P(x < x_1|\mu) = \alpha. \tag{4.21}$$

Figure 4-5 shows these two different types of confidence intervals when the observable x is simply the measured value of μ in an experiment with a Gaussian resolution function with known fixed rms deviation σ. And μ is constrained to be non-negative.

If a physicist select the types of interval based on the result of x, let's say upper limit for $x_0 < 3\sigma$ and central interval for x_0 greater than 3σ. We call this a "flip-flopping" policy and the effect of such policy is shown in Figure 4-6. Such confidence intervals for "90%" C.L. are obviously not valid, since they sometimes cover the true value at a frequency less than the stated confidence level. For $1.36 < \mu < 4.28$, the coverage is only 85%.

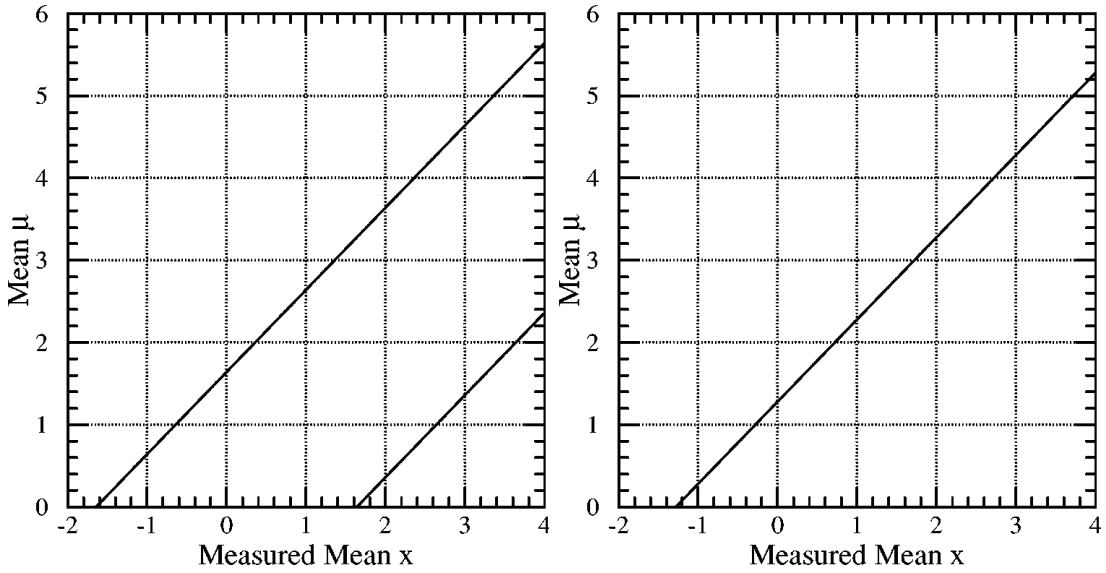

Figure 4-5: Left: standard confidence interval for 90% C.L. central confidence intervals. Right: standard confidence interval for 90% C.L. upper limits. The second line for the upper limits case is at $x = +\infty$ and all plots are in the units of the rms deviation (σ).

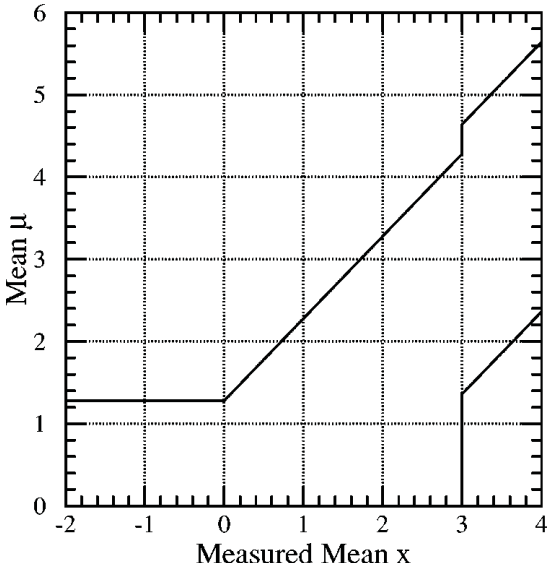

Figure 4-6: Plot of confidence interval used for 90% C.L. quoted by flip-flopping physicist.

Ordering Principle

The flip-flopping problem is solved in Feldman-Cousins method by its "ordering principle". In this approach what one considers is not simply x but a ratio of probabilities and this new quantity is defined by

$$R(x,\mu) = \frac{P(x|\mu)}{P(x|\mu_{best})}, \tag{4.22}$$

where μ_{best} is the set of parameters that maximize $P(x|\mu)$ and it is required to be physically allowed. Obviously one has $0 \leq R \leq 1$ and the R is getting larger as the probability increases.

In contrast to formula (4.19), the acceptance region for μ now comes from the ordering of μ,

$$P(R(x,\mu) > R_c|\mu) = 1 - \alpha, \tag{4.23}$$

where the probability of x satisfies the pdf $P(x|\mu)$ and the cut R_c on R is derived from such condition. The set of x satisfying this equation gives the acceptance. Typically it is still a connected interval $[x_1, x_2]$. Since the R is only calculated in the physical region, the probability in equation (4.23) is the real probability of the physical world. Because of the ordering of R, the unique cut R_c automatically gives the proper type of confidence interval with no doubt.

Returning to the previously discussed problem about the confidence interval for a Gaussian distribution, with the Feldman-Cousins approach, the 90% confidence interval is shown in Figure 4-7. It is instructive to compare it with Figure 4-6. At large x, the confidence intervals $[\mu_1, \mu_2]$ are the same in both plots, since that is far away from the constraining boundary. Below $x = 1.28$, the lower end point of the new confidence intervals is zero, so that there is automatically a transition from two-sided confidence intervals to an upper confidence limit given by μ_2.

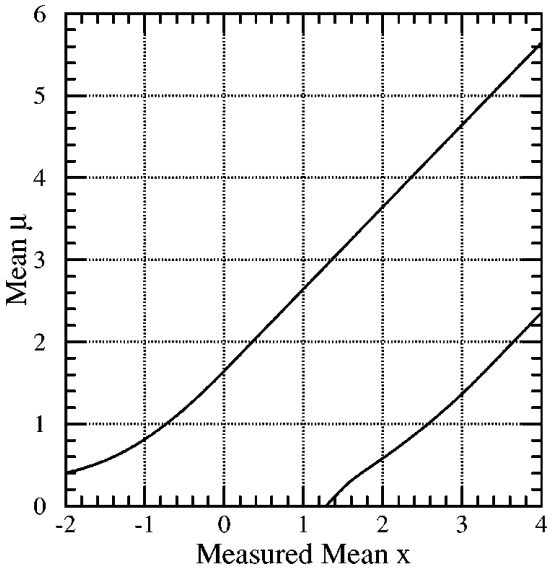

Figure 4-7: Plot of 90% confidence interval for the mean of a Gaussian, constrained to be non-negative. This gives a much more reliable 90% inaterval compared to Figure 4-6.

4.3.2 Application To Pentaquark Search

For the pentaquark search, we plan to perform spectrum scans throughout each missing mass spectrum in 1 MeV/c^2 steps for several hypothesis widths of 0.5, 2.0, 5.0 and 10.0 MeV/c^2 and derive the 90% confidence interval for the cross sections of possible resonances.

Resonance Shape

The resonance shape used in following fit is a Breit-Wigner with width Γ convoluted with a 1.5 MeV/c^2 wide Gaussian which represents the instrumental resolution.

Log-Likelihood Fit

Due to the low statistics in some missing mass regions, the traditional χ^2[101] fit on the total spectra is no longer reliable. Therefore in this analysis, the fit uses maximum likelihood techniques [99][102]. What is actually done is minimizing the quantity called the log-likelihood. For Poisson distributions, the total log-likelihood

for a multiple data set is

$$-2ln\mathcal{L} = 2\sum_j \sum_i (s_{ij} + b_{ij} - n_{ij} + n_{ij} ln(\frac{n_{ij}}{s_{ij} - b_{ij}})), \tag{4.24}$$

where the subscript i is for the i^{th} bin involved in the fit, subscript j means the data from j^{th} momentum settings, s is the signal strength in counts, b is the background (non-narrow-resonance) level in counts and n is the actual counts from experimental data. The individual s and b are calculated from the cross section values by applying correction factors C_{ij} and the accidental background $B_{ij}^{\rm acc}$ determined in section 3.9:

$$s_{ij} = s_i^{\rm CS}/C_{ij} \tag{4.25}$$

$$b_{ij} = b_i^{\rm CS}/C_{ij} + B_{ij}^{\rm acc}. \tag{4.26}$$

And the total cross section for the signal is

$$\sigma = \sum_i s^{\rm CS}. \tag{4.27}$$

The best estimation of background and signal is obtained by minimizing the log-likelihood.

Measurement of Background Level

In the calculation of log-likelihood, both background and signal are free parameters to fit. Since the final goal is to arrive at the confidence interval of the signal strength, the background level needs to be determined first.

Actually, the background level presents a slight difficulty with applying Feldman-Cousins approach to most situations (including ours). Technically, the Feldman-Cousins approach assumes that the level of the background is known absolutely, either from Monte Carlo (as Feldman and Cousins assume for their neutrino oscillation example) or from measurements. We, and most places that use Feldman-Cousins, fit the background.

In the language used in discussing this problem the level of background is called a

"nuisance" parameter and there is much literature about this. The "correct" way to handle the nuisance parameters is given in reference [103]. This article suggests that the Feldman-Cousins approach will give "over coverage" in this case, and we could set a tighter bound if we treated the nuisance parameter (i.e. background) correctly. Rolke, et al. provide routines for this, but they seem to not be directly applicable to our situation.

Feldman and Cousins have also studied this issue, see reference [104] and Feldman's presentation [105]. In Feldman's presentation, his essential conclusion is that there is "over coverage" unless you are in the situation of very small background, which may not apply in our case. So the conclusion is that we are justified in presenting the Feldman-Cousins approach and not switching to the Rolke approach.

At the point of a given missing mass, M, the level of background is obtained by fitting the 20 MeV/c^2 wide sidebands above and below the region containing 90% of a hypothesized peak at M with width Γ. The side band near the spectrum's edge is reduced to a minimum of 5 MeV/c^2 while the total coverage of both sidebands is kept 40 MeV/c^2.

The function used in the background fit is constructed from the smooth background shape B^0 obtained earlier in the spectrum combination,

$$b^{\mathrm{CS}}(M) = c_0 \cdot B^0(M) + c_1 + c_2 \cdot M + o(M^2), \tag{4.28}$$

where c_i are free parameters for fit. The maximum order of M is determined based on the statistics and the shape of channels. The order should be kept as low as possible but not lose the ability to describe the actual shapes. As a result Σ_5^0 uses up to zeroth order while N_5^0 and Θ^{++} use first order.

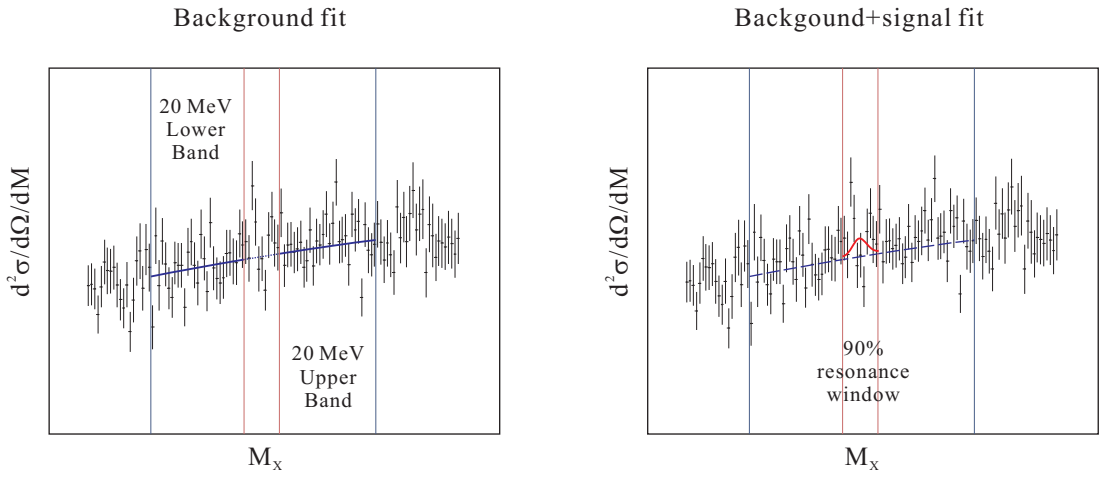

Figure 4-8: The background and signal fits of the missing mass spectrum.

Monte Carlo and 90% Confidence Interval

Once the background level is fixed, the only free parameter in the fit is the cross section of the Breit-Wigner resonance:

$$\mu = \sigma. \tag{4.29}$$

Then the σ_{best} is obtained by fitting the spectrum within the 90% resonance window which covers 90% of the total cross section of the resonance, as shown in Figure 4-8.

Since the likelihood is the probability of getting the spectrum from a signal with cross section σ, the approach is equivalent to using the difference in log-likelihood between σ and σ_{best} instead of R, the ratio of probabilities, i.e.,

$$\begin{aligned} R'(\sigma) &= \Delta ln\mathcal{L}(\sigma) = -2ln\mathcal{L}(\sigma) - (-2ln\mathcal{L}(\sigma_{best})) \\ &= -2ln(R) = 2\sum_j \sum_i (s_{ij} - s_{ij}^{best} + n_{ij} ln(\frac{s_{ij}^{best} + b_{ij}}{s_{ij} - b_{ij}})). \end{aligned} \tag{4.30}$$

With only physically allowed non-negative cross sections σ, one has $0 \leq R'$ and $R'(\sigma_{beset}) = 0$ for best fit.

Figure 4-9 shows how to arrive at the 90% confidence interval using the test variable R'.

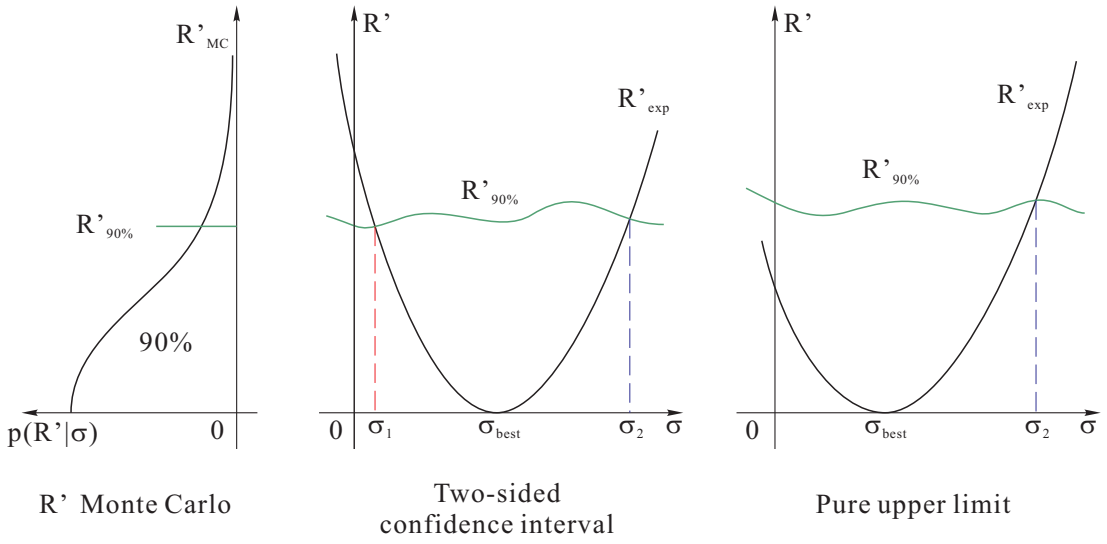

Figure 4-9: Extraction of 90% confidence interval for cross section. The left plot shows the distribution of R' and the $R'_{90\%}$ obtained from Monte Carlo "experiments". the collection of $R'_{90\%}$ are the green curves in the next two plots. The μ with experimental R' less than $R'_{90\%}$ is accepted in the 90% confidence interval. The two types of intervals are determined automatically.

For each value of σ, the 90% cut for R' needs to be determined first. The equation (4.23) now becomes

$$P(R' < R'_{90\%}|\sigma) = 90\%. \tag{4.31}$$

To find out such $R'_{90\%}$ for a cross section σ, many Monte Carlo "experiments" were performed. Missing mass spectra for each spectrometer settings were randomly populated with total statistics equal to that of the actual data. The spectral shape was based on the smooth background shape with a hypothetical resonance of cross section σ and width Γ added at mass M. From these Monte Carlo "experiments", $R'_{\rm MC} = \Delta ln\mathcal{L}_{\rm MC}$ was determined. The distribution of $R'_{\rm MC}$ from the Monte Carlo "experiments" was examined to determine $R'_{90\%}$ such that 90% of the Monte Carlo simulations had $R' < R'_{90\%}$. Due to using the Monte Carlo method, the $R'_{90\%}$ can only be obtained for discreet σ values, and in this analysis, the σ was selected in steps of 0.5 nb/sr. The quality of the Monte Carlo was checked by comparing the log-likelihood fit of pure background simulations, $\sigma = 0$, with the experimental data as shown in Figure 4-10.

Γ(MeV/c^2)	0.5	2.0	5.0	10.0	Mass (MeV/c^2)
Σ_5^0 (nb/sr)	10.0 (2.8%)	11.0 (3.1%)	13.0 (3.7%)	17.5 (4.9%)	1550 - 1810
N_5^0 (nb/sr)	4.5 (1.3%)	5.5 (1.5%)	6.0 (1.7%)	10.5 (2.9%)	1610 - 1880
Θ^{++} (nb/sr)	3.0 (0.8%)	3.5 (1.0%)	3.5 (1.0%)	4.0 (1.1%)	1480 - 1590

Table 4.2: Result of narrow resonance scan. For each of the resonances investigated, this table lists the largest upper limit photoproduction cross section in nb/sr and relative to the measured $\Lambda^0(1520)$ of $356 \pm 25_{stat.} \pm 35_{sys.}$ nb/sr for resonance widths of Γ=0.5,2.0,5.0 and 10.0 MeV/c^2.

Then the $R'(\sigma)_{exp}$ was calculated for all σ grid points using experimental data. If a σ satisfies $R'(\sigma)_{exp} < R'_{90\%}(\sigma)$ then this σ is within the 90% acceptance. And the collection of these σ values give the 90% confidence interval.

90% Sensitivity Level

In addition, the sensitivity level at 90% suggested by Feldman and Cousins was also calculated to help interpret the result. It shows the 90% probability of background fluctuations and the background has only a chance of 10% for creating larger fluctuation than this level:

$$P(\sigma_{best} < \sigma^{sen}_{90\%} | \sigma = 0) = 90\%. \tag{4.32}$$

Basically, it's indicating the sensitivity or the ability of identifying potential signals of the experiment.

4.3.3 Results And Conclusion

The upper limit, lower limit and statistical sensitivity curves are shown in Figures 4-11, 4-12 and 4-13 for the Γ =0.5, 2.0, 5.0 and 10.0 MeV/c^2 cases. The maximum upper limits listed in Table 4.2 are expressed, for each resonance in nb/sr and as a fraction of the $\Lambda^0(1520)$ cross section.

As can be seen in Figures 4-11, 4-12 and 4-13 most of the 90% confidence region shows only upper limits and the upper limit curves oscillate about the statistical sensitivity curves. And the oscillating behavior of upper limits is expected for pure background situation since the 90% upper limit can be treated as an experimental

measurment of the 90% background fluctuation level in that case. Where the lower limit curves are different from zero, they are always below the sensitivity curves implying that non of the lower limits can be distinguished from a statistical fluctuation.

There are several known or suspected resonances in this mass region, in particular several 3 or 4-star[3] Λ, Σ, Δ and N states in the $\gamma^* p \to K^+ X$ and $\gamma^* p \to \pi^+ X$ channels [94]. Most are too wide (> 50 MeV/c^2) to be visible in this experiment (unless they have a *substantial* cross section) and have only been seen in partial-wave analysis or both. Taken together, they add up to a relatively smooth background.

In conclusion, a high resolution search for the Σ_5^0, N_5^0 and Θ^{++} has been completed using the Jefferson Lab Hall A HRS spectrometers. This search had an instrumental resolution of $\sigma_{\text{instr.}} = 1.5$ MeV/c^2. No statistically significant narrow ($\Gamma \leq 10$ MeV/c^2) structures were observed in any of the three reaction channels. Upper limits of the photoproduction cross section for these states were found to be $< 5\%$ of the $\Lambda^0(1520)$ photoproduction cross section for $\Gamma \leq 10$ MeV/c^2 at 90% confidence level.

[3]According to PDG [94], 3 star means that the existence of a resonance ranges from very likely to certain, but further confirmation is desirable and/or quantum numbers, branching fractions, etc. are not well determined. 4-star means that the existence of a resonance is certain and properties are at least fairly well explored.

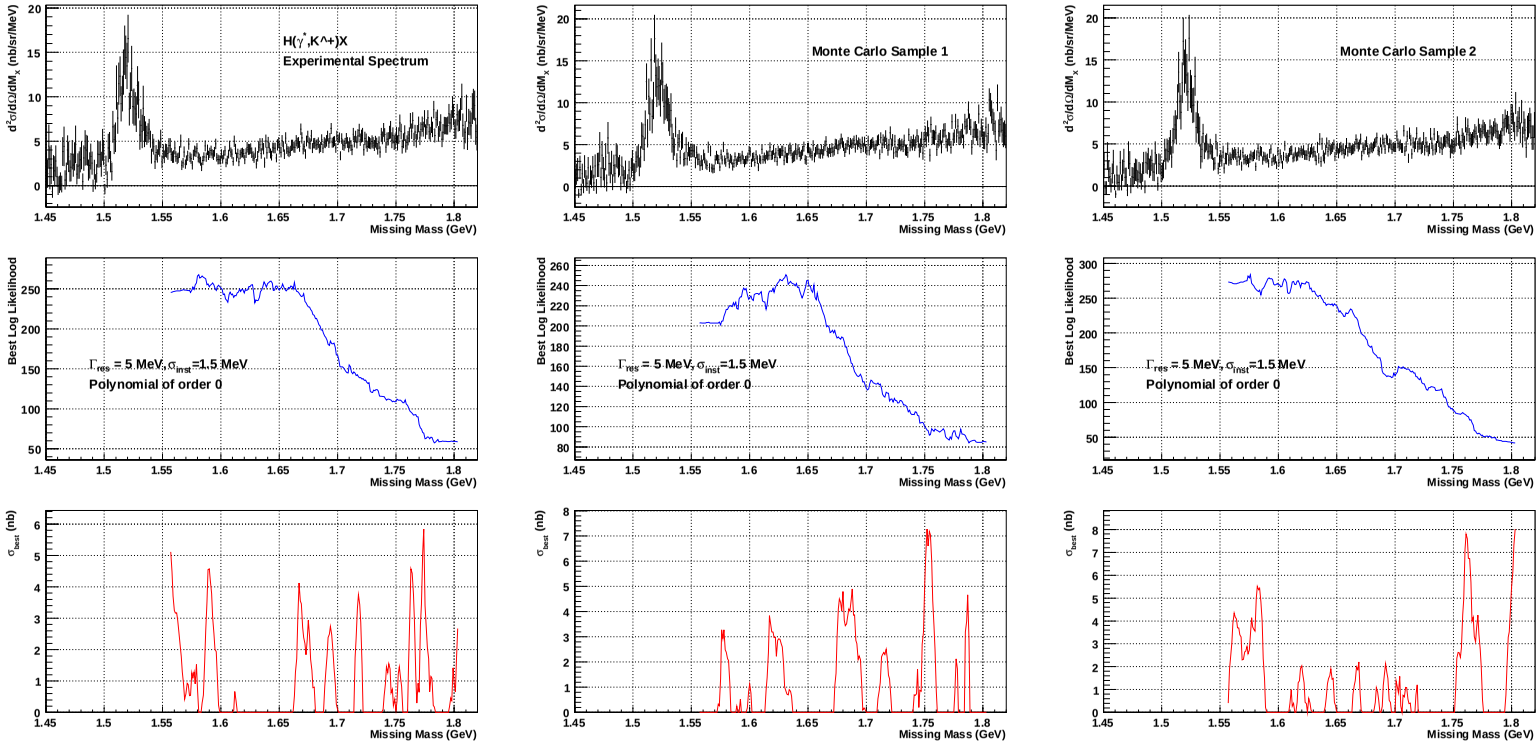

Figure 4-10: The comparison of Monte Carlo spectra with experimental spectrum. The plots in second row are the minimum log likelihood and all three curves display similar behavior and consistent values. The bottom plots are integrated cross section σ_{best} and once again these three spectra give similar grass-like pattern with similar frequency and amplitude.

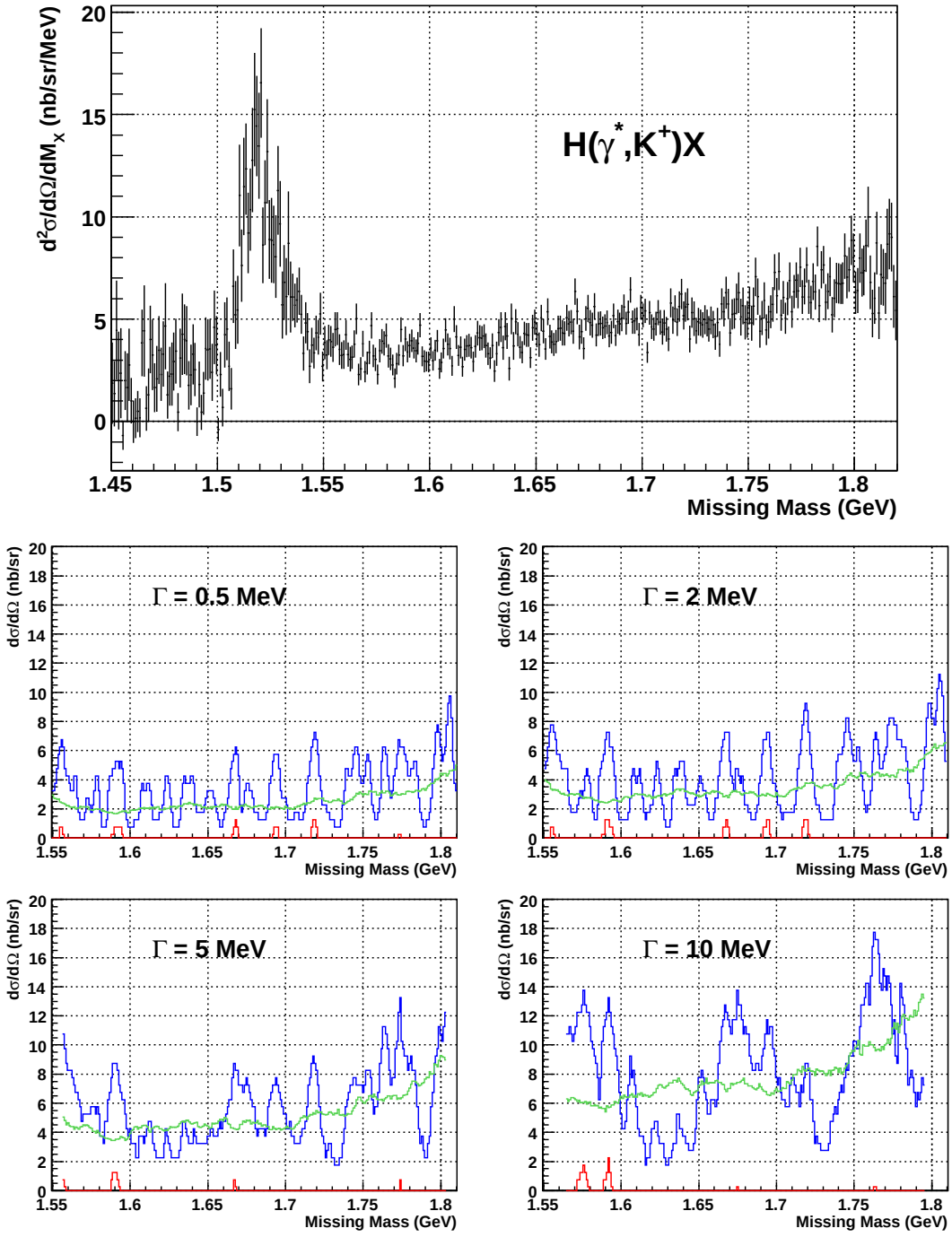

Figure 4-11: The upper and lower limit [top(blue) and bottom (red) solid lines] at 90% confidence level for the production of Σ_5^0 in the reaction $\gamma * p \rightarrow K^+\Sigma_5^0$ with $Q^2 \approx 0.1$ (GeV/c)^2, $E_{\gamma^*}^{\rm CM} \approx 1.1$ GeV, $\theta_{\gamma^* K}^{\rm CM} \approx 8.5^\circ \pm 2.9^\circ$ and $\Delta\Omega_{\gamma^* K}^{\rm CM} \approx 38$ msr. In most cases, the lower limit (bottom-red curve) is zero. The smoother green curve shows the statistical sensitivity.

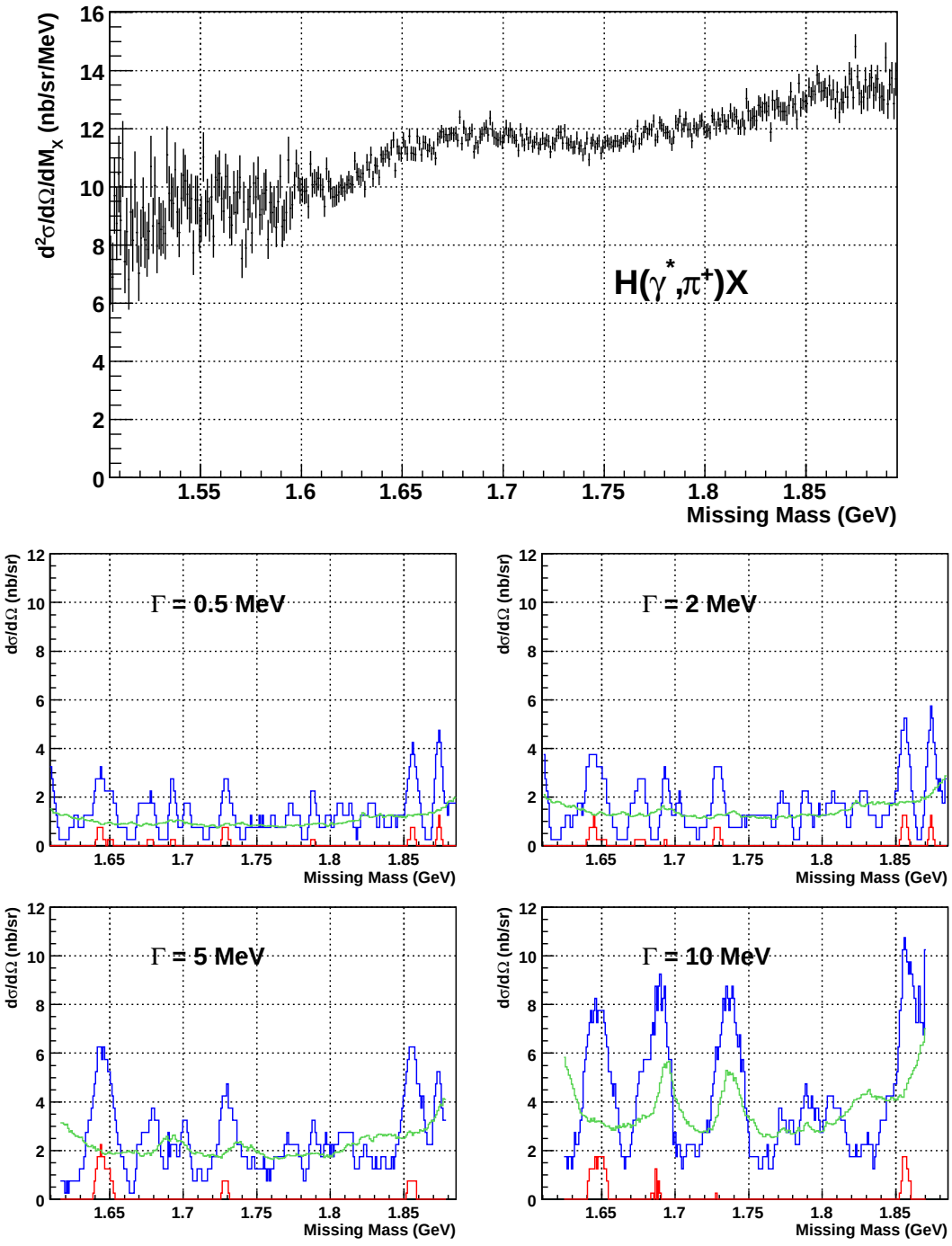

Figure 4-12: The 90% confidence level for the production of N_5^0 in the reaction $\gamma * p \rightarrow \pi^+ N_5^0$ with $Q^2 \approx 0.1$ (GeV/c)^2, $E_{\gamma^*}^{\rm CM} \approx 1.1$ GeV, $\theta_{\gamma^*\pi}^{\rm CM} \approx 7.7^\circ \pm 2.7^\circ$ and $\Delta\Omega_{\gamma^*\pi}^{\rm CM} \approx 32$ msr. the curves have the same meaning as in Figure 4-11.

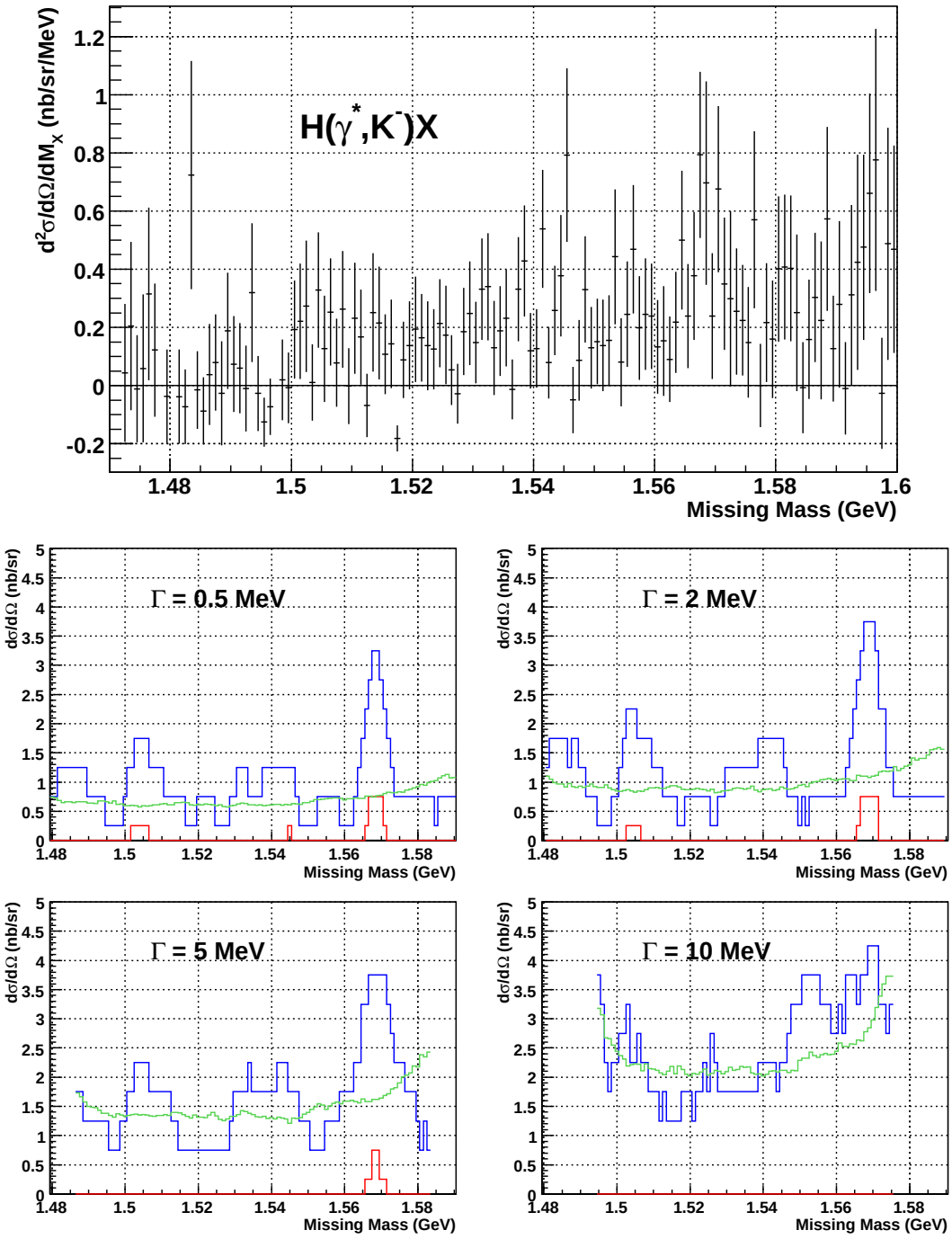

Figure 4-13: The 90% confidence level for the production of Θ^{++} in the reaction $\gamma * p \to K^- \Theta^{++}$ with $Q^2 \approx 0.1$ (GeV/c)^2, $E^{\rm CM}_{\gamma^*} \approx 1.1$ GeV, $\theta^{\rm CM}_{\gamma^* K} \approx 8.5^\circ \pm 2.9^\circ$ and $\Delta\Omega^{\rm CM}_{\gamma^* K} \approx 38$ msr. the curves have the same meaning as in Figure 4-11.

Appendix A

Hall A HRS+Septum Optics Database Calibration

The pair of Hall A septum magnets were firstly used during small angel GDH [67] experiment in 2003. Due to an error of the installation, the left septum could not bend scattered particles with designed 6 degrees. So, first complete set of optics data was not taken until the Hall A hyper-nuclear [66] experiment started in December 2003. This chapter will describe the new C++ method used in the first HRS+Septum optics matrix optimization.

A.1 Intrduction to HRS+Spetum Optics

The optics of spectrometers is not traditional "optics" for mirros and lens. It's more like a matrix transforming variables from detector system to target system. In other words, optics is the software part of a spectrometer system which releases the full potential of the hardware.

A.1.1 Hall A coordinate conventions

In this section, a short overview of Hall A coordinate conventions is presented. For more details, they can be found in reference [106, 107]. All coordinate systems pre-

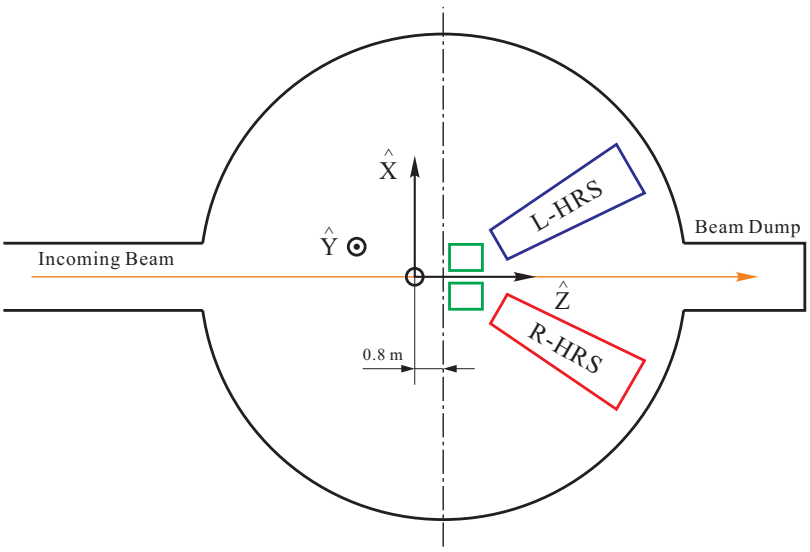

Figure A-1: Hall coordinate system (top view).

sented are Cartesian. Note that a reference to an angular coordinate in this section should be taken to refer to the tangent of the angle in question.

Hall Coordinate System (HCS)

The origin of the HCS is defined by the intersection of the electron beam and the vertical symmetry axis of the target system. As described in section 2.6, due to the installation of septum magnet the center is displace by 0.8 m upstream from the geometry center of Hall A. Direction $\hat{z}$ is along the beam line and points to the beam dump, $\hat{y}$ is vertically up and $\hat{x}$ is to the right facing the beam. See Figure A-1.

Target Coordinate System (TCS)

Each of the HRS is bundled with its own TCS. The central ray vertically passing through the center of sieve collimator[1] away from target defines the $z_{\rm tg}$ axis of the TCS for a given spectrometer. The $\hat{y}_{\rm tg}$ is pointing to the right and $\hat{x}_{\rm tg}$ is vertically down facing the central ray. See Figure A-2. In the ideal case where the spectrometer is pointing directly at the hall center and the sieve slit is perfectly centered on the

[1]The sieve slit is placed before the entrance of septum magnet. It is used to replace normal single hole collimator for optics calibration purpose. The plot of sieve hole can be found in Figure A.2.2.

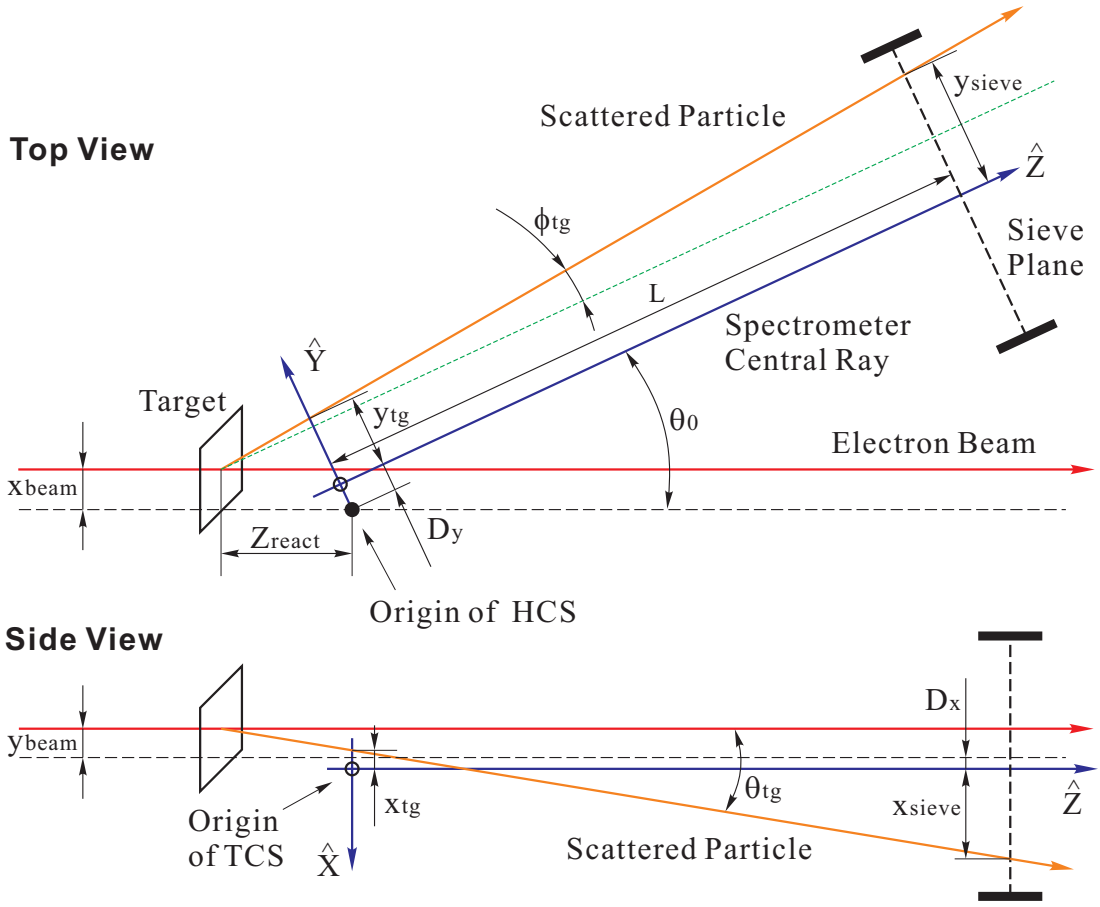

Figure A-2: Target coordinate system (top and side views).

spectrometer, the TCS has the same origin as HCS. However it typically deviates from HCS center by D_y and D_x in horizontal and vertical directions in TCS. And these shifts are given by survay. The distance of midpoint of the collimator from the TCS origin is defined to be a constant L for the spectrometer. The out-of-plane angle ($\theta_{\rm tg}$) ang the in-plane angle ($\phi_{\rm tg}$) are given by $dx_{\rm sieve}/L$ and $dy_{\rm sieve}/L$.

The TCS virables are used to calculate scattering angles and reaction points along the beam. Combined with beam variables (measured in the Hall coordinate system) the scattering angle and reaction point are given by

$$\theta_{\rm scat} = arccos(\frac{cos(\theta_0) - \phi_{\rm tg} sin(\theta_0)}{\sqrt{1+\theta_{\rm tg}^2+\phi_{\rm tg}^2}}) \tag{A.1}$$

$$z_{\rm react} = \frac{-(y_{\rm tg}+D_{\rm y}) + x_{\rm beam}(cos(\theta_0) - \phi_{\rm tg} sin(\theta_0))}{cos(\theta_0)\phi_{\rm tg} + sin(\theta_0)}, \tag{A.2}$$

where θ_0 denotes the spectrometer central angle. The in-plane and out-of-plane angles can be determined using sieve hole positions:

$$\phi_{\rm tg} = \frac{y_{\rm sieve} + D_y - x_{\rm beam}cos(\theta_0) + z_{\rm react}sin(\theta_0)}{L - z_{\rm react}cos(\theta_0) - x_{\rm beam}sin(\theta_0)} \quad (A.3)$$

$$\theta_{\rm tg} = \frac{x_{\rm sieve} + D_x + y_{\rm beam}}{L - z_{\rm react}cos(\theta_0) - x_{\rm beam}sin(\theta_0)}. \quad (A.4)$$

Furthermore,

$$y_{\rm tg} = y_{\rm sieve} - L\phi_{\rm tg} \quad (A.5)$$

$$x_{\rm tg} = x_{\rm sieve} - L\theta_{\rm tg}. \quad (A.6)$$

Detector Coordinate System (DCS)

The intersection of wire 184 of the VDC1 U1 plane and the perpendicular projection of wire 184 in the VDC1 V1 plane onto the VDC U1 plane defines the origin of the DCS. $\hat{z}$ is perpendicular to the VDC planes pointing verically up, $\hat{x}$ is along the long sysmmetry axis of lower VDC pointing away from the hall center (See Figure A-3).

Using the trajectory intersection points p_n (where $n = {\rm U1, V1, U2, V2}$) with the four VDC planes, the coordinates of the detector vertex can be calculated according to

$$tan(\eta_1) = \frac{p_{\rm U2} - p_{\rm U1}}{d_2} \quad (A.7)$$

$$tan(\eta_2) = \frac{p_{\rm V2} - p_{\rm V1}}{d_2} \quad (A.8)$$

$$\theta_{\rm det} = \frac{1}{\sqrt{2}}(tan(\eta_1) + tan(\eta_2)) \quad (A.9)$$

$$\phi_{\rm det} = \frac{1}{\sqrt{2}}(-tan(\eta_1) + tan(\eta_2)) \quad (A.10)$$

$$x_{\rm det} = \frac{1}{\sqrt{2}}(p_{\rm U1} + p_{\rm V1} - d_1 tan(\eta_2)) \quad (A.11)$$

$$y_{\rm det} = \frac{1}{\sqrt{2}}(-p_{\rm U1} + p_{\rm V1} - d_1 tan(\eta_2)). \quad (A.12)$$

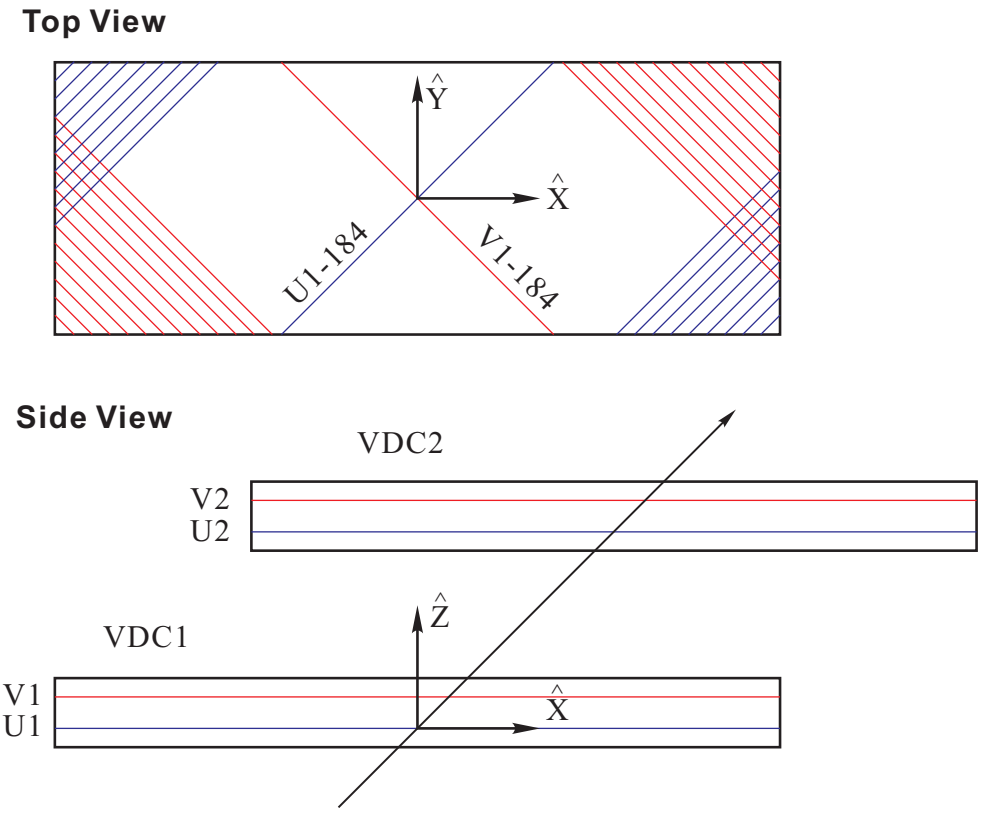

Figure A-3: Detector coordinate system (top and side views).

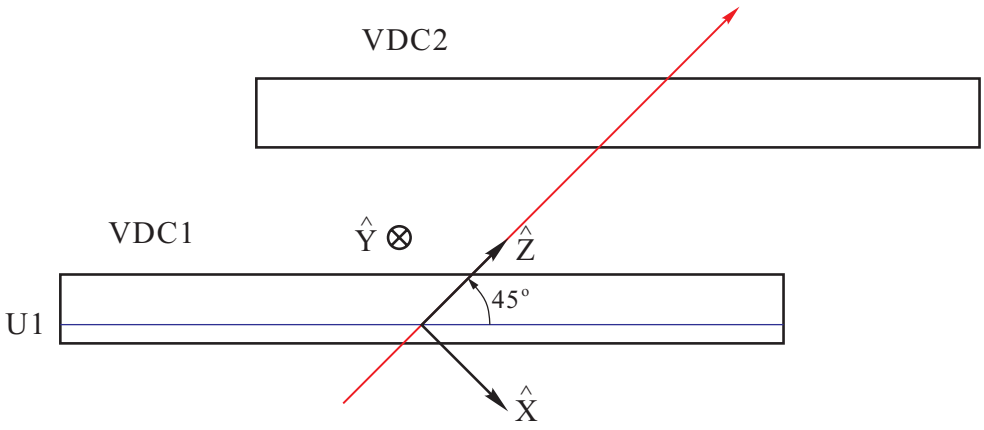

Figure A-4: Transport coordinate system.

Transport Coordinate System (TRCS)

The TRCS at the focal plane is generated by rotating the DCS clockwise around its y-sxis by 45 degrees. It's typically used as a mediate stage from DCS to the FCS which will be described in next section. Ideally, the $\hat{z}$ of the TRCS coincides with the central ray of the spectrometer. The transport coordinates can be experessed in terms of the detector coordinates by

$$\theta_{\rm tra} = \frac{\theta_{\rm det} + tan(\rho_0)}{1 - \theta_{\rm det} tan(\rho_0)} \tag{A.13}$$

$$\phi_{\rm tra} = \frac{\phi_{\rm det}}{cos(\rho_0) - \theta_{\rm det} sin(\rho_0)} \tag{A.14}$$

$$x_{\rm tra} = x_{\rm det} cos(\rho_0)(1 + \theta_{\rm tra} tan(\rho_0)) \tag{A.15}$$

$$y_{\rm tra} = y_{\rm det} + sin(\rho_0)\phi_{\rm tra} x_{\rm det}, \tag{A.16}$$

where $\rho_0 = -45^\circ$ is the rotation angle, see Figure A-4.

Transport Coordinate System (TRCS)

The focal plane coordinate system (FCS) chosen for the HRS analysis is a rotated coordinate system. Because of the focusing of HRS magnet system, particles from different scattering angles with same momentum will be focused at the focal plane. Therefore, the relative momentum to the central momentum of the spectrometer

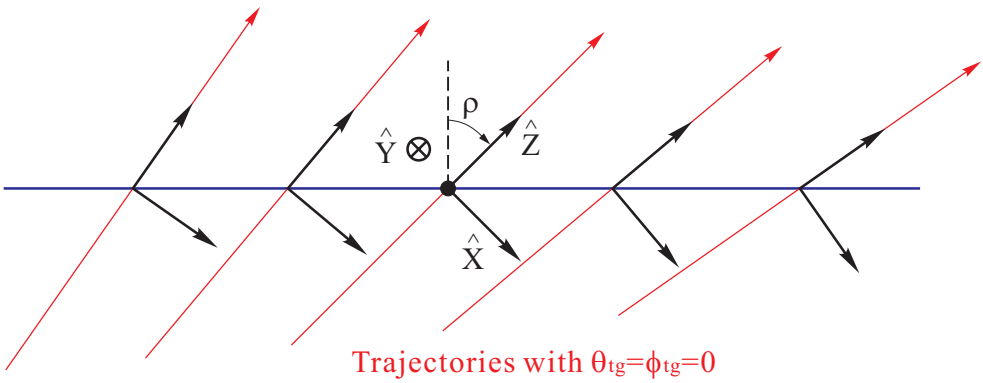

Figure A-5: Rotating focal plane system.

selected by magnet settings,

$$\delta = \frac{\Delta p}{p_0} = \frac{p - p_0}{p_0}, \tag{A.17}$$

is approximately only a function of $x_{\rm tra}$ and p_0 in the formular stands for the central momentum setting of HRS and Septum. And the FCS is obtained by rotating the DCS around its y-axis by an varying angle $\rho(x_{\rm tra})$ to have the new $\hat{z}$ axis paralell to the **local** central ray, which has scattering angle $\theta_{\rm tg} = \phi_{\rm tg} = 0$ for the corresponding δ at position $x_{\rm tra}$. In this rotated coordinate system, the dispersive angle $\theta_{\rm fp}$ is small for all points across the focal plane and approximately symmetric with $\theta_{\rm fp} = 0$. Such symmetry will greatly simply the further optics optimization.

With proper systematic offsets added, the coordinates of focal plane vertex can be written as follows:

$$\begin{aligned}
x_{\rm fp} &= x_{\rm tra} && \text{(A.18)}\\
tan(\rho) &= \sum t_{i000} x^i_{\rm fp} && \text{(A.19)}\\
y_{\rm fp} &= y_{\rm tra} - \sum y_{i000} x^i_{\rm fp} && \text{(A.20)}\\
\theta_{\rm fp} &= \frac{x_{\rm det} + tan(\rho)}{1 - \theta_{\rm det} tan(\rho)} && \text{(A.21)}\\
\phi_{\rm fp} &= \frac{\phi_{\rm det} - \sum p_{i000} x^i_{\rm fp}}{cos(\rho_0) - \theta_{\rm det} sin(\rho_0)}. && \text{(A.22)}
\end{aligned}$$

The transfer is not unitary and we have $x_{\rm fp}$ equal to $x_{\rm tra}$ for simplicity.

A.1.2 Matrix Approach

For each event, two angular coordinates ($\theta_{\rm det}$ and $\phi_{\rm det}$) and two spatial coordinates ($x_{\rm det}$ and $y_{\rm det}$) are measured at the focal plane detectors. The position of the particle and the tangent of the angle made by its trajectory along the dispesive direction are given by $x_{\rm det}$ and $\theta_{\rm det}$, while $y_{\rm det}$ and $\phi_{\rm det}$ give the position ang tangent of the angle perpendicular to the dispersive direction. These variables are corrected for any detector offsets from the ideal central ray of the spectrometer to obtain the focal plane coordinates $x_{\rm fp}$, $\theta_{\rm fp}$, $y_{\rm fp}$ and $\phi_{\rm fp}$. The focal plane observables are used to calculate θ, ϕ, y and δ at in the target system by matrix inversion.

The first order of such optics matrix can be expressed as,

$$\begin{pmatrix} \delta \\ \theta \\ y \\ \phi \end{pmatrix}_{\rm tg} = \begin{pmatrix} \langle\delta|x\rangle & \langle\delta|\theta\rangle & 0 & 0 \\ \langle\theta|x\rangle & \langle\delta|\theta\rangle & 0 & 0 \\ 0 & 0 & \langle y|y\rangle & \langle y|\phi\rangle \\ 0 & 0 & \langle\phi|y\rangle & \langle\phi|\phi\rangle \end{pmatrix} \cdot \begin{pmatrix} x \\ \theta \\ y \\ \phi \end{pmatrix}_{\rm fp} . \tag{A.23}$$

The null tensor elements result from the mid-plane symmetry of the spectrometer.

In parctice, the expansion of the focal plane coordinates is performed up to the fifth order. A set of tensors D_{jkl},T_{jkl},Y_{jkl} and P_{jkl} links the focal plane coordinates to target coordinates according to [108]

$$\delta = \sum_{j,k,l} D_{jkl}\theta_{\rm fp}^{j} y_{\rm fp}^{k} \phi_{\rm fp}^{l} \tag{A.24}$$

$$\theta_{\rm tg} = \sum_{j,k,l} T_{jkl}\theta_{\rm fp}^{j} y_{\rm fp}^{k} \phi_{\rm fp}^{l} \tag{A.25}$$

$$y_{\rm tg} = \sum_{j,k,l} Y_{jkl}\theta_{\rm fp}^{j} y_{\rm fp}^{k} \phi_{\rm fp}^{l} \tag{A.26}$$

$$\phi_{\rm tg} = \sum_{j,k,l} P_{jkl}\theta_{\rm fp}^{j} y_{\rm fp}^{k} \phi_{\rm fp}^{l}, \tag{A.27}$$

where the tensors D_{jkl},T_{jkl},Y_{jkl} and P_{jkl} are polynomials in $x_{\rm fp}$. For example,

$$D_{jkl} = \sum_{i=0}^{m} C_{ijkl}^{D} x_{\rm fp}^{i}. \tag{A.28}$$

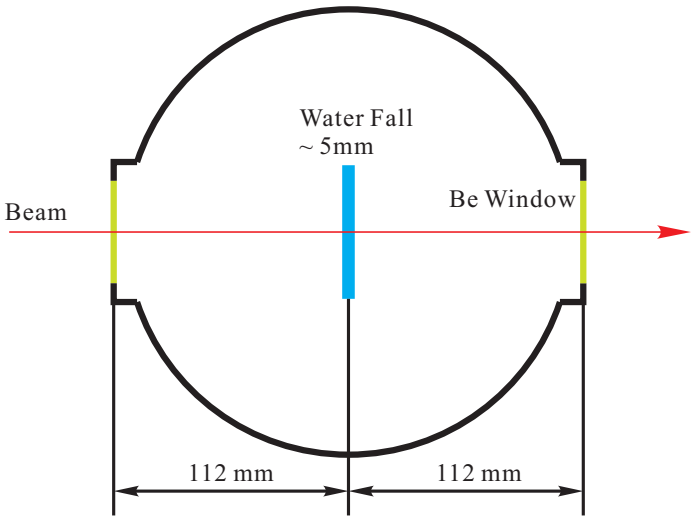

Figure A-6: Top section view of waterfall target.

A.2 Experimental and Optimization Procedure

A.2.1 Experiment

A full optimization of optics database requires sets of data with wide coverage on corresponding acceptance: δ in momentum, $\phi_{\rm tg}$ and $\theta_{\rm tg}$ in solid angle and $y_{\rm tg}$ for extended target. Other than reconstructed from detector variables the target variables' values in such experiments should also be obtained in other precise ways such as well known physics process: elestic scattering, nuclear excitation spectra or survey: target position, collimator sieve pattern. The ways are selected depending on which elements we want to optimize. Such kind of data were collected by performing the following series of calibration measurements.

- The first set of experiment were focused on angular and momentum calibration.

  1. A fixed energy 2037.2 MeV electron beam was incident on target. Two types of targets were used. One was typical 1 mm thick carbon and another one was a waterfall target build by INFN [109]. It contains a single waterfall with thickness around 5 mm and two 150 μm Be windows spaced by 224 mm as shown in Figure A-6.

2. Both HRS were positioned at 6 degrees. A pair of sieve slits with precisely drilled holes was used as collimators for the angular calibration, see Figure A.2.2.

3. The central momentum of both spectrometers was adjusted so that it will deviate from the momentum of elastically scattered electrons at 6 degrees by a few percent. This deviation was varied from +4.5% to -4.5% in steps of 1.3%. At each step measurements were taken with both targets with and without sieve slits. We call such sweep a delta scan. The idea of delta scan is trying to minimize the changes applied to the beam energy. By only changing the magnetic settings of the spectrometers, we are still able to scan the whole momentum acceptance.

- The second set of experiment was used to optimize y elements.

1. Three sets of carbon targets were used in this measurement. Except the single foil carbon target, the other two targets had two carbon foils spaced by 10 and 24 cm.

2. A 3776.86 MeV electron beam was incident on target. Both spectromers were set to collect inelastic scattering events, left arm at 1.96 GeV/c and right arm at 1.57 GeV/c.

During the calibration procedure, the raster was always turned off and the position of the beam on the target was kept within 100 μm away from the ideal beam line. As a result, the intersection point of the beam with the thin target foil provided a point target (to with the spectrometer resolution).

The following position and distances were then surveyed:

- the target position,

- the spectrometer central angles, and

- the position of the sieve slit center with respect to the spectrometer central axis.

A.2.2 Optimization Procedure and results

The major optics optimization procedure is illustrated in Figure A-7. The core program "Optimize++" was adopted from N. Liyanga's code [107] for ESPACE [110] optics database. Some new features and scripts were integrated to comply the new Hall A C++ Analyzer [85].

The optimization begin with an initial optics database generated by magnetic field simulation using SNAKE [111]. The core of the optimization program is the TMinuit package of ROOT [86]. This package will vary the optics matrix parameters to minimize the variance σ^2 of reconstructed data from their actual values. And the variance is calculated in the following way:

$$\sigma^2(x) = \sum_{i=1}^{m}\sum_{j=1}^{n}(x_{i,j}^{\text{recon.}} - x_i^{\text{survey}})^2, \tag{A.29}$$

where x can be any target variables, θ_{tg}, ϕ_{tg}, x_{tg} or δ, m is the total number of grid points measured in corresponding acceptance and n is number of events sampled for each point.

Sieve Pattern Reconstruction

The angular part of optics matrix was optimized firstly because the y_{tg} reconstruction and the elestic scattering momentum calculation are depending on the angles. The results from surveys were used to calculate the θ_{tg} and ϕ_{tg} of each hole.

The left figure shows the design of sieve slit, and the large holes are used to identify the orientation of the image at the focal plane. The right two plots show the improvement of the angluar resonstruction from left HRS after optimization. As a result, we got θ_{tg} (out-of-plane angle) reconstruted with a resolution of 4 mrad FWHM and ϕ_{tg} (in-plane angle) with 1.5 mrad.

Momentum delta scan

The momentum calibration requires precise measurement of spectrometer central momentum. With the constants determined in reference [112] the central momentum of

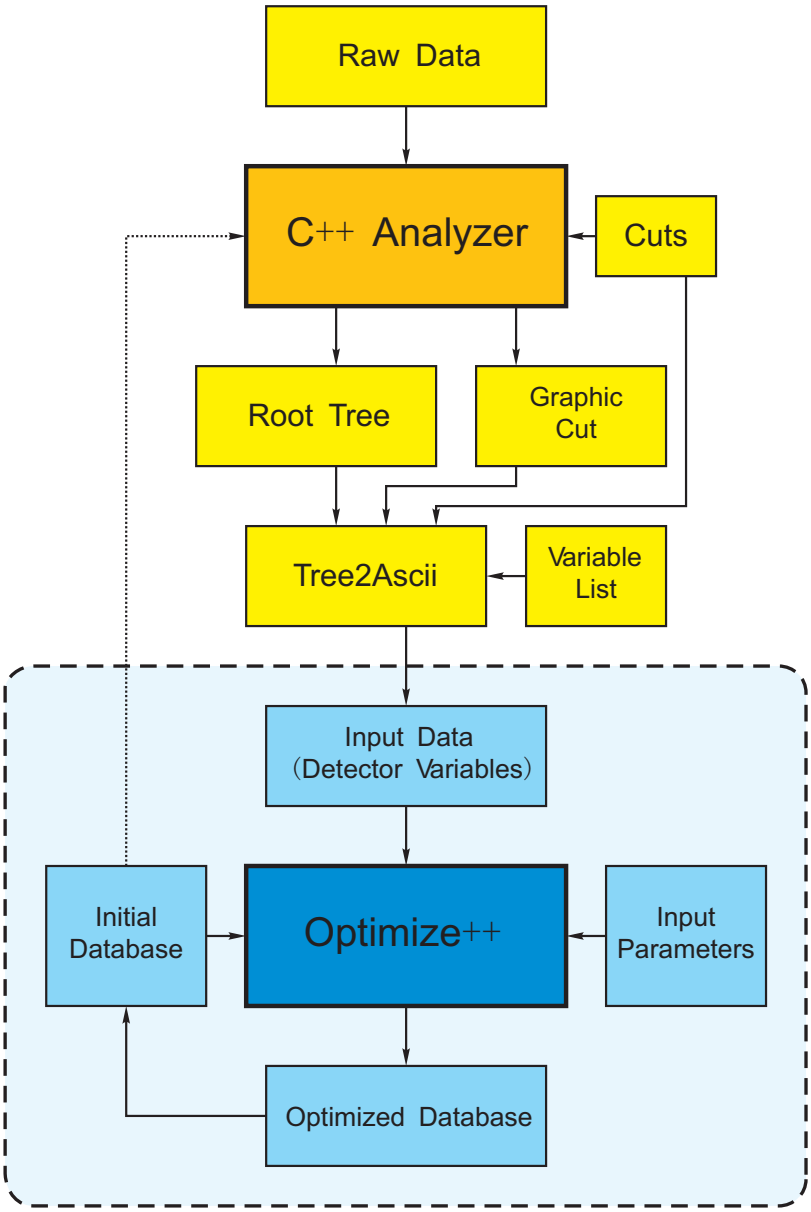

Figure A-7: Basic procedure for HRS+Septum optics optimization.

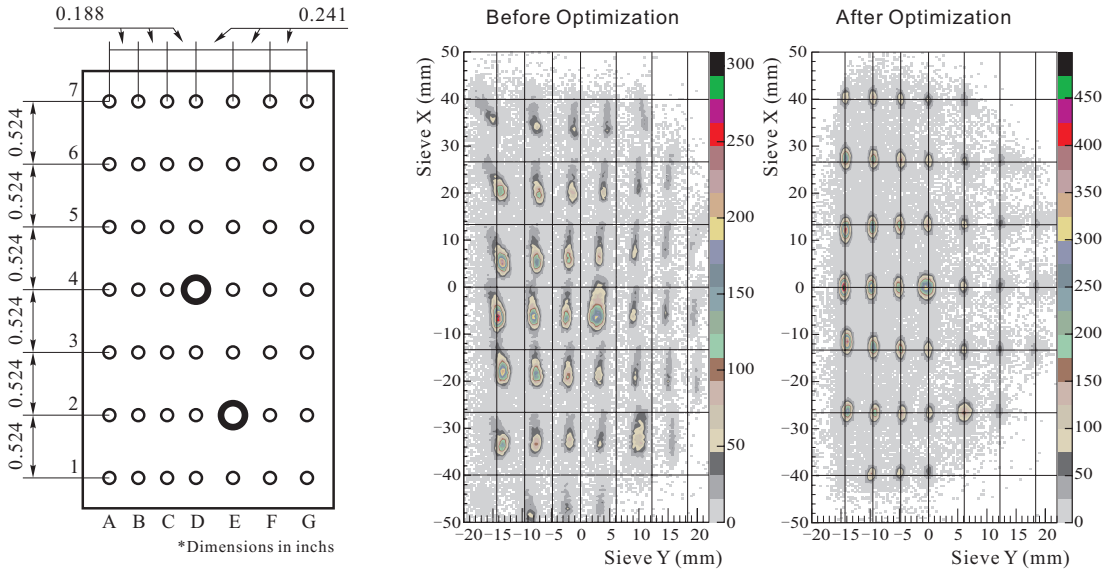

Figure A-8: Sieve Pattern Recostruction.

each settings were calculated using magnet field readouts from dipoles.

One issue in the elastic peak reconstruction is the angular dependence. The elastically scattered electron has energy (omit the electron's mass):

$$p(M,\theta) = E' = \frac{E}{1 + E/M(1 - cos(\theta))}, \tag{A.30}$$

where E is incoming electron energy, M is target mass and θ is scattering angle. So the our solid angle acceptance, the elastic peak will be broadened by this dependence and the effect becomes larger for lighter target elements. To remove such effect, a new variable called dp_{kin} is defined by

$$dp_{\text{kin}} = dp - \frac{p(M,\theta_{\text{scat}}) - p(M,\theta_0)}{p_0}, \tag{A.31}$$

where the scattering angle θ_{scat} is calculated using formula (A.1) and θ_0 is the central angle of spectrometer.

Figure A-9 shows the effect of this dp_{kin} correction in the water fall target elastic scattering. The hydrogen elastic peak after the correction can finaly be clearly identified. Of course, this method is only valid for elastic scattering from known targets.

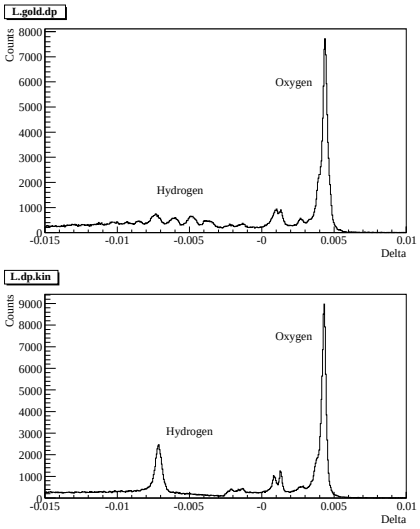

Figure A-9: $dp_{\rm kin}$ correction on elastic scattering from waterfall target.

Figure A-10 shows the results of a set of delta scan on Carbon target reconstructed using left HRS data.

The final relative momentum resolution is better than 2×10^{-4}.

Multi-foil targets

The $y_{\rm tg}$ optimization improved the transverse position resolution in target system to 2.5 mm FWHM, and it's corresponding to a 2.5 cm FWHM resolution of reaction point along beam in the 6 degrees configuration. The results are shown in Figure A-11.

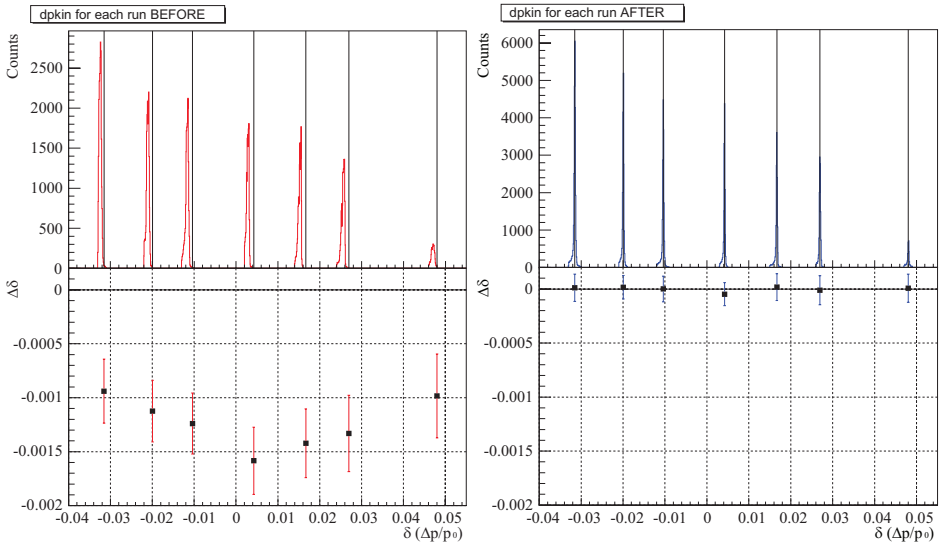

Figure A-10: Left HRS elestic peaks' reconstruction in a delta scan on Carbon target. The top plots show the absolute position of the peaks, the bottom plots show the deviation of reconstructed data from true values and the error bars show the resolution σ of those peaks.

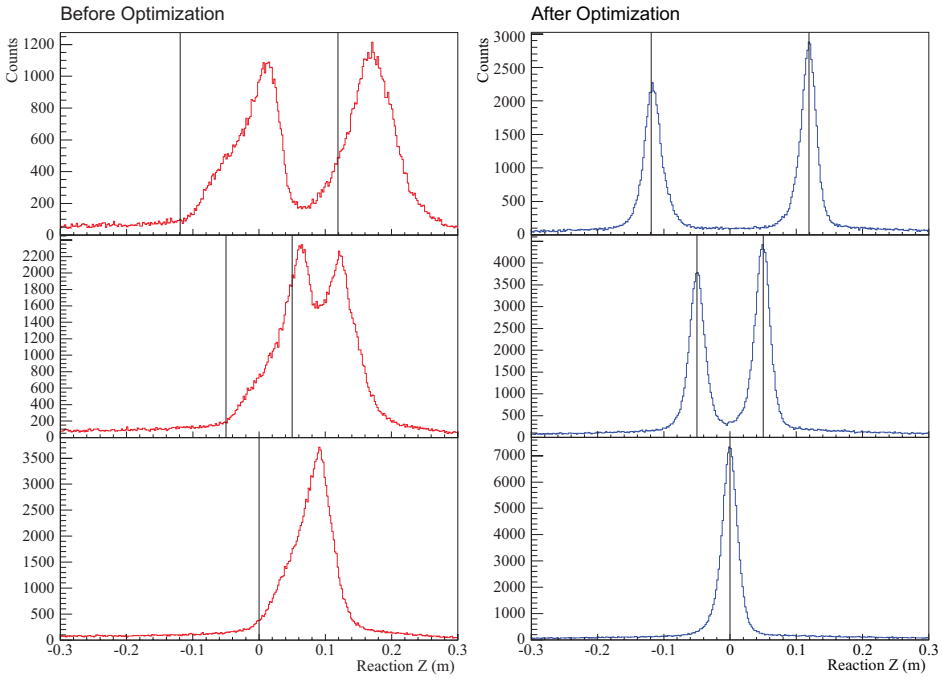

Figure A-11: Reaction positions reconstruction using multi-foil targets.

Bibliography

[1] V. Petrov D. Diakonov and M. Polyakov. *Z. Phys.*, A359:305, 1997.

[2] R. L. Jaffe and F. Wilczek. *Phys. Rev. Lett.*, 91:012002, 2003.

[3] (CLAS) S. Stepanyan *et al. Phys. Rev. Lett.*, 91:250001, 2003.

[4] (CLAS) S. Niccolai *et al. Phys. Rev. Lett.*, 97:032001, 2006.

[5] (NA49) C. Alt *et al. Phys. Rev. Lett.*, 92:042003, 2004.

[6] (STAR) H. Z. Huang. *Int. J. Mod. Phys.*, A21:825, 2006.

[7] (HERMES) A. Airapetian *et al. Nucl. Phys.*, A755:379, 2005.

[8] P. Reimer and B. Wojtsekhowski (spokespersons) *et al.* High Resolution Study of the 1540 Exotic State. *Jeffeson Lab Proposal E04-012*, 2004.

[9] R. L. Jaffe. *Phys. Rev.*, D15:267, 1977.

[10] H. Hogaasen and P. Sorba. *Nucl. Phys.*, B145:119, 1978.

[11] R. L. Jaffe. *Phys. Rev.*, D20:748, 1979.

[12] R. L. Cool *et al. Phys. Rev. Lett.*, 17.

[13] S. Mori *et al. Phys. Rev.*, 185:1687, 1969.

[14] (Particle Data Group) T. G. Trippe *et al. Rev. Mod. Phys.*, 48:S1, 1976.

[15] T. H. Skyrme. *Proc. Soc. Lond.*, A260:1975, 1961.

[16] T. H. Skyrme. *Nucl. Phys.*, 31:556, 1962.

[17] E. Witten. *Nucl. Phys.*, B223:433, 1983.

[18] E. Witten. *Nucl. Phys.*, B223:422, 1983.

[19] E. Guadagnini. *Nucl. Phys.*, B236:35, 1984.

[20] D. Diakonov and V. Petrov. *talks at the ITEP Winter School*, 1984.

[21] A. Manohar. *Nucl. Phys.*, B248:19, 1984.

[22] M. Chemtob. *Nucl. Phys.*, B256:600, 1985.

[23] M. Praszalowicz. *Proc. of the Workshop Skyrmions and Anomalies, Krakow, Poland, World Scientific*, page 112, 1987.

[24] (LEPS) T. Nakano *et al. Phys. Rev. Lett.*, 91:012002, 2003.

[25] K. H. Hicks. *Prog. Part. Nucl. Phys.*, 55:647, 2005.

[26] V. D. Burkert. *Int. J. Mod. Phys.*, A21:1764, 2006.

[27] R. A. Schumacher. nucl-ex/0512042. 2005.

[28] (DIANA) V. V. Barmin *et al. Phys. Atom, Nuclei*, 66:1715, 2003.

[29] (SAPHIR) J. Barth *et al. Phys. Lett.*, B572:127, 2003.

[30] K. Hicks. *Int. J. Mod. Phys.*, A20:219, 2006.

[31] (CLAS) M. Battaglieri *et al. Phys. Rev. Lett.*, 96:042001, 2006.

[32] W. Dunwoodie. *JLab Users Group Meeting*, 2006.

[33] A. E. Asratyan *et al. Phys. Atom. Nucl.*, 67:682, 2004.

[34] The ZEUS collaboration. *Phys. Lett.*, B591:7, 2004.

[35] (COSY-TOF) M. Abdel-Barv *et al. Phys. Lett.*, B595:127, 2004.

[36] A. Hosaka S. I. Nam and H. C. Kim. *Phys. Lett.*, B633:483, 2006.

[37] (BES) J. Z. Bai *et al. Phys. Rev.*, D70:012004, 2004.

[38] The Belle Collaboration. hep-ex/0409010.

[39] (ALEPH) S. Schael *et al. Phys. Lett.*, B599:1, 2004.

[40] (HERA-B) I. Abt. *et al. Phys. Rev. Lett.*, 93:212003, 2003.

[41] (SPHINX) Yu M. Antipov *et al. Eur. Phys. J.*, A21:455, 2004.

[42] (HyperCP) M. J. Longo *et al. Phys. Rev.*, D70:111101, 2004.

[43] (CDF) D. O. Litvintsev *et al.* hep-ex/0410024.

[44] M. V. Polyakov I. I. Strakovsky R. A. Arndt, Y. I. Azimov and R. L. Workman. *Phys. Rev.*, C69:035208, 2004.

[45] S. Nussinov. hep-ph/0307357.

[46] R. A. Arndt *et al. Phys. Rev.*, C68:042001, 2003.

[47] J. Haidenbauer and G. Krein. *Phys. Rev.*, C68:052201, 2003.

[48] W. R. Gibbs. *Phys. Rev.*, C70:045208, 2004.

[49] T. Bowen *et al. Phys. Rev.*, D2:2599, 1970.

[50] I. I. Strakovsky R. L. Workman Y. I. Azimov, R. A. Arndt and K. Goeke. *Eur. Phys. J.*, A26:79, 2005.

[51] S. Capsticl *et al. Phys. Lett.*, B570:185, 2003.

[52] H. Gao and B. Q. Ma. *Mod. Phys. Lett.*, A14:2313, 1999.

[53] (Particle Data Group) K. Hagiwara *et al. Phys. Rev.*, D66:1, 2002.

[54] (CLAS) V. Kubarovsky *et al. Phys. Rev. Lett.*, 97:102001, 2006.

[55] P. Brindza *et al.* Superconducting Septum Magnet Design for Jefferson Lab Hall A. *IEEE Transactions on applied superconductivity*, 11:1594, March 2001.

[56] P. Chevtsov *et al.* Synchrotron Light Interferometer at Jefferson Lab. *Proceedings of the 2003 Particle Accelerator Conference*, 2003.

[57] T. Mitsuhashi. Beam Profile Measurement by SR Interferometers. *Proceedings of the Joint U.S.-CERN-Japan-Russia School on Particle Accelerators, Montreus, Switzerland*, 1998.

[58] M. G. Minty and F. Zimmerman. Measurement and Control of Charged Particle Beams, Springer-Verlag, Berlin. page 163, 2003.

[59] J. Alcorn *et al.* Basic instrumentation for Hall A at Jefferson Lab. *Nucl. Instr. and Meth*, A522:294, 2004.

[60] K. Unser. *IEEE Trans. Nucl. Sci.*, NS28:2344, 1981.

[61] W. Barry *et al.* Beam Position Measurement in the CEBAF Recirculating Linacs by use of Pseudorandom Pulse Sequences, JLab-TN-90-246. 1990.

[62] W. Barry *et al.* Basic Noise Considerations for CEBAF Beam Position Monitors, JLab-TN-91-087. 1991.

[63] R. A. Lindgren. A CDR for a new Scattering Chamnber for Hall A. 2001.

[64] http://hallaweb.jlab.org/equipment/BigBite/.

[65] http://hallaweb.jlab.org/equipment/targets/cryotargets/Halla_tgt.html.

[66] F. Garibaldi *et al.* High Resolution 1p-Shell Hypernuclear Spectroscopy. *JLab Experiment E94-107*, 1994.

[67] A. Deur J. P. Chen and F. Garibaldi (spokespersons) *et al.* The GDH Sum Rule, the Spin Structure of ^{3}He and the Neutron using Nearly Real Photons. *Jefferson Lab Experiment E97-110*, 1997.

[68] R. Michaels (spokesperson) *et al.* Parity Experiment in HALL A, http://hallaweb.jlab.org/parity/.

[69] W. Bertozzi *et al. Nucl. Instr. and Meth.*, 191:957, 1977.

[70] K. G. Fissum *et al.* Vertical Drift Chambers for the Hall A High Resolution Spectrometers at Jefferson Lab. *Nucl. Instr. and Meth.*, A 474:108, 2001.

[71] B. Wojtsekhowski *et al.* High Performance Threshold Aerogel Counters. *Nucl. Instr. and Meth.*

[72] P. A. Ĉerenkov. *Phys. Rev.*, 52:378, 1937.

[73] E. Fermi. *Phys. Rev.*, 57:485, 1940.

[74] R. Perrino *et al. Nucl. Instr. and Meth.*, A457:571, 2001.

[75] L. Lagamda *et al. Nucl. Instr. and Meth.*, A471:325, 2001.

[76] R. Iommi *et al.* Test and Development of a Cherenkov diffusion detector prototype using Airglass aerogel at TJNAF, JLab-TN-00-010. 2000.

[77] ALICE Collaboration. Technical Design Report of the High Momentum Particle Identification Detector, CERN/LHCC98-19, Alice TDR 1. 1998.

[78] F. Garibaldi (spokesperson) *et al.* The Hall A RICH Detector. *Hall A Status Report 2001*, 2001.

[79] B. Reitz. TOSP for the Hall A RICH Detector. 2003.

[80] DuPont™ Tedlar®PVF Film. http://www.dupont.com/tedlar/.

[81] Hall A Operations Manual. 2000.

[82] A. Deur. TJNAF E94-010 Technical Note E94010-TN-03.

[83] Jefferson Lab Data Acquisition Group. The CODA Data Acquisition System, http://coda.jlab.org.

[84] Experimental Physics and Industrial Control System, http://www.aps.anl.gov/epics.

[85] http://hallaweb.jlab.org/root/index.html.

[86] http://root.cern.ch.

[87] C. L. Woody *et al. J. Phys. G: Nucl. Phys.*, 33:275, 2006.

[88] L. Zhu. Particle Identification with Aerogel Cherenkov Detector A1/A2. *Write-up for Hall A Data Analysis Workshop 2001*, Dec. 2001.

[89] P. E. Ulmer. *Ph.D. thesis, MIT*, 1998.

[90] D. V. Jordan. *Ph.D. thesis, MIT*, 1994.

[91] L. Weinstein. *Ph.D. thesis, MIT*, 1988.

[92] G. Cowan *et al. Phys. Lett.*, B592:275, 2003.

[93] P. Markowitz (spokesperson) *et al.* Electroproduction of Kaons up to $Q^2 = 3(GeV/c)^2$. *Jefferson Lab Proposal E98-108*, 1998.

[94] W. M. Yao *et al. J. Phys. G: Nucl. Phys.*, 33:31, 2006.

[95] J. J. Sakurai. Modern Quantum Mechanics. page 421.

[96] J. D. Jackson *et al. J. Phys. G: Nucl. Phys.*, 33:321, 2006.

[97] D. C. Fries *et al. Nucl. Phys.*, B143:408, 1978.

[98] D. P. Barber *et al. Z. Phys.*, C12:1, 1982.

[99] G. J. Feldman and R. D. Cousins. Unified Approach to the Classical Statistical Analysis of Small Signals. *Phys. Rev.*, D7:57, 1998.

[100] J. Neyman. *Trans. R. Soc. London*, A236:333, 1937.

[101] F. James *et al.*

[102] S. Baker and R. D. Cousins. *Nucl. Instr. and Meth.*, A221:437, 1984.

[103] W. A. Rolke *et al. Nucl. Instr. and Meth.*, A551:493, 2005.

[104] R. D. Cousins and Highland. *Nucl. Instr. and Meth.*, A320:331, 1992.

[105] G. J. Feldman. http://conferences.fnal.gov/cl2k/copies/feldman2.pdf.

[106] ESPACE Users Guide. 1997.

[107] N. Liyanaga. Optics calibration of the Hall A High Resolution Spectrometers using the New C++ Optimizer, JLab-TN-02-012. 2002.

[108] M. Berz *et al.* Spectrometer Constant Determination for the Hall A HRS Pair. *Nucl. Instr. and Meth.*, A258:402, 1987.

[109] Istituto Nazionale di Fisica Nucleare, Rome, Italy, http://www.infn.it/indexen.php.

[110] Event Scanning Program fot Hall A Collaboration Experiments, http://hallaweb.jlab.org/espace/index.html.

[111] http://hallaweb.jlab.org/news/minutes/tranferfuncs.html.

[112] N. Liyanaga. Spectrometer constant determination for the Hall A HRS Pair, JLab-TN-01-049. 2001.